TEMPLATE-ASSISTED SYNTHESIS AND STUDY OF ONE-DIMENSIONAL NANOSTRUCTURES ARRAY

LOH PUI YEE

B. Sc. (Hons.), NUS

A THESIS SUBMITTED

FOR THE DEGREE OF DOCTOR OF PHILOSOPHY

DEPARTMENT OF CHEMISTRY

NATIONAL UNIVERSITY OF SINGAPORE

2013

Acknowledgements

I would like to express my deepest gratitude to the people who had helped me through this path less travelled and made this thesis possible.

Firstly, for my PhD supervisor, Associate Professor Chin Wee Shong, who always find time for me despite her busy schedule. I would like to thank her for her professional guidance, enthusiastic encouragement and useful critiques. No matter it was for work or personal matters, she has been of good counsel and support.

Another big thanks to my co-supervisor, Associate Professor Sow Chorng Haur, for all the encouragement and productive discussions. His speedy proof-reading and constructive comments for paper writing are also very much appreciated.

Special thanks to Mr. Ho Yeow Lin Peter and Ms. Ng Yuting, final year undergraduate students under my supervision, for their respective preliminary work on MWCNT/PPV core-shell nanowires and Co/Al-LDH nanostructures which allowed me to further optimize the synthesis parameters and study their properties. Thanks to Mr. Lee Kian Keat as well for sharing his knowledge on electrochemical capacitors and sensors.

Many thanks to Ms. Lim Xiaodai Sharon for her kind support in the synthesis of aligned MWCNT arrays and the usage of focused laser beam systems in A/P Sow Chorng Haur's laboratory. Also, thanks to Mr. Ho Kok Wen and Mr. Lee Ka Yau for their assistance regarding the SEM and EDX instruments; Dr. Zhang Jixuan and Mr. Henche Kuan in the Department of Materials Science and Engineering for their support in TEM and XPS usage; Mr. Teo Hoon Hwee and Ms. See Sin Yin for their guidance in DR-FTIR measurement; and Mdm Tan Teng Jar for her support in the XRD measurement.

I am also very grateful to my seniors, Dr. Xu Hairuo and Dr. Yin Fenfang for their professional guidance and personal encouragement. Thanks also go to all my group members, Dr. Teo Tingting Sharon, Ms. Tan Zhi Yi, Mr. Lee Kian Keat, Mr. Huang Baoshi Barry, Ms. Yong Wei Ying Doreen, Ms. Chi Hong and Mr. Chen Jiaxin, for their support and making my days in the laboratory always enjoyable.

I am also thankful for the research scholarship provided by National University of Singapore (NUS).

Finally, my heartfelt gratitude goes to my family and my loving husband for their unconditional love and encouragement.

Table of Contents

Summary

The ability to control the length and shell thickness in synthesis of multi-layered one-dimensional (1D) nanostructures is an important aspect in the exploration of their properties, leading to the realization of their potential applications. Template-assisted synthesis using anodic aluminium oxide (AAO) membrane as sacrificial template and aligned multi-walled carbon nanotubes (MWCNT) as deposition surface are two versatile methods to grow 1D nanostructures. Thus, this thesis further demonstrates a few approaches of using the templates together with electrochemical and some chemical methods to grow various 1D hetero-nanostructures. Some potential applications of the resultant nanostructures are also illustrated.

To begin, Chapter 1 gives an overall background and scopes of this thesis. Chapter 2 then describes all necessary experimental procedures for syntheses, characterizations and properties measurements of nanostructures obtained.

In Chapter 3, we established optimal parameters to electropolymerize poly(*p*-phenylene vinylene) (PPV) into AAO nanochannels to give luminescent organic 1D nanostructures. Nanowires (NWs) and nanotubes (NTs) can be prepared by manipulating the conditions of plating solution and deposition potential, while their length is controllable by the deposition time. Micro-patterning via focused laser beam was also demonstrated. An interesting “red-shifting” of the photoluminescence maxima was observed upon laser modification in air but not in inert environment.

To further demonstrate the versatility of AAO, Chapter 4 presents our Pore-Widening method in creating coaxial multi-layered 1D hetero-nanostructures. Nanochannels of AAO have a certain thickness which can be manipulated with controlled etching to create annular gap around the cores for subsequent deposition of shells. With judicious selection of materials and sequences of steps, a few strategies are illustrated, leading to fabrication of various hetero-nanostructures such as polymer/metal, metal/metal, polymer/metal/metal and metal oxide/metal core-shell nanostructures.

AAO can be more than just a sacrificial template for deposition of 1D nanostructures. In Chapter 5, AAO was employed to fabricate cobalt-aluminium layered double hydroxides (Co/Al-LDH) hierarchical nanostructures. Here, AAO not only acts as template, but also provides Al^{3+} ions in the alkaline solution that isomorphously substitute some of the Co^{2+} during the hydroxide formation, forming Co/Al-LDH NFs on Co NWs. These arrays can be directly used as electrode for electrochemical capacitor and glucose sensing applications. Effects of alkaline treatment time on the morphology, Al content and properties of LDH NFs will also be discussed.

In the last result chapter, Chapter 6 describes the use of aligned MWCNT as support for growth of 1D nanostructures. Here, the electropolymerization conditions established in Chapter 3 is utilized to coaxially grow PPV onto the MWCNT, forming arrays of MWCNT/PPV core-shell nanostructures. Comparing to constant potentiometry, pulsed potentiometry was found to show better control of the shell thickness. The

resulting nanostructures were then tested for photocurrent response towards 405 nm laser.

Lastly, Chapter 7 gives an overall conclusion of the thesis work. Some future outlook and further exploration are also proposed here.

List of Publications

Nanowires with Controllable Core-Shell Structures: A "Pore Widening" Method. P. Y. Loh, C. M. Liu, C. H. Sow, W. S. Chin. *RSC Adv.* **4** (2014) 8735-8740.

CoOOH Nanosheet Electrodes: Simple Fabrication for Sensitive Electrochemical Sensing of Hydrogen Peroxide and Hydrazine. K. K. Lee, P. Y. Loh, C. H. Sow, W. S. Chin. *Biosens. Bioelectron.* **39** (2013) 255-260.

CoOOH Nanosheets on Cobalt Substrate as a Non-enzymatic Glucose Sensor. K. K. Lee, P. Y. Loh, C. H. Sow, W. S. Chin. *Electrochem. Commun.* **20** (2012) 128-132.

Facile Fabrication of One-dimensional Multi-component Nanostructures using Porous Anodized Alumina Membrane. P. Y. Loh, C. M. Liu, W. C. Pua, F. Y. Kam, W. S. Chin. *Cosmos* **6** (2010) 221-234.

Fabrication and Micropatterning of Luminescent Poly(*p*-phenylene vinylene) Nanotube Arrays. P. Y. Loh, C. M. Liu, C. H. Sow, W. S. Chin. – manuscript in progress.

Co/Al Layered Double Hydroxides Hierarchical Nanostructures: A Binderless Electrode for Electrochemical Capacitor. P. Y. Loh, K. K. Lee, Y. Ng, C. H. Sow, W. S. Chin. – manuscript submitted for publication.

Co/Al Layered Double Hydroxides Hierarchical Nanostructures as a Sensitive Non-enzymatic Glucose sensor. P. Y. Loh, K. K. Lee, Y. Ng, C. H. Sow, W. S. Chin. – manuscript in progress.

List of Tables

List of Figures

List of Abbreviations

λ_{exc}	Excitation wavelength
0D	Zero-dimensional
1D	One-dimensional
2D	Two-dimensional
3D	Three-dimensional
AA	L-Ascorbic acid
AAO	Anodic aluminium oxide
ACN	Acetonitrile
ALD	Atomic layer deposition
ASF	Atomic sensitivity factor
C-D	Charge-discharge
CE	Counter electrode
CMC	Critical micelle concentration
CNT	Carbon nanotubes
Co/Al-LDH	Cobalt-aluminium layered double hydroxides
Co/Al-NWNF-*y*	Label for “Co/Al-LDH NFs on Co NWs” electrodes, with *y* being the hours of alkaline treatment time during sample preparation
CPs	Conducting polymers
CV	Cyclic voltammetry
CVD	Chemical vapour deposition

DR-FTIR	Diffuse Reflectance Fourier-Transform Infrared Spectroscopy
DSSC	Dye-sensitized solar cells
DWNT	Double-walled nanotubes
ECs	Electrochemical capacitors
EDLCs	Electric double-layer capacitors
EDX	Energy Dispersive X-ray Spectroscopy
ESs	Electrochemical sensors
Et_4NBF_4	Tetraethylammonium tetrafluoroborate
EtOH	Ethanol
FET	Field-effect transistor
FIB	Focused ion-beam
FM	Fluorescence Microscopy
Glc	Glucose
GOx	Glucose oxidase
HRTEM	High-Resolution Transmission Electron Microscope
HT	Hydrotalcite
IEP	Isoelectric point
ITO	Indium tin oxide
I-V	Current-voltage
J-V	Current density-voltage
KOH	Potassium Hydroxide
LDH	Layered double hydroxides

LOD	Limit of detection
LOL	Limit of linearity
M1	First metal component
M2	Second metal component
MWCNT	Multi-walled carbon nanotubes
MWCNT/PPV-*n*	Label for samples of MWCNT/PPV core-shell NWs, where *n* is the total duration of the overall pulse cycles in minutes
NaOH	Sodium hydroxide
NFs	Nanoflakes
NPs	Nanoparticles
NRs	Nanorods
NSs	Nanosheets
NTs	Nanotubes
NWs	Nanowires
O_2 RIE	Oxygen reactive ion etching
OPVs	Oligophenylene vinylenes
PA	Polyacetylene
PANI	Polyaniline
PC	Photocurrent
PCB	Printed circuit board
PECVD	Plasma-enhanced chemical vapour deposition
PL	Photoluminescence Spectroscopy

PPV	Poly(*p*-phenylene vinylene)
PPy	Polypyrrole
PTh	Polythiophene
RE	Reference electrode
RF	Radio frequency
rpm	Revolutions per minute
RSD	Relative standard deviation
sccm	Standard cubic centimeter per minute
SEM	Scanning Electron Microscope
SLS	Solution-liquid-solid
TBX	α,α,α’,α’-tetrabromo-*p*-xylene
TEM	Transmission Electron Microscope
TFTs	Thin-film transistors
UA	Uric acid
VLS	Vapour-liquid-solid
WE	Working electrode
XPS	X-ray Photoelectron Spectroscopy
XRD	X-ray Diffraction

Chapter 1

Introduction

Nanotechnology involves the manipulation of matters with at least one dimension sized between 1 to 100 nm. The design and exploitation of such nanomaterials have attracted numerous research interests, both for fundamental studies and industrial applications.[1-4] This is due to their new or enhanced size- and shape-dependent properties as compared to their bulk counterparts. The reduction in sizes can lead to quantum confinement of electrons which was shown to influence the electrical conductivity and magnetic susceptibility of these materials.[5-8] Besides, their higher surface area and catalytic properties also proved to be useful for applications in electrochemical sensors and capacitors.[1,4] With the invention and development of advanced measuring instrumentation, scientists have been able to "see" and "manipulate" structure on the nanometer region. Such technological advancement further encourages the research of nanomaterials for a broader and ever increasing range of applications.

As proposed by Pokropivny *et al.*,[9] nanostructures can be classified according to their dimensionality as a whole, that is zero-dimensional (0D), one-dimensional (1D), two-dimensional (2D) and three-dimensional (3D). 0D nanostructures have all three dimensions that are sized in nanometric size range. Examples are quantum dots, nanoparticles (NPs) and hollow nanospheres.[10-12] As for 1D nanostructures, one of the dimensions is outside of nanometer range with examples such as nanoribbons, nanobelts, nanorods (NRs), nanowires (NWs) and nanotubes (NTs).[13-17] 2D nanostructures are such as nanoprisms, nanoplates, nanosheets, nanowalls and nanodisks, with two dimensions outside of nanometer range.[18-21] 3D nanostructures are assemblies or combinations of various nanostructures such as dendritic nanoballs, nanocoils, nanoflowers and branched NWs.[22-25] Among these nanostructures, 1D NWs and NTs are the focus of this thesis work and will be discussed in more details in the following sections.

1.1 One-dimensional (1D) nanostructures

Since the discovery of carbon nanotubes (CNT) in 1991,[26] research interests towards 1D nanostructures have increased tremendously. With their unique properties and increased surface area arises from their high aspect ratio (length-to-width), 1D nanostructures have demonstrated immense potentials both as the active functional materials[2-4] or as interconnects for various nanoscale devices.[27-29] As mentioned above, there are many forms of 1D nanostructures, all of which are characterized by a high aspect ratio. The most common ones are NRs, NWs and NTs. The only difference between NWs and NRs is their aspect ratio which is often defined as more and less than 20 for NWs and NRs, respectively. Their properties are largely dependent on the type of material but may also be affected by the shape, morphology and structure (i.e. crystalline or amorphous).

1.1.1 Single-component NWs and NTs

Single-component 1D nanostructures are simply NWs and NTs that consist of one type of material. The applications of such nanostructures are mainly dependent on the properties of material and/or the increased surface area of the nanostructures. Depending on the material that forms the single-component NWs or NTs, they can be applied as active functional electrodes or as interconnects in nanoscale devices.

One example of application as an electrode is the usage of V_2O_5 NWs array as cathode for lithium (Li) ion battery.[30] With decreased diameter of the electrode material, the distance that Li^+ ion must diffuse within the electrode would be decreased which then improves the low-temperature performance of Li ion batteries. This opens up potential utilization of lithium ion batteries under sub-zero temperatures. In addition, magnetite Fe_3O_4 NWs[31] and hydrogen-treated cap-opened Si NTs[32] also exhibit excellent performance as anodes for Li-ion battery. Array of 1D metal oxides nanostructures are also popularly studied as photoelectrodes for dye-sensitized solar cells (DSSC), especially TiO_2 and ZnO NWs and NTs.[3] These 1D photoelectrodes were shown to improve charge transfer by providing direct pathways for electron transport in the device as compared to NPs films.

Other than the inorganic components, conducting polymer NWs such as polyaniline (PANI) also demonstrated various useful applications such as chemical sensors, supercapacitors[33] and biosensor.[34] Polypyrrole (PPy)

NWs array also exhibited excellent response to pH changes and good stability over time.[35]

Recently, an interesting work presented the fabrication of ultra-long Cu NWs array bumps as “Velcro” interconnects to connect circuits on two different substrates.[28] These arrays were deposited onto conductive electrode on both Si die and printed circuit board (PCB) substrates. By attaching these NWs arrays, they form a contact similar to the commercial “Velcro” type loop fastener.

1.1.2 Multi-component NWs and NTs

It is only natural to progress from single-component towards the fabrication and design of more complex, multi-component 1D nanostructures for wider range of applications. In addition to the benefits of 1D morphology, the coupling of different materials into a 1D nanostructure also presents multi-functionality or new properties arising from synergistic effects between the different material components, such as *p-n* junctions or Schottky diodes. Examples of such nanostructures include segmented NWs, core-shell NWs and multi-walled NTs, all of which contain hetero-junctions between various combinations of materials.

Various segmented NWs consisting of metal and conducting polymer (CP) were fabricated.[36] An example is Co-PPy-Co NWs which were fabricated electrochemically in single-wire form inside the anodic aluminium oxide (AAO) template.[37] Using this metal-CP-metal NW, a field-effect transistor (FET) was easily produced, simply by patterning a gate on one side of the wire. The advantages of this in-wire FET include reproducible metal-organic junctions, controllability of the diameter and easy integration of the devices. Rather than only a few segments, multi-segmented NWs were also fabricated such as Ni-Cu and Ni-Pt multi-segmented NWs arrays.[38, 39] These NWs were fabricated in AAO template using pulsed electrochemical method from a single plating solution consisting of both metal ions. Both arrays showed enhanced coercivity than that of the bulk and NWs of Ni, and this can be attributed to single magnetic domain of cylindrical Ni nanoparticles separated by Cu or Pt segments.

Core-shell NWs and NTs with coupled core and shell materials have shown great potential applications in solar cells, sensors and energy storage.[16, 40-43] Various combinations of materials were explored including semiconductors, metals, metal oxides and conductive polymers.[40, 42-48] Some of these hetero-nanostructured architecture reported functional advantages such as formation of *p-i-n* junction coaxially within one strand of core-shell NW[40] and as protection of the core material from external environment by coating a thermally and chemically stable shell over the core.[49] Others also demonstrated enhanced performance due to synergistic effect between the core and the shell components.[16, 42] By tweaking the synthesis procedures, a nanoscale coaxially gated in-wire thin-film transistors (TFTs) were realized by fabricating Au/CdS/Au segmented NWs wrapped around by SiO_2.[50] Besides, coaxial nanocables consisting of silver core and amorphous carbon shell were also shown to have potential as interconnects.[27] To properly connect the core, the insulating shell must first be etched away before depositing the platinum microlead using focused ion-beam (FIB) technique.

1.2 Strategies for the synthesis of 1D nanostructures

A common challenge in the study of 1D nanomaterials is the development of simple and cost-effective anisotropic synthesis methods. Various synthetic strategies have been reported to prepare both single- and multi-component 1D nanostructures.[51-54] These synthesis methods can be broadly divided into top-down and bottom-up approaches. Top-down approaches (physical and engineering techniques such as sputtering[55] and lithography[13, 56]) seek to create structures with smaller dimension from larger ones; whereas bottom-up approaches seek to arrange smaller components (e.g. atoms and molecules) into more complex assemblies (nanostructures). Only the latter approaches will be further discussed here as it is more relevant to this thesis work.

Chemical synthesis processes are considered to be bottom-up approach to prepare 1D nanostructures. Among these processes, the growth of 1D nanostructures often follows one or a combination of the strategies as illustrated in Figure 1.1. The first strategy as shown in Figure 1.1A exploits the intrinsic anisotropic crystallographic structures whereby these materials naturally grow into 1D nanostructures. Since not all materials have such crystallographic structures, this strategy is limited to only a few types of material such as molybdenum chalcogenides,[57, 58] chalcogens[59, 60] and metallophthalocyanines.[61-63] As for the second strategy in Figure 1.1B, the uni-directional growth is incited by reducing the symmetry of the nucleation seed, achievable from the introduction of liquid-solid interface. The precursor or starting material for the growth can be supplied via vapour (as in vapour-liquid-solid, VLS) or solution (as in solution-liquid-solid, SLS). Uni-directional growth can also be achieved by kinetically limiting the growth rates of certain facets of a seed with suitable capping reagent as illustrated by the third strategy in Figure 1.1C. Lastly, 1D nanostructures can be fabricated using template with 1D morphology as a mould for directed growth as shown in Figure 1.1D.

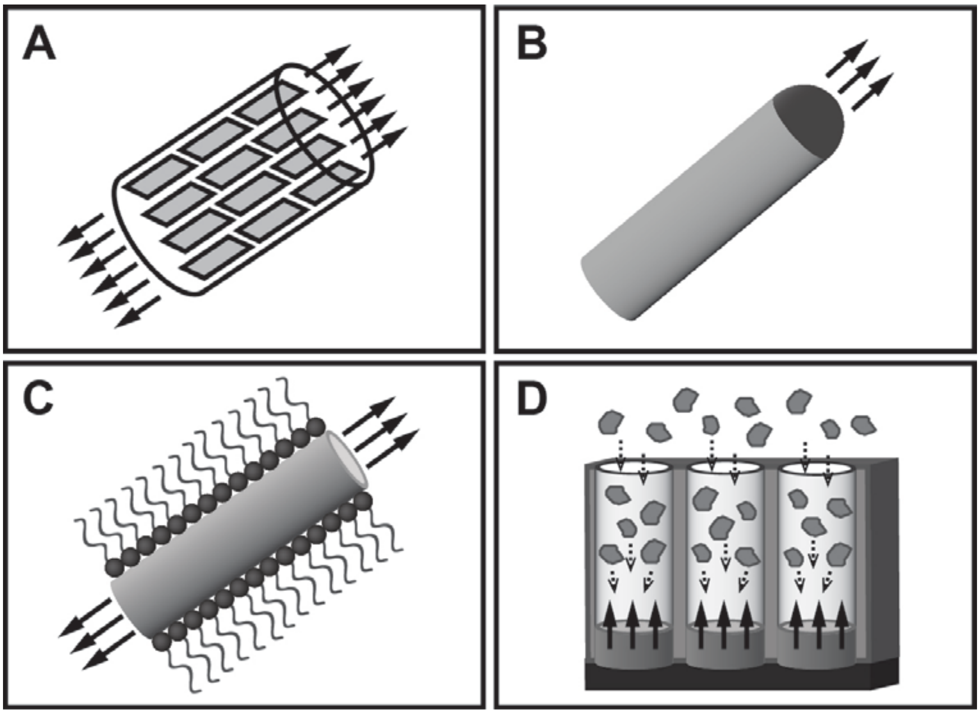

Figure 1.1: Strategies to fabricate 1D nanostructures: (A) dictation by the intrinsic anisotropic crystallographic structure, (B) directed growth by a liquid droplet as in the vapour-liquid-solid (VLS) and solution-liquid-solid (SLS) processes, (C) kinetic control by capping reagent, and (D) template-assisted growth. [Schematics redrawn and adapted from Ref. 51]

Since the first strategy is very limited to certain type of materials, it will not be further discussed in this Chapter. The other three strategies are more generic, and some popular synthesis methods that apply these strategies will be briefly discussed in the following sub-sections. In relation to the work in this thesis, template-assisted methods will be discussed in more details.

1.2.1 Vapour-liquid-solid (VLS) and Solution-liquid-solid (SLS) methods

Both VLS and SLS methods have similar mechanism where the growth of NWs is confined by the introduction of liquid-solid interface which reduce the symmetry of a seed as illustrated in Figure 1.1B. These methods often results in highly crystalline NWs and is common for the synthesis of various semiconductors NWs.

VLS was first developed by Wagner *et al*.[64] in the 1960s and recently re-examined by Lieber, Yang and many other research groups.[65-78] As the name implies, the starting materials (precursors) are in vapour phase which would then dissolved into the liquid droplets (catalysts) for growth of solid NWs. The important steps of VLS method are shown in Figure 1.2 and this mechanism were confirmed by Yang and co-workers.[65] A typical reaction starts with (i) metal alloying where gaseous precursors dissolved into the nanosized liquid droplets of catalyst, (ii) crystal nucleation when liquid droplets are super-saturated with the desired material and (iii) axial growth where the NRs grow into NWs. Since the 1D growth is mainly induced by the liquid droplets, one major requirement is that the metal catalyst must be able to form liquid alloy (ideally a eutectic mixture) with the target solid material. They must also be inert to other materials and have low vapour pressure at the growth temperature. To satisfy these requirements, catalysts used are typically noble metals (e.g. Au, Pt or Ag) or transition metals (e.g. Ni or Fe) with high melting point. In addition, the diameter of NWs grown is mainly determined by the size of the catalyst droplets. This was further demonstrated by Lieber and Yang where the specific sizes of Si and GaP NWs could be prepared by simply controlling the diameter of monodispersed gold colloids or clusters used as the catalyst.[65-67] The vapours of precursors can be generated by various methods such as laser ablation, thermal evaporation, arc discharge and chemical vapour deposition (CVD), but these did not affect the quality of NWs. Using this method, various semiconductor NWs and NRs were generated including Si, Ge, GaN, GaP, ZnS, CdS, ZnO and SiO_2.[68-78]

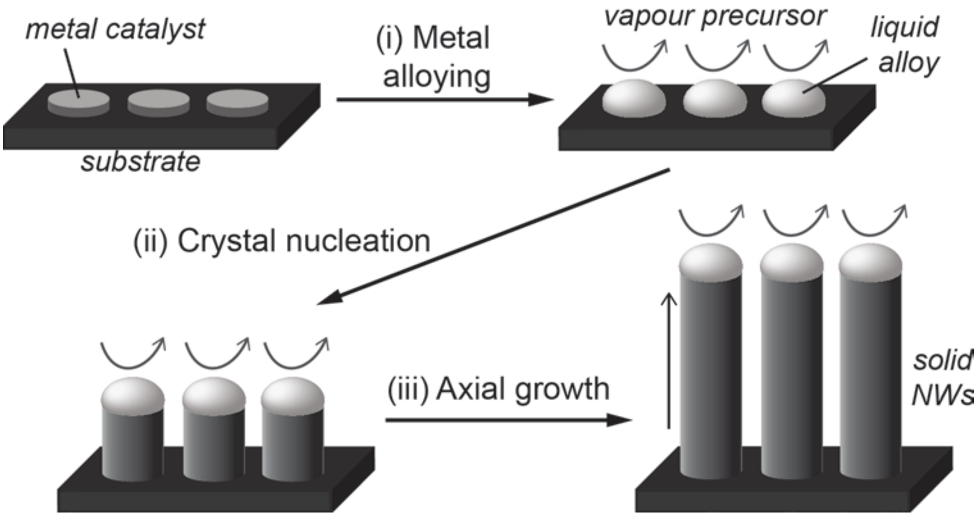

Figure 1.2: Schematic showing the mechanism for growth of NWs via VLS method. [Schematics redrawn and adapted from Ref. 53]

Based on an analogy to the VLS process, SLS method was first developed by Buhro *et al.* to synthesize crystalline NWs of III-V semiconductors at relatively low temperatures.[79] As shown in Figure 1.3, the mechanism of SLS is analogous to VLS process except that the precursors are transported to the metal catalyst through solution instead of vapour phase. Compared to VLS, the SLS method applies lower growth temperature (often below the boiling point of solvent used) and employs low-melting-point metals such as Bi, Sn and In as the catalyst to grow crystalline NWs in solution.[79] The diameter of the resulting NWs is also dependent on the size of metal catalyst, similar to VLS method. Thus, monodispersed NPs of low-melting-point metals with controlled diameters were shown useful to produce thin NWs with narrow diameter distribution.[80-83] Other than using metal NPs, it was reported that metal salts can also be used as the catalyst for NWs growth via SLS method such as using $BiCl_3$ to grow ZnSe NWs.[84] The desired material for NWs is commonly derived from the decomposition of two organometallic precursors. For example, GaAs NWs from the decomposition of $(t\text{-Bu})_3Ga$ and $As(SiMe_3)_3$ with In-NPs catalyst,[80] and CdSe NWs from cadmium stearate and $n\text{-}R_3PSe$ (R = butyl or octyl) with Bi-NPs catalyst[85] or CdO and trioctylphosphine selenide using Au/Bi-NPs catalyst.[86] There were also reports on employing clusters as single-source precursors which resulted in better control and smaller diameter of NWs.[87] Recently, SLS method has been adopted to prepared NWs films which are free-standing on substrates. This was shown to be feasible by using metal catalyst films[88-90] or pre-formed metal catalyst NPs[83] deposited on substrates as the catalyst for growth of NWs, or using an electrically controlled SLS process to synthesize the NWs directly on the electrode surface.[91, 92]

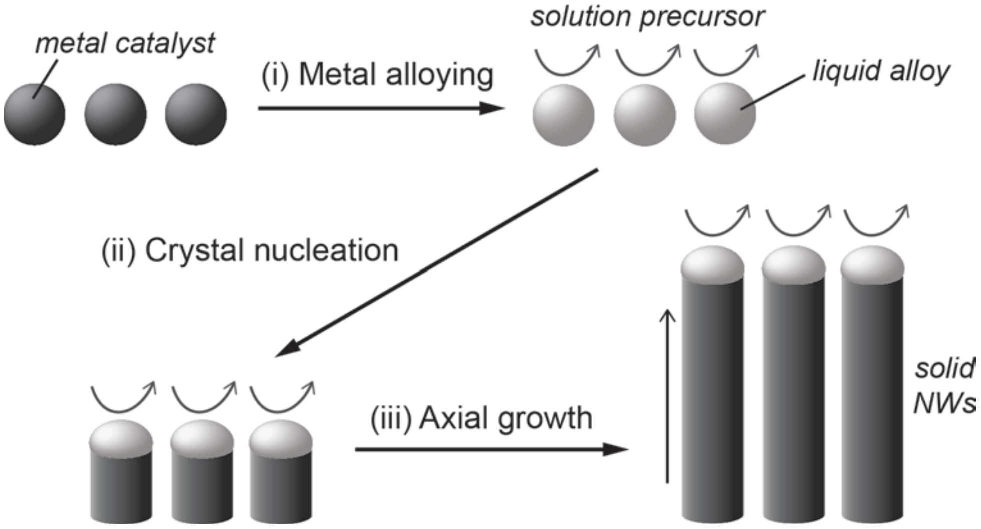

Figure 1.3: Schematic showing the mechanism for growth of NWs via SLS method. [Schematics redrawn and adapted from Ref. 53]

VLS and SLS methods can also be applied to fabricate multi-component 1D nanostructures. Various approaches were reported depending on the desired type of 1D hetero-nanostructures. Single-step VLS was reported for the synthesis of core-shell NWs where all precursors for the core and the shell were introduced at the same time. Here, the core and shell is grown consecutively which occurs due to differences in the reactivity of the core and shell materials. Examples are CdS/ZnS, ZnO/(Mg,Zn)O and GaN/BN core-shell NWs.[93-98] Otherwise, segmented or core-shell NWs can also be obtained by alternating the introduction of precursors for deposition of each segments or layers for instance Si/SiGe multi-segmented NWs,[99] Si/Ge[100] and *p-i-n* Si core-shell NWs[40] via VLS methods, and CdS/CdSe,[88] ZnSe/ZnTe[101] and CdSe/ZnSe[90] segmented NWs via SLS methods. Besides, combination of VLS or SLS processes with other methods can also be applied to fabricate hetero-nanostructures. This approach allows more freedom of the combination of desired materials such as CdSe/CdS,[102] ZnSe/CdSe[84] and CdTe/ZnSe[103] core-shell NWs.

1.2.2 Kinetic-controlled growth methods

According to Wulff facets theorem,[104] the shape of a single-crystalline crystal often follow the intrinsic symmetry of the crystal. For instance, most metallic crystals grow to be a cube rather than a rod. Besides, the growth kinetics of each crystal planes also determine the final shape of the crystal.[105] This implies possibility to control the final shape of a crystal by attaching appropriate capping reagent(s) to alter the growth rates of specific facet. One example of capping agent is 1-hexadecylamine which was demonstrated in the synthesis of ZnS NRs.[106] It was proposed that the amine group selectively adsorbed to the (110) facet of ZnS nanoscrystals and minimized its surface energy, thereby impeding the growth along this plane and promoted the growth along (111) plane to form NWs. Besides amine group, polymers such as poly(vinyl pyrrolidone) were also used as capping agent for growth of silver NWs.[107]

The capping agent can also play an additional role of attacking agent (catalyst) which simplifies the synthesis of nanostructures. As demonstrated by Zhang *et al.*,[108, 109] the amine group was proposed to play dual role as both the attacking agent and capping agent for decomposition of single-precursor lead thiobenzoate and zinc acetate to give PbS and ZnO nanostructures, respectively. For the synthesis of PbS NWs, small amount of thiol was added together with the amine as capping agent for 1D growth. As the activating agent, the amine may behave like a nucleophile and attacked the electron-deficient carbon of the carbonyl group of acetate, leading to an addition-elimination process which generate PbS and ZnO monomers. The remaining amine groups in the reaction pot would then act as the capping agent for crystals growth. By adjusting the ratio of amine (or thiol) to precursor, 1D growth into NWs was successfully obtained.

1.2.3 Template-assisted methods

Template-assisted synthesis as illustrated in Figure 1.1D is a straightforward route to 1D nanostructures where the template simply serves as a scaffold for materials to grow in or onto. Using this method, the morphology of the nanostructures is very much determined by the shape of the template and synthesis steps chosen for deposition of desired materials. Overall, this method is simple and cost-effective, which provides high-throughput and allows easy duplication of the template’s topology. Nevertheless, the resulting product is often polycrystalline and relatively low in quantity for each run.

The template can be sacrificial (where the template will be removed after the deposition of 1D nanostructures) or as deposition surface (where the template will become part of the desired 1D nanostructures). Typical templates used are such as anodic aluminium oxide (AAO), track-etched polycarbonate, self-assembled molecular structures and existing NWs or NTs. The first three examples are usually the sacrificial type while the last become part of the desired 1D nanostructures. The former approach of using the template as sacrificial scaffold commonly involves three steps: (1) infiltration of the template with precursor or starting material, (2) conversion of the precursor to material of interest, and (3) selective removal of template to obtain pure 1D nanostructures. Among the examples of sacrificial templates mentioned, AAO and track-etched polycarbonate are considered as hard template while the self-assembled molecular structures are soft template.

The use of cylindrical nanopores in AAO and track-etched polycarbonate as template in the synthesis of 1D nanostructures was pioneered by Martin and co-workers.[110-112] These templates are versatile and can be obtained commercially from a number of vendors. Since these templates are sacrificial, materials to be fabricated will have to be inert to the reagent used to remove the template. Nevertheless, various materials were demonstrated to be compatible with the templates with examples such as metals, semiconductors, ceramics and polymers.[30, 50, 110-125] Most of the reports on templated synthesis of 1D nanostructures were based on AAO due to its higher pore density, more ordered array of pores and better control over the morphology of the resulting product. As shown in Figure 1.4, various 1D nanostructures can be prepared using AAO as the template, simply by adjusting the way of filling up the nanopores and sequences of deposition steps.[36, 48, 113, 116] A variety of techniques were demonstrated to infiltrate the template to obtain various 1D nanostructures, ranging from electrochemical methods[48, 119, 120, 124] to chemical methods such as CVD,[121] sol-gel,[30, 44] layer-by-layer chemical deposition[122] and hydrothermal[125] or combinations of these methods.[50, 123]

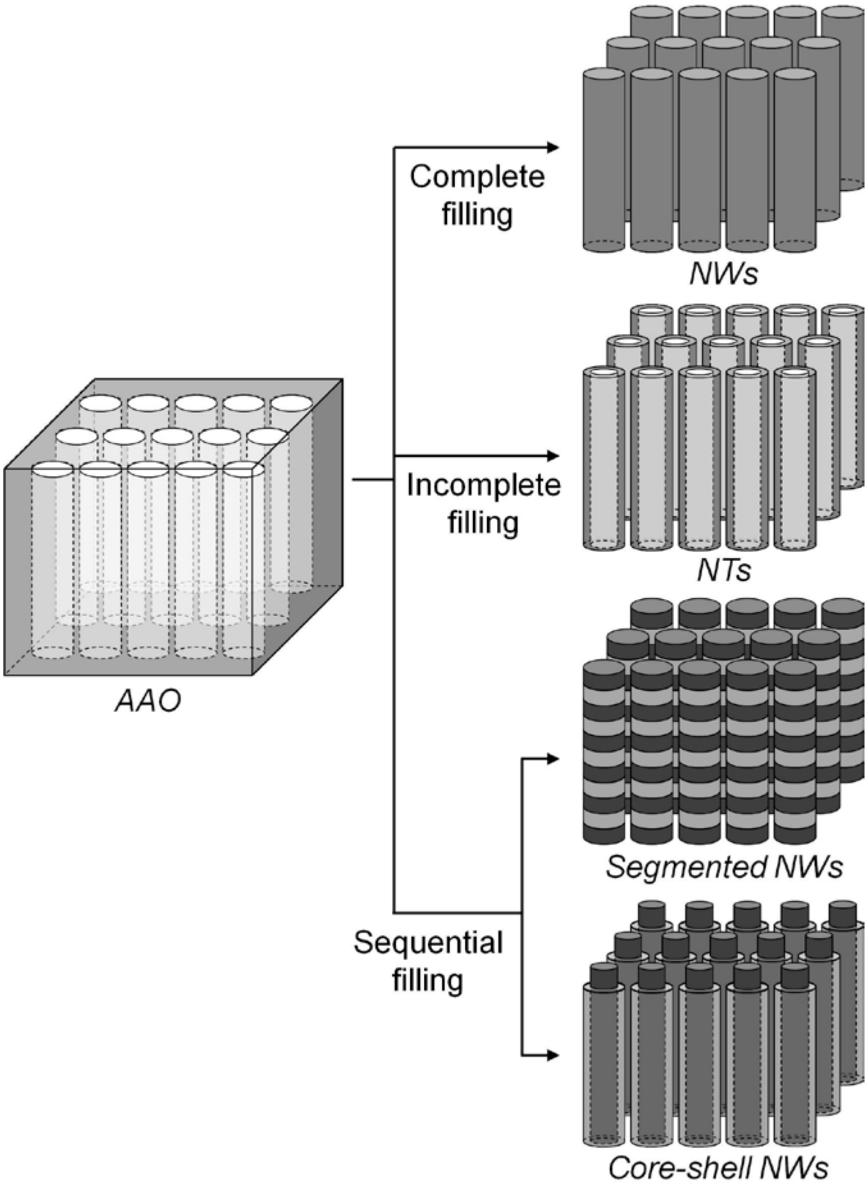

Figure 1.4: Schematic diagram showing the formation of NWs, NTs and multi-component nanostructures by complete, incomplete and sequential filling of the nanochannels of AAO, respectively.

Another type of sacrificial template is the cylindrical micelles (or inverse micelles) which are formed by the self-assembly of surfactant molecules at their critical micelle concentration (CMC) as shown in Figure 1.5.[126] This class of soft template is versatile and useful for generating relatively large quantities of 1D nanostructures. Similar to the porous membranes, these surfactant molecules have to be selectively removed to obtain pure 1D nanostructures. As shown in Figure 1.5, this type of template often makes use of the interaction between the precursor and one end of the surfactant molecules. By adjusting the environment of the solution, either micelles or inverse micelles are formed which will then determine whether the materials to-be-formed will grow inside or outside of the cylindrical micelles, forming NWs or NTs respectively. However, it is often difficult and tedious to prepare and remove the micellar phase of the soft template. Based on this principle, various 1D nanostructures were prepared such as gold NRs, tungsten NWs, CdS NTs and NWs.[127-130] Polymer-TiO_2 segmented NWs were also fabricated by using block co-micelle as template.[131] Recently, it was demonstrated that the surfactant can also act as a dopant. As shown by Chowdhury *et al.*,[132] camphor sulfonic acid that was used as surfactant for the growth of PANI NWs were not removed but remained as the dopant which had improved the conductivity of the NWs.

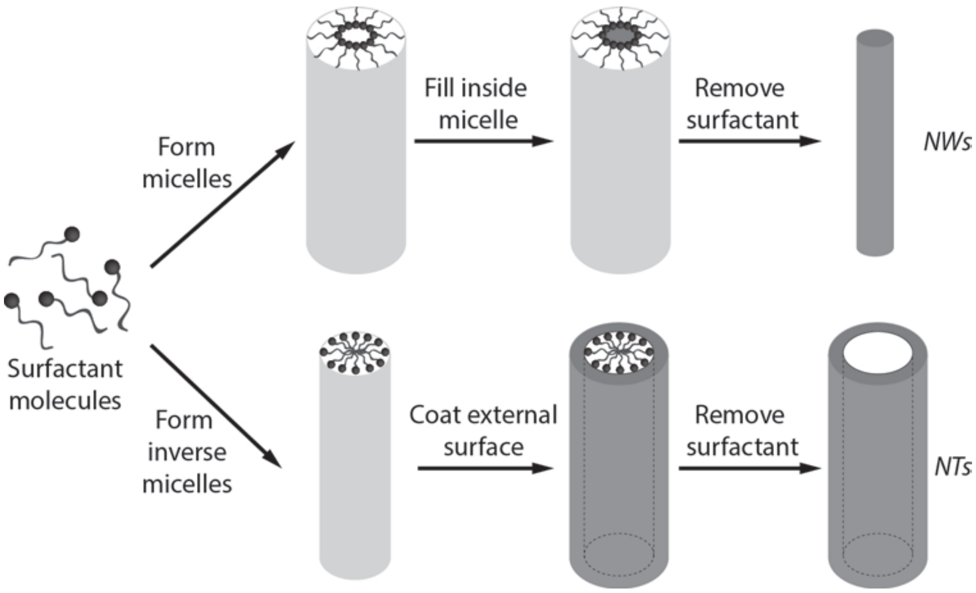

Figure 1.5: Schematic diagram illustrating the formation of NWs and NTs by templating against the cylindrical micelles or inverse micelles, respectively. [Schematics redrawn and adapted from Ref. 51]

Rather than sacrificing the scaffold, existing NWs or NTs can be used as template to fabricate various multi-component 1D nanostructures. The template acts as the deposition surface and will become part of the desired nanostructures. This was vastly demonstrated by the synthesis of CNT/polymer core-shell 1D nanostructures where the polymers were directly deposited onto the surface of CNT.[133-136] Another example is the synthesis of coaxially coated manganese oxide (MnO_2) on vertically aligned carbon nanofiber arrays.[137] Carbon nanofiber array was firstly formed by plasma enhanced chemical vapour deposition (PECVD) and MnO_2 was deposited onto the nanofibers via pulsed electrodeposition. Other than coaxial core-shell nanostructures, various groups have demonstrated the fabrication of hetero-branched NWs using pre-formed NWs as the template.[25]

1.3 Objective and scope of thesis

As illustrated above, anisotropic 1D nanostructures possess enhanced properties and are useful for the miniaturization of electronic, optoelectronic and electrochemical devices. In the exploration of their properties that leads to the realization of their potential applications, it is important to establish our ability to control separately the growth in length and diameter/shell thickness of multi-component 1D nanostructures. Simple and cost-effective synthesis methods are also always preferred for real applications in the industry.

Hence, this project sets out to further explore the use of AAO and aligned multi-walled carbon nanotubes (MWCNT) as templates to grow various single- and multi-component 1D nanostructures. While the use of these templates (especially AAO) has been studied in the literature, our aim is to develop strategies to prepare unique 1D architectures in a simple and direct manner through these readily obtainable templates. In the selection of materials, we have chosen to investigate materials with potentials in optical and electrochemical applications. Chapter 2 contains all necessary experimental procedures for the syntheses, characterizations and properties measurements of these 1D nanostructures obtained. Electrochemical deposition technique was used as the main fabrication method because of its ease in controlling the type and length of NWs or NTs produced via the applied potentials, the variety of electro-active materials and electrolytes, and the duration of deposition.

In Chapter 3, we established optimal parameters to electrodeposit poly(*p*-phenylene vinylene) (PPV) into AAO nanochannels to give luminescent organic 1D nanostructures. To the best of our knowledge, this is the first report on the synthesis of PPV 1D nanostructures via template-assisted electrodeposition method. Compared to reported syntheses of PPV 1D nanostructures that were based on precursor method,[138, 139] our method is less tedious as it does not require post-treatment of samples. In this Chapter, we show that both PPV NWs and NTs can be prepared by manipulating the purity of the plating solution and deposition potentials, while their length can be readily controlled by the electrodeposition duration. In addition, we also demonstrate the ability of micro-patterning the PPV arrays via focused laser beam technique. An interesting "red-shifting" of the photoluminescence maxima was observed upon laser modification in air but not in an inert environment.

To further demonstrate the versatility of AAO as shape-directing template, Chapter 4 presents a "Pore Widening" method that we have developed to fabricate coaxial multi-layered 1D hetero-nanostructures. In this method, a mild etching reagent was used to controllably etch away the channel walls of AAO, creating annular gaps around the deposited core wires for subsequent deposition of shells. With judicious selection of materials and sequences of steps, a few strategies are illustrated, leading to the fabrication of various hetero-nanostructures such as polymer/metal, metal/metal, polymer/metal/metal and metal oxide/metal core-shell nanostructures.

AAO can be more than just a sacrificial template for the deposition of 1D nanostructures. In Chapter 5, we describe an application of AAO to fabricate cobalt-aluminium layered double hydroxides (Co/Al-LDH) hierarchical nanostructures. Here, the AAO not only acts as template, but also provides Al^{3+} ions in the alkaline solution that isomorphously substitute some of the Co^{2+} ions during the hydroxide formation. The resulting nanostructures consists of Co/Al-LDH nanoflakes (NFs) supported onto cobalt NWs. Since these arrays are directly grown onto current collector, they can be readily used as electrode for electrochemical capacitor and glucose sensing applications without the need of binder. The effects of alkaline treatment on the LDH NFs in terms of their morphology and Al content were studied and will be discussed in this Chapter.

In the last result chapter, Chapter 6 describes the use of aligned MWCNT as support for the growth of 1D nanostructures. The electropolymerization conditions established in Chapter 3 was adapted to coaxially grow PPV onto each strands of MWCNT, forming arrays of aligned MWCNT/PPV core-shell nanostructures. Both constant potentiometry and pulsed potentiometry were applied and the latter was found to show better control of the shell thickness. The photocurrent responses of the resulting nanostructures were investigated with 405 nm laser.

Lastly, Chapter 7 gives an overall conclusion of the thesis work. Some future outlook and further exploration are also proposed here.

1.4 References

1. A. S. Arico, P. Bruce, B. Scrosati, J. M. Tarascon, W. Van Schalkwijk. *Nat. Mater.* **4** (2005) 366-377.
2. H. E. Jeong, K. Y. Suh. *Nano Today* **4** (2009) 335-346.
3. Q. F. Zhang, G. Z. Cao. *Nano Today* **6** (2011) 91-109.
4. P. Si, Y. J. Huang, T. H. Wang, J. M. Ma. *RSC Adv.* **3** (2013) 3487-3502.
5. H. Weller. *Adv. Mater.* **5** (1993) 88-95.
6. H. Weller. *Angew. Chem. Int. Ed. Engl.* **32** (1993) 41-53.
7. C. Liu, Z. J. Zhang. *Chem. Mater.* **13** (2001) 2092-2096.
8. Y. W. Jun, Y. M. Huh, J. S. Choi, J. H. Lee, H. T. Song, S. Kim, S. Yoon, K. S. Kim, J. S. Shin, J. S. Suh, J. Cheon. *J. Am. Chem. Soc.* **127** (2005) 5732-5733.
9. V. V. Pokropivny, V. V. Skorokhod. *Mater. Sci. Eng., C* **27** (2007) 990-993.
10. U. K. Gautam, S. R. C. Vivekchand, A. Govindaraj, G. U. Kulkarni, N. R. Selvi, C. N. R. Rao. *J. Am. Chem. Soc.* **127** (2005) 3658-3659.
11. G. Zhang, D. Y. Wang. *J. Am. Chem. Soc.* **130** (2008) 5616-5617.
12. Y. T. Kim, J. H. Han, B. H. Hong, Y. U. Kwon. *Adv. Mater.* **22** (2010) 515-518.
13. J. M. Park, K. S. Nalwa, W. Leung, K. Constant, S. Chaudhary, K. M. Ho. *Nanotechnology* **21** (2010) 215301.
14. G. R. Li, Z. P. Feng, J. H. Zhong, Z. L. Wang, Y. X. Tong. *Macromolecules* **43** (2010) 2178-2183.

15. J. Y. Chen, N. Ahmad, D. W. Shi, W. P. Zhou, X. F. Han. *J. Appl. Phys.* **110** (2011) 073912.
16. X. H. Xia, J. P. Tu, Y. Q. Zhang, X. L. Wang, C. D. Gu, X. B. Zhao, H. J. Fan. *ACS Nano* **6** (2012) 5531-5538.
17. D. Panda, T. Y. Tseng. *J. Mater. Sci.* **48** (2013) 6849-6877.
18. X. Y. Dong, X. H. Ji, J. Jing, M. Y. Li, J. Li, W. S. Yang. *J. Phys. Chem. C* **114** (2010) 2070-2074.
19. A. K. P. Mann, S. E. Skrabalak. *Chem. Mater.* **23** (2011) 1017-1022.
20. P. F. Siril, L. Ramos, P. Beaunier, P. Archirel, A. Etcheberry, H. Remita. *Chem. Mater.* **21** (2009) 5170-5175.
21. S. Vizireanu, S. D. Stoica, C. Luculescu, L. C. Nistor, B. Mitu, G. Dinescu. *Plasma Sources Sci. Technol.* **19** (2010) 034016.
22. L. Wang, Y. Yamauchi. *Chem. Mater.* **21** (2009) 3562-3569.
23. J. N. Wang, L. F. Su, Z. P. Wu. *Cryst. Growth Des.* **8** (2008) 1741-1747.
24. W. W. Lei, D. Liu, J. Zhang, P. W. Zhu, Q. L. Cui, G. T. Zou. *Cryst. Growth Des.* **9** (2009) 1489-1493.
25. C. W. Cheng, H. J. Fan. *Nano Today* **7** (2012) 327-343.
26. S. Iijima. *Nature* **354** (1991) 56-58.
27. M. R. Gao, W. H. Xu, L. B. Luo, Y. J. Zhan, S. H. Yu. *Adv. Mater.* **22** (2010) 1977-1981.
28. J. Xu, K. M. Razeeb, S. K. Sitaraman, A. Mathewson. *2012 12th IEEE Conference on Nanotechnology (IEEE-Nano)* (2012).

29. M. D. Brubaker, P. T. Blanchard, J. B. Schlager, A. W. Sanders, A. Roshko, S. M. Duff, J. M. Gray, V. M. Bright, N. A. Sanford, K. A. Bertness. *Nano Lett.* **13** (2013) 374-377.

30. C. R. Sides, C. R. Martin. *Adv. Mater.* **17** (2005) 125-128.

31. D. W. Su, H. J. Ahn, G. Wang. *J. Power Sources* **244** (2013) 742-746.

32. J. Ha, U. Paik. *J. Power Sources* **244** (2013) 463-468.

33. J. P. Wang, D. H. Zhang. *Adv. Polym. Tech.* **32** (2013) E323-E368.

34. Y. Q. Hao, B. B. Zhou, F. B. Wang, J. Li, L. Deng, Y. N. Liu. *Biosens. Bioelectron.* **52** (2014) 422-426.

35. G. D. Sulka, K. Hnida, A. Brzozka. *Electrochim. Acta* **104** (2013) 536-541.

36. V. Callegari, S. Demoustier-Champagne. *Macromol. Rapid Commun.* **32** (2011) 25-34.

37. H. J. Chung, H. H. Jung, Y. S. Cho, S. Lee, J. H. Ha, J. H. Choi, Y. Kuk. *Appl. Phys. Lett.* **86** (2005) 213113.

38. Y. G. Guo, L. J. Wan, C. F. Zhu, D. L. Yang, D. M. Chen, C. L. Bai. *Chem. Mater.* **15** (2003) 664-667.

39. H. P. Liang, Y. G. Guo, J. S. Hu, C. F. Zhu, L. J. Wan, C. L. Bai. *Inorg. Chem.* **44** (2005) 3013-3015.

40. B. Z. Tian, X. L. Zheng, T. J. Kempa, Y. Fang, N. F. Yu, G. H. Yu, J. L. Huang, C. M. Lieber. *Nature* **449** (2007) 885-890.

41. X. H. Xia, J. S. Luo, Z. Y. Zeng, C. Guan, Y. Q. Zhang, J. P. Tu, H. Zhang, H. J. Fan. *Sci. Rep.* **2** (2012) 981.

42. C. Y. Yan, H. Jiang, T. Zhao, C. Z. Li, J. Ma, P. S. Lee. *J. Mater. Chem.* **21** (2011) 10482-10488.

43. K. M. Fang, Y. Y. Yang, L. Y. Fu, H. T. Zheng, J. H. Yuan, L. Niu. *Sensors and Actuators B-Chemical* **191** (2014) 401-407.

44. N. I. Kovtyukhova, T. E. Mallouk, T. S. Mayer. *Adv. Mater.* **15** (2003) 780-785.

45. J. C. Bao, K. Y. Wang, Z. Xu, H. Zhang, Z. H. Lu. *Chem. Commun.* (2003) 208-209.

46. S. Y. Bae, H. W. Seo, H. C. Choi, D. S. Han, J. Park. *J. Phys. Chem. B* **109** (2005) 8496-8502.

47. L. Li, Y. W. Yang, G. H. Li, L. D. Zhang. *Small* **2** (2006) 548-553.

48. M. Lahav, E. A. Weiss, Q. B. Xu, G. M. Whitesides. *Nano Lett.* **6** (2006) 2166-2171.

49. Y. C. Zhu, Y. Bando, D. F. Xue, F. F. Xu, D. Golberg. *J. Am. Chem. Soc.* **125** (2003) 14226-14227.

50. N. I. Kovtyukhova, B. K. Kelley, T. E. Mallouk. *J. Am. Chem. Soc.* **126** (2004) 12738-12739.

51. Y. N. Xia, P. D. Yang, Y. G. Sun, Y. Y. Wu, B. Mayers, B. Gates, Y. D. Yin, F. Kim, Y. Q. Yan. *Adv. Mater.* **15** (2003) 353-389.

52. A. J. Mieszawska, R. Jalilian, G. U. Sumanasekera, F. P. Zamborini. *Small* **3** (2007) 722-756.

53. J. Y. Chun, J. W. Lee. *Eur. J. Inorg. Chem.* (2010) 4251-4263.

54. J. N. Tiwari, R. N. Tiwari, K. S. Kim. *Prog. Mater Sci.* **57** (2012) 724-803.

55. L. M. Cao, H. Tian, Z. Zhang, X. Y. Zhang, C. X. Gao, W. K. Wang. *Nanotechnology* **15** (2004) 139-142.

56. X. M. Yan, S. Kwon, A. M. Contreras, J. Bokor, G. A. Somorjai. *Nano Lett.* **5** (2005) 745-748.

57. J. H. Golden, F. J. DiSalvo, J. M. J. Frechet, J. Silcox, M. Thomas, J. Elman. *Science* **273** (1996) 782-784.

58. L. Venkataraman, C. M. Lieber. *Phys. Rev. Lett.* **83** (1999) 5334-5337.

59. B. Gates, B. Mayers, B. Cattle, Y. N. Xia. *Adv. Funct. Mater.* **12** (2002) 219-227.

60. B. Mayers, Y. N. Xia. *J. Mater. Chem.* **12** (2002) 1875-1881.

61. M. Hanack, M. Lang. *Adv. Mater.* **6** (1994) 819-833.

62. H. S. Nalwa. *Appl. Organomet. Chem.* **4** (1990) 91-102.

63. T. J. Marks. *Angew. Chem. Int. Ed. Engl.* **29** (1990) 857-879.

64. R. S. Wagner, W. C. Ellis. *Appl. Phys. Lett.* **4** (1964) 89-90.

65. Y. Y. Wu, P. D. Yang. *J. Am. Chem. Soc.* **123** (2001) 3165-3166.

66. M. S. Gudiksen, C. M. Lieber. *J. Am. Chem. Soc.* **122** (2000) 8801-8802.

67. Y. Y. Wu, H. Q. Yan, M. Huang, B. Messer, J. H. Song, P. D. Yang. *Chem. Eur. J.* **8** (2002) 1261-1268.

68. Y. J. Zhang, Q. Zhang, N. L. Wang, Y. J. Yan, H. H. Zhou, J. Zhu. *J. Cryst. Growth* **226** (2001) 185-191.

69. L. W. Yu, L. Rigutti, M. Tchernycheva, S. Misra, M. Foldyna, G. Picardi, P. R. I. Cabarrocas. *Nanotechnology* **24** (2013).

70. Y. Y. Wu, P. D. Yang. *Chem. Mater.* **12** (2000) 605-607.

71. C. C. Chen, C. C. Yeh, C. H. Chen, M. Y. Yu, H. L. Liu, J. J. Wu, K. H. Chen, L. C. Chen, J. Y. Peng, Y. F. Chen. *J. Am. Chem. Soc.* **123** (2001) 2791-2798.

72. W. S. Shi, Y. F. Zheng, N. Wang, C. S. Lee, S. T. Lee. *J. Vac. Sci. Technol., B* **19** (2001) 1115-1118.

73. Y. W. Wang, L. D. Zhang, C. H. Liang, G. Z. Wang, X. S. Peng. *Chem. Phys. Lett.* **357** (2002) 314-318.

74. Y. W. Wang, G. W. Meng, L. D. Zhang, C. H. Liang, J. Zhang. *Chem. Mater.* **14** (2002) 1773-1777.

75. M. H. Huang, Y. Y. Wu, H. Feick, N. Tran, E. Weber, P. D. Yang. *Adv. Mater.* **13** (2001) 113-116.

76. X. C. Wu, W. H. Song, K. Y. Wang, T. Hu, B. Zhao, Y. P. Sun, J. J. Du. *Chem. Phys. Lett.* **336** (2001) 53-56.

77. T. J. Kempa, J. F. Cahoon, S. K. Kim, R. W. Day, D. C. Bell, H. G. Park, C. M. Lieber. *Proc. Natl. Acad. Sci. U.S.A.* **109** (2012) 1407-1412.

78. L. V. Podrezova, S. Porro, V. Cauda, M. Fontana, G. Cicero. *Appl. Phys. A: Mater. Sci. Process.* **113** (2013) 623-632.

79. T. J. Trentler, K. M. Hickman, S. C. Goel, A. M. Viano, P. C. Gibbons, W. E. Buhro. *Science* **270** (1995) 1791-1794.

80. H. Yu, W. E. Buhro. *Adv. Mater.* **15** (2003) 416-419.

81. H. Yu, J. B. Li, R. A. Loomis, L. W. Wang, W. E. Buhro. *Nat. Mater.* **2** (2003) 517-520.

82. D. D. Fanfair, B. A. Korgel. *Cryst. Growth Des.* **5** (2005) 1971-1976.

83. F. D. Wang, V. L. Wayman, R. A. Loomis, W. E. Buhro. *ACS Nano* **5** (2011) 5188-5194.

84. N. Petchsang, L. Shapoval, F. Vietmeyer, Y. H. Yu, J. H. Hodak, I. M. Tang, T. H. Kosel, M. Kuno. *Nanoscale* **3** (2011) 3145-3151.

85. H. Yu, J. B. Li, R. A. Loomis, P. C. Gibbons, L. W. Wang, W. E. Buhro. *J. Am. Chem. Soc.* **125** (2003) 16168-16169.

86. J. W. Grebinski, K. L. Hull, J. Zhang, T. H. Kosel, M. Kuno. *Chem. Mater.* **16** (2004) 5260-5272.

87. Z. Wang, Z. Li, A. Kornowski, X. D. Ma, A. Myalitsin, A. Mews. *Small* **7** (2011) 2464-2468.

88. L. Ouyang, K. N. Maher, C. L. Yu, J. McCarty, H. Park. *J. Am. Chem. Soc.* **129** (2007) 133-138.

89. W. C. Kwak, T. G. Kim, W. J. Lee, S. H. Han, Y. M. Sung. *J. Phys. Chem. C* **113** (2009) 1615-1619.

90. R. Laocharoensuk, K. Palaniappan, N. A. Smith, R. M. Dickerson, D. J. Werder, J. K. Baldwin, J. A. Hollingsworth. *Nat. Nanotechnol.* **8** (2013) 660-666.

91. A. Dorn, C. R. Wong, M. G. Bawendi. *Adv. Mater.* **21** (2009) 3479-3482.

92. A. Dorn, P. M. Allen, M. G. Bawendi. *ACS Nano* **3** (2009) 3260-3265.

93. Y. J. Hsu, S. Y. Lu. *Chem. Commun.* (2004) 2102-2103.

94. Y. J. Hsu, S. Y. Lu, Y. F. Lin. *Adv. Funct. Mater.* **15** (2005) 1350-1357.

95. Y. W. Heo, M. Kaufman, K. Pruessner, K. N. Siebein, D. P. Norton, F. Ren. *Appl. Phys. A: Mater. Sci. Process.* **80** (2005) 263-266.

96. Y. W. Heo, C. Abernathy, K. Pruessner, W. Sigmund, D. P. Norton, M. Overberg, F. Ren, M. F. Chisholm. *J. Appl. Phys.* **96** (2004) 3424-3428.

97. W. S. Jang, S. Y. Kim, J. Lee, J. Park, C. J. Park, C. J. Lee. *Chem. Phys. Lett.* **422** (2006) 41-45.

98. W. Q. Han, A. Zettl. *Appl. Phys. Lett.* **81** (2002) 5051-5053.

99. Y. Y. Wu, R. Fan, P. D. Yang. *Nano Lett.* **2** (2002) 83-86.

100. L. J. Lauhon, M. S. Gudiksen, C. L. Wang, C. M. Lieber. *Nature* **420** (2002) 57-61.

101. A. G. Dong, F. D. Wang, T. L. Daulton, W. E. Buhro. *Nano Lett.* **7** (2007) 1308-1313.

102. Z. Li, X. D. Ma, Q. A. Sun, Z. Wang, J. A. Liu, Z. H. Zhu, S. Z. Qiao, S. C. Smith, G. Q. Lu, A. Mews. *Eur. J. Inorg. Chem.* (2010) 4325-4331.

103. Y. M. Sung, W. C. Kwak, T. G. Kim. *Crystengcomm* **14** (2012) 389-392.

104. J. A. Venables. *Introduction to Surface and Thin Film Processes*. Cambridge University Press, Cambridge (2000) pp. 4.

105. Z. L. Wang. *J. Phys. Chem. B* **104** (2000) 1153-1175.

106. J. H. Yu, J. Joo, H. M. Park, S. I. Baik, Y. W. Kim, S. C. Kim, T. Hyeon. *J. Am. Chem. Soc.* **127** (2005) 5662-5670.

107. Y. G. Sun, Y. D. Yin, B. T. Mayers, T. Herricks, Y. N. Xia. *Chem. Mater.* **14** (2002) 4736-4745.

108. Z. H. Zhang, S. H. Lee, J. J. Vittal, W. S. Chin. *J. Phys. Chem. B* **110** (2006) 6649-6654.

109. Z. H. Zhang, M. H. Lu, H. R. Xu, W. S. Chin. *Chem. Eur. J.* **13** (2007) 632-638.

110. C. R. Martin. *Science* **266** (1994) 1961-1966.

111. C. R. Martin. *Chem. Mater.* **8** (1996) 1739-1746.

112. J. C. Hulteen, C. R. Martin. *J. Mater. Chem.* **7** (1997) 1075-1087.

113. S. J. Hurst, E. K. Payne, L. D. Qin, C. A. Mirkin. *Angew. Chem. Int. Edit.* **45** (2006) 2672-2692.

114. R. O. Al-Kaysi, T. H. Ghaddar, G. Guirado. *J. Nanomater.* (2009).

115. F. Massuyeau, J. L. Duvail, H. Athalin, J. M. Lorcy, S. Lefrant, J. Wery, E. Faulques. *Nanotechnology* **20** (2009) 155701.

116. C. Wee Shong, P. Weicheng, K. Fong Yu, L. Chenmin, L. Pui Yee. *COSMOS* **06** (2010) 221-234.

117. K. R. Lee, Y. U. Kwon. *Nano* **5** (2010) 75-87.

118. Q. P. Wang, F. F. Min, J. B. Zhu. *Mater. Lett.* **91** (2013) 9-11.

119. R. Elnathan, R. Kantaev, F. Patolsky. *Nano Lett.* **8** (2008) 3964-3972.

120. R. Liu, J. Duay, S. B. Lee. *ACS Nano* **5** (2011) 5608-5619.

121. X. D. Li, G. W. Meng, Q. L. Xu, M. G. Kong, X. G. Zhu, Z. Q. Chu, A. P. Li. *Nano Lett.* **11** (2011) 1704-1709.

122. S. F. Hou, C. C. Harrell, L. Trofin, P. Kohli, C. R. Martin. *J. Am. Chem. Soc.* **126** (2004) 5674-5675.

123. D. Z. Zhang, L. A. Luo, Q. Liao, H. Wang, H. B. Fu, J. N. Yao. *J. Phys. Chem. C* **115** (2011) 2360-2365.

124. H. Z. Wang, Y. Song, W. H. Liu, S. W. Yao, W. G. Zhang. *Mater. Lett.* **93** (2013) 319-321.

125. J. H. Dai, Q. Liu, L. Wang, P. W. Wu, X. Huang, Z. B. Zhu, J. T. Tian. *Mater. Lett.* **107** (2013) 333-336.

126. H. Ringsdorf, B. Schlarb, J. Venzmer. *Angew. Chem. Int. Edit.* **27** (1988) 113-158.

127. Y. J. Xiong, Y. Xie, J. Yang, R. Zhang, C. Z. Wu, G. Du. *J. Mater. Chem.* **12** (2002) 3712-3716.

128. Y. Y. Yu, S. S. Chang, C. L. Lee, C. R. C. Wang. *J. Phys. Chem. B* **101** (1997) 6661-6664.

129. Y. D. Li, X. L. Li, Z. X. Deng, B. C. Zhou, S. S. Fan, J. W. Wang, X. M. Sun. *Angew. Chem. Int. Edit.* **41** (2002) 333-335.

130. X. H. Yang, Q. S. Wu, L. Li, Y. P. Ding, G. X. Zhang. *Colloids Surf., A* **264** (2005) 172-178.

131. H. Wang, A. J. Patil, K. Liu, S. Petrov, S. Mann, M. A. Winnik, I. Manners. *Adv. Mater.* **21** (2009) 1805-1808.

132. D. Chowdhury. *J. Phys. Chem. C* **115** (2011) 13554-13559.

133. M. Hughes, M. S. P. Shaffer, A. C. Renouf, C. Singh, G. Z. Chen, J. Fray, A. H. Windle. *Adv. Mater.* **14** (2002) 382-385.

134. Q. Peng, Z. H. Wen, G. S. Zeng, J. P. Zou, S. Q. Lu. *Chem. Lett.* **38** (2009) 380-381.

135. Y. P. Fang, J. W. Liu, D. J. Yu, J. P. Wicksted, K. Kalkan, C. O. Topal, B. N. Flanders, J. D. Wu, J. Li. *J. Power Sources* **195** (2010) 674-679.

136. X. X. Bai, X. J. Hu, S. Y. Zhou, J. Yan, C. H. Sun, P. Chen, L. F. Li. *Electrochim. Acta* **87** (2013) 394-400.

137. J. W. Liu, J. Essner, J. Li. *Chem. Mater.* **22** (2010) 5022-5030.

138. W. Zhang, Z. H. Huang, E. Y. Yan, C. Wang, Y. Xin, Q. Zhao, Y. B. Tong. *Mater. Sci. Eng., A* **443** (2007) 292-295.

139. Y. Xin, Z. B. Ling, S. Y. Li, T. T. Lin, G. D. Liu. *Mater. Sci. Eng., B* **177** (2012) 1094-1097.

Chapter 2

Experimental

2.1 List of chemicals and reagents

Table 2.1: Chemicals and solvents used in the work described in this thesis.

Chemical	Purity	Formula	Source
α,α,α’,α’-tetrabromo-*p*-xylene (TBX)	98%	$(C_6H_4)(CHBr_2)_2$	TCI
Tetraethylammonium tetrafluoroborate (Et_4NBF_4)	99%	$(CH_3CH_2)_4NBF_4$	Alfa Aesar
Acetonitrile (ACN)	HPLC grade	CH_3CN	Fisher Chemicals
Sodium hydroxide	99-100%	NaOH	Chemicon Laboratory Reagent
Cobalt (II) sulfate heptahydrate	99%	$CoSO_4.7H_2O$	Riedel-De Haën Ag Seelze-Hannover
Cobalt (II) nitrate hexahydrate	≥ 97%	$Co(NO_3)_2.6H_2O$	Hayashi Pure Chemical Industries Ltd.
Nickel (II) sulfate hexahydrate	100%	$NiSO_4.6H_2O$	VWR
Nickel (II) chloride hexahydrate	98%	$NiCl_2.6H_2O$	Merck
Boric acid	99.8%	H_3BO_3	Merck
Potassium hydroxide	85%	KOH	GCE Laboratory Chemicals
L-Ascorbic acid (AA)	99%	$C_6H_8O_6$	Alfa Aesar
Uric acid (UA)	99%	$C_5H_4N_4O_3$	Sigma
Pyrrole	99%	C_4H_5N	Acros

2.2 Synthesis of 1D nanostructures using AAO as template

In this thesis, the nanostructures were primarily fabricated using electrochemical deposition method with AAO as hard template. AAO nanopore membranes were obtained as Anodisc 47 from Whatman Co., pore size ≈ 0.2 μm, thickness ≈ 60 μm, pore density ≈ 10^9 pores/cm^2. All electrodeposition was carried out using Autolab PGSTAT30 potentiostat/galvanostat. A platinum rod was used as the counter electrode (CE) and Ag/AgCl (3 M KCl) or Ag/AgCl (saturated LiCl/EtOH) [0.143 V vs SHE] as the reference electrode (RE) for aqueous and non-aqueous plating solution, respectively. A thin layer of gold sputtered on one side of the AAO prior to electrodeposition served as the working electrode (WE) after making contact with copper foil in the Teflon cell. A hole of about 0.785 cm^2 (diameter = 1 cm) in the Teflon cell defined the area of AAO membrane that was in contact with the plating solution. Kalrez® rubber O-ring was used to prevent leakage of plating solution into the Teflon cell. This formed a three-electrode configuration for electrodeposition as illustrated in Figure 2.1.

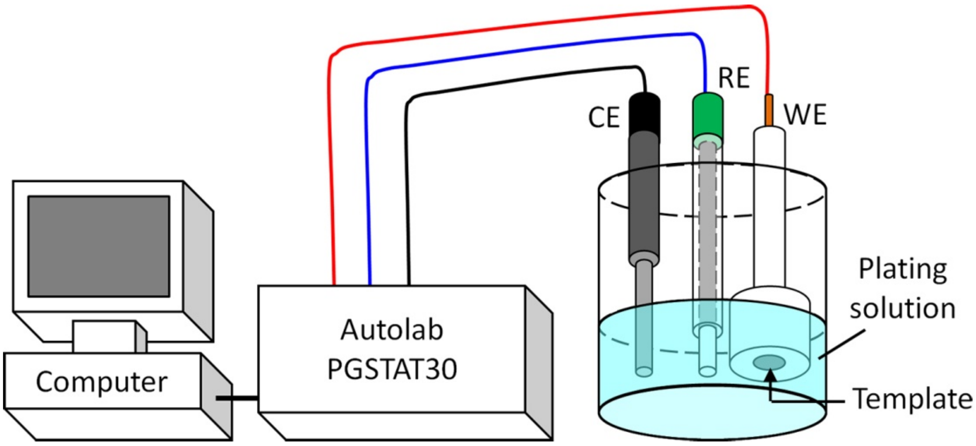

Figure 2.1: Three-electrode configuration setup for electrochemical deposition of nanostructures and measurements of electrochemical properties.

2.2.1 Synthesis of PPV 1D nanostructures

Three-electrode configuration as illustrated in Figure 2.1 was employed for the electrodeposition of PPV 1D nanostructures. The plating solution consisted of 30 mM α,α,α',α'-tetrabromo-*p*-xylene (TBX) and 0.12M tetraethylammonium tetrafluoroborate (Et_4NBF_4) in 30 mL of acetonitrile (ACN).[1] Since the plating solution was non-aqueous, the RE used is Ag/AgCl (saturated LiCl/EtOH) [0.143V vs SHE]. Constant cathodic potential of -2.34 V was applied for fabrication of PPV 1D nanostructures. We have found that the presence of oxygen and moisture from the air has an effect on the morphology of the PPV nanostructures obtained (Section 3.1.1). Thus, some synthesis was performed with plating solution prepared using freshly distilled ACN as solvent. This plating solution was purged with dry N_2 gas prior to electrodeposition. During electrodeposition, the solution was not purged to prevent disturbance due to bubbling but a blanket of dry N_2 gas was maintained on top of the solution with continuous flow of N_2 gas. In order to study the effect of applied potential on the morphology of PPV nanostructures in Section 3.1.2, constant potentials ranging from -1.74 V to -2.74 V was chosen to electropolymerize PPV into the pores of AAO template. After electrodeposition, the template was removed by soaking in 0.5 M NaOH solution for 1 hour to give free-standing array of 1D nanostructures on the thin gold substrate. A schematic diagram of the template-assisted synthesis of PPV nanowires (NWs) or nanotubes (NTs) is illustrated in Figure 2.2.

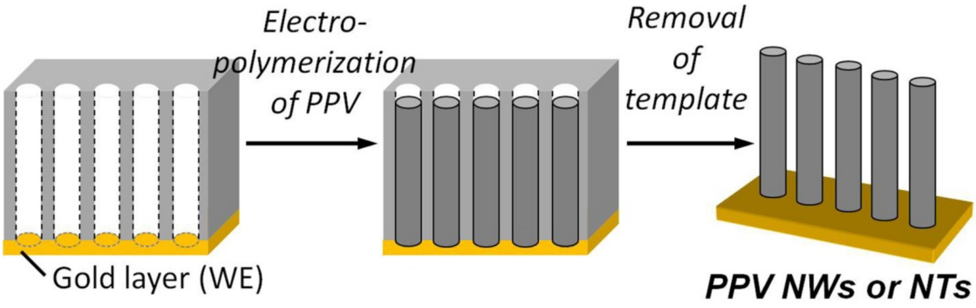

Figure 2.2: Schematic diagram for the synthesis of PPV 1D nanostructures by electrodeposition using AAO as template.

2.2.2 Electrodeposition of polypyrrole and metallic components for core-shell 1D nanostructures

Three-electrode configuration as illustrated in Figure 2.1 was employed for the electrodeposition of multi-layered core-shell 1D nanostructures in Chapter 4. Depending on the material of interest to be deposited, the plating solution and deposition parameters used would be changed accordingly.

For electrodeposition of polypyrrole (PPy), plating solution used consists of 0.3 M pyrrole and 0.12 M Et_4NBF_4 with 30 mL ACN as the solvent. Electrodeposition was carried out at constant potential +1.064V vs Ag/AgCl (saturated LiCl/EtOH), with charges passed through of 1.0 C.

For nickel (Ni) component, electrodeposition was carried out under a constant cathodic current density of -5 mA/cm^2 from a typical Watts bath consisting of 165 g/L $NiSO_4 \cdot 6H_2O$, 22.5 g/L $NiCl_2 \cdot 6H_2O$ and 37 g/L H_3BO_3, adjusted to pH 3-4 with H_2SO_4.[2]

Lastly, electrodeposition of copper (Cu) was achieved at a constant cathodic current density of -2 mA/cm^2 from a copper complex aqueous solution consisting of 80 g/L $CuSO_4 \cdot 5H_2O$, 120 g/L ethylenediamine and 20 g/L $KNaC_4H_4O_6 \cdot 4H_2O$.

2.2.3 Synthesis of Co/Al layered double hydroxides hierarchical 1D nanostructures

Three-electrode configuration as illustrated in Figure 2.1 was also employed for the fabrication of hierarchical nanostructures of Co/Al layered double hydroxides (Co/Al-LDH) nanoflakes (NFs) supported on Co NWs. Firstly, Co NWs were deposited into the nanochannels of AAO template at a constant cathodic current of -1.5 mA from 30 mL aqueous solution consisted of 266 g/L $CoSO_4 \cdot 7H_2O$ and 40 g/L H_3BO_3. Since the plating solution was aqueous, the RE used is Ag/AgCl (3M KCl). Subsequently, the Co NWs in AAO was rinsed with deionized water and immersed into 30 mL of 2.5 M NaOH for 1, 18, 24 and 48 hours. These durations of immersion were chosen to study the effect of alkaline treatment time in Section 5.1. The alkaline treatment would remove AAO and form Co/Al-LDH NFs at the same time. This procedure was adapted from Lee *et al*. which reported the fabrication of CoOOH NFs on Co foil using alkaline treatment in a stirred solution.[3, 4] A schematic of the synthesis process is illustrated in Figure 2.3.

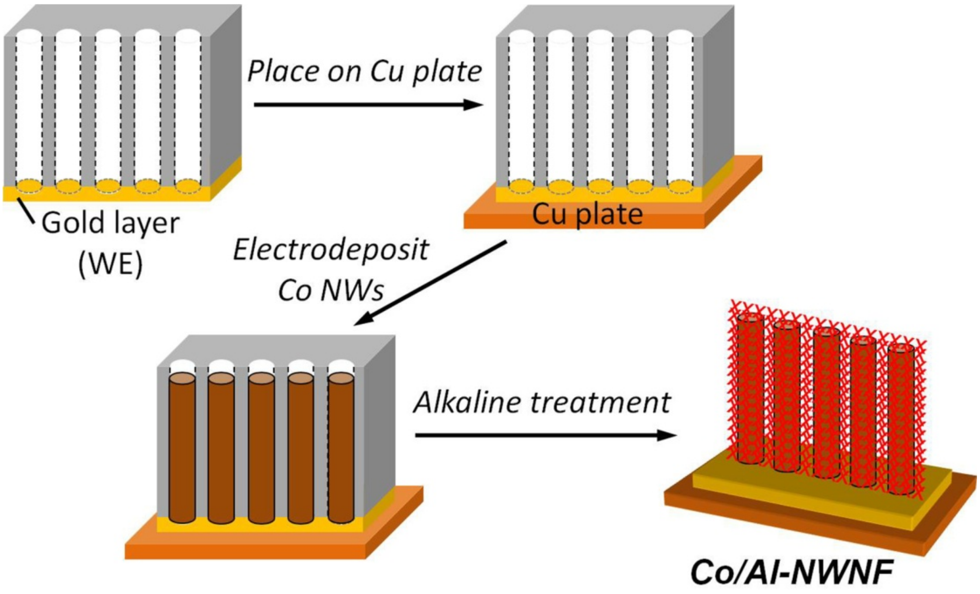

Figure 2.3: Schematic diagram for the fabrication of Co/Al-LDH hierarchical nanostructures using AAO as template and source of Al^{3+} ions.

2.3 Synthesis of 1D nanostructures using aligned MWCNT as template

In this study, aligned multi-walled carbon nanotubes (MWCNT) was used as a supporting template for deposition. Here, array of aligned MWCNT was first prepared on a silicon (Si) substrate, followed by electropolymerization of PPV onto the MWCNT. The synthesis strategy is shown in Figure 2.4.

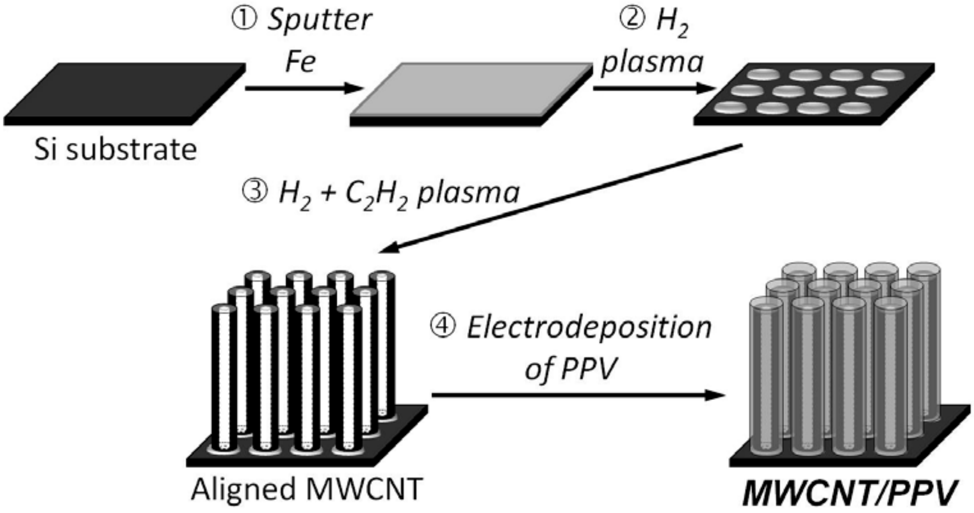

Figure 2.4: Schematic diagram for the growth of MWCNT/PPV core-shell nanostuctures on *n*-type Si via PECVD followed by electrochemical method.

2.3.1 Synthesis of aligned MWCNT arrays

The arrays of aligned MWCNT was grown using plasma-enhanced chemical vapour deposition (PECVD) technique[5] with iron (Fe) nanoparticles as catalyst on 1.3 × 1.3 cm *n*-type Si (100) (doping thickness 500 ± 25 μm, resistivity 1-30 Ω-cm). Before use, the substrates were cleaned by ultrasonic bath in acetone for 15 minutes, followed by deionised water for another 5 minutes to remove organic residues and acetone, respectively. The substrates were then blown dry with nitrogen gas. Then, the cleaned substrates were subjected to radio frequency (RF) magnetron sputtering machine to coat a thin layer of Fe catalyst (about 5 nm thickness) as shown in Figure 2.4 Step 1. Sputtering was carried out at 100 W under argon gas flow of 20 sccm and process pressure of 12 mTorr for 1 minute after reaching a vacuum of 2.6×10^{-6} Torr. Rotation of stage was set to be at about 12 rpm.

Subsequently, the substrates were transferred into an RF (13.56MHz) PECVD system where the MWCNT was grown. Once the chamber has reached vacuum level about 1×10^{-5} Torr, the temperature for the chamber and substrates were set at 400 ^{o}C and 720 ^{o}C, respectively. Next, the chamber was conditioned with H_2 gas (55 sccm) at pressure of 500 mTorr for 4 minutes. The growth of MWCNT then proceed via two processes: (1) The Fe layer on Si was etched and reduced by H_2 plasma (55 sccm, RF power 80 W) at substrate temperature of 720 ^{o}C and process pressure of 500 mTorr for 10 minutes to form islands of elemental Fe catalyst as shown in Figure 2.4 Step 2. (2) A mixture of C_2H_2 (22 sccm) and H_2 (55 sccm) gases was introduced into the chamber at substrate temperature of 720 ^{o}C, working pressure of 1200 mTorr and RF power of 100 W for growth of MWCNT as shown in Figure 2.4 Step 3. The growth duration was set to 1 hour. Finally, the system was cooled down to room temperature and vented to atmospheric pressure before the samples were removed.

2.3.2 Synthesis of aligned MWCNT/PPV core-shell nanowires

Using the arrays of aligned MWCNT as-prepared in Section 2.3.1, MWCNT/PPV core-shell NWs were prepared by coating PPV onto the MWCNT via electrochemical method as shown in Figure 2.4 Step 4. The synthesis setup and conditions were similar to that for the synthesis of PPV nanostructures in Section 2.2.1. Electrodeposition of PPV was carried out via the three-electrode configuration as shown in Figure 2.1 with the MWCNT array on Si substrate as WE. A copper tape was used to connect the conductive surface of the *n*-type Si to the copper foil in the Teflon cell to ensure good electrical connection to the MWCNT array, as the bottom side of the substrate was not conductive. The same plating solution as that in Section 2.2.1 was employed (30 mM TBX and 0.12 M Et_4NBF_4) with the ACN solvent distilled prior to use and the plating solution purged with nitrogen (N_2) before electrodeposition. A blanket of N_2 gas was maintained on top of the solution during electrodeposition to provide a dry and oxygen-free environment, preventing interferences from the reduction of H_2O and O_2 during the synthesis. Optimum parameters for the electrodeposition of PPV are further discussed in Chapter 6.

2.4 Micro-patterning of PPV 1D nanostructures array via laser pruning technique

The well-formed PPV nanostructures arrays were subjected to micro-patterning using laser pruning technique. Details of this technique have been reported elsewhere.[6] In brief, a parallel beam of laser was directed into a conventional optical microscope whereby it was focused to a tight spot by the objective lens of the optical microscope system. With the sample sitting on computer controlled stage, a wide variety of micro patterns could be readily created. A schematic of the optical microscope-focused laser beam system set-up is shown in Figure 2.5. The lasers employed were diode lasers of wavelength 660 nm and 532 nm, with their laser powers adjusted using a neutral density filter. The raster speed of patterning was set to be at 65 μm/s.

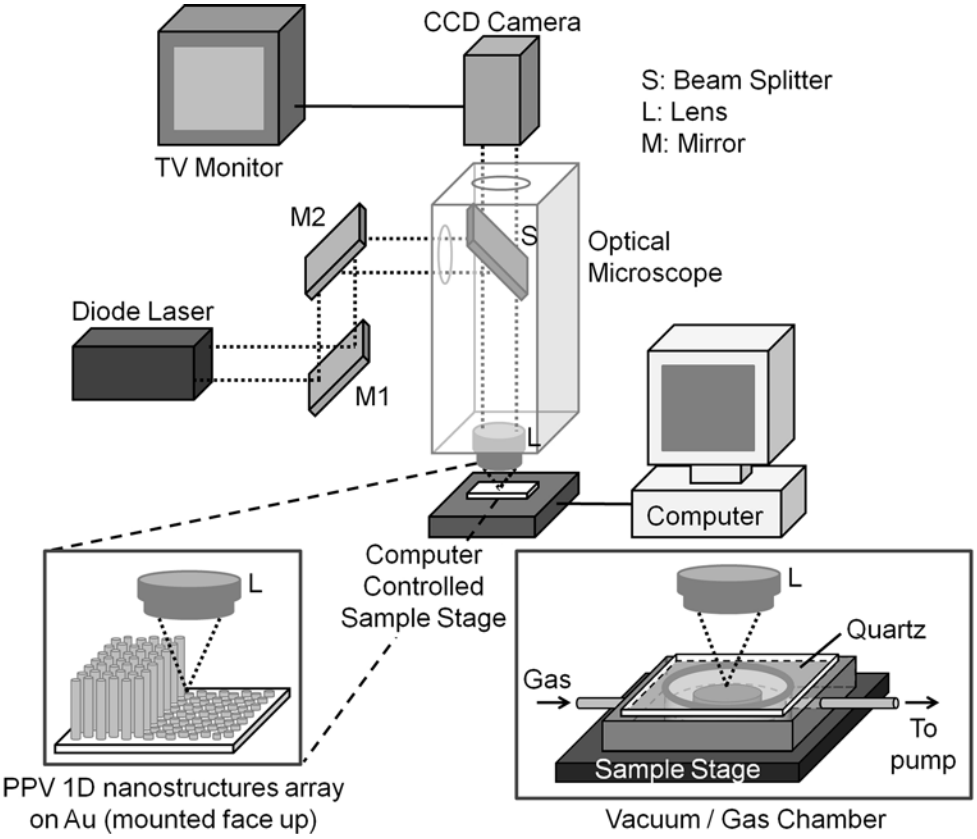

Figure 2.5: Schematic of the optical microscope-focused laser beam system used for micro-patterning. For laser pruning in air, samples were placed directly under the laser beam as shown in the bottom left box; while the box in the bottom right shows the chamber for laser pruning in vacuum or helium environment.

2.5 Oxygen reactive ion etching (O_2 RIE) and heat treatment of core-shell nanostructures

Oxygen reactive ion etching (O_2 RIE) of PPy/Ni core-shell NWs in Section 4.1.1 was carried out using SAMCO RIE-10N, operated at power of 20 W and pressure of 0.05 Torr. Samples were placed facing up in the chamber and etched for 15 minutes.

For the heat treatment of PPy/Ni core-shell NWs to obtain nickel oxide NTs in Section 4.1.1, samples were placed in the middle of a tube furnace and treatment was carried out at 400°C in ambient air for 3 hours.

2.6 Measurement of electrochemical capacitance of Co/Al layered double hydroxides hierarchical 1D nanostructures

An electrochemical half cell was assembled in a three-electrode configuration as shown in Figure 2.1 with Pt wire as the CE, Ag/AgCl (3M KCl) as the RE and the Co/Al-LDH nanostructures prepared in Section 2.2.3 as WE. Since the nanostructures are free-standing on gold substrate, binder was not required to fabricate this WE. The electrochemical behaviour was studied via cyclic voltammetry (CV) and galvanostatic charge-discharge (C-D) measurements in 30 mL of 1 M KOH aqueous solution at ambient condition using Autolab PGSTAT30 potentiostat/galvanostat. CV curves were obtained by scanning the potential between -0.1 V and 0.5 V at scan rate of 10 mV/s. On the other hand, C-D curves were recorded at 2.5 mA/cm^2, 5.1 mA/cm^2 , 10.2 mA/cm^2 and 12.7 mA/cm^2 in potential range of 0 V to 0.45 V.

2.7 Measurement of electrochemical glucose sensing of Co/Al layered double hydroxides hierarchical 1D nanostructures

The same three-electrode configuration as described in Section 2.6 and Autolab PGSTAT30 potentiostat/galvanostat were employed.

To evaluate the glucose (Glc) sensing properties of the Co/Al-LDH electrodes, CV and hydrodynamic chronoamperometric Glc step addition were carried out at ambient condition. CV curves in Figure 5.9A were recorded in potential range of -0.1 V to 0.5 V at 10 mV/s before and after addition of Glc. Amounts of Glc added were 100 μL, 200 μL and 500 μL of 0.135 M stock solution for corresponding concentrations of 0.5 mM, 1.0 mM and 2.5 mM in 27 mL of 0.1 M NaOH. On the other hand, hydrodynamic chronoamperometric Glc step addition in Figure 5.10 was carried out at constant potentials of 0.3 V and 0.4 V with constant stirring of 700 rpm. Glc was added step-wise at interval of 50 seconds in the sequence of 10 μL, 20 μL, 40 μL, 80 μL and 100 μL of 0.135 M stock solution into 27 mL of 0.1 M NaOH for respective added concentration of 0.05 mM, 0.1 mM. 0.2 mM, 0.4 mM and 0.5 mM.

Effect of concentration of NaOH (also pH of the electrolyte) on Glc sensing was studied in electrolyte concentrations of 0.005 M, 0.01 M, 0.02 M, 0.05 M and 0.1 M NaOH. For each electrolyte, pH of the solution and the current response at 0.3 V to addition of 4 mM Glc were recorded.

Selectivity of our electrodes were tested against naturally occurring interfering compounds such as uric acid (UA) and ascorbic acid (AA). The tests were carried out at 0.3 V to measure current response of 4 mM Glc in the presence of 0.33 mM of UA and 0.125 mM of AA in 0.1 M NaOH electrolyte.

2.8 Measurement of photocurrent response of aligned MWCNT/PPV core-shell nanowires

Here, the MWCNT/PPV core-shell NWs prepared from Section 2.3.2 are tested for their photocurrent (PC) response. Since the *n*-type Si substrate may give positive results for current-voltage (*I*-*V*) and PC measurements, the nanostructures were first transferred to a non-conductive substrate as illustrated in Figure 2.6.

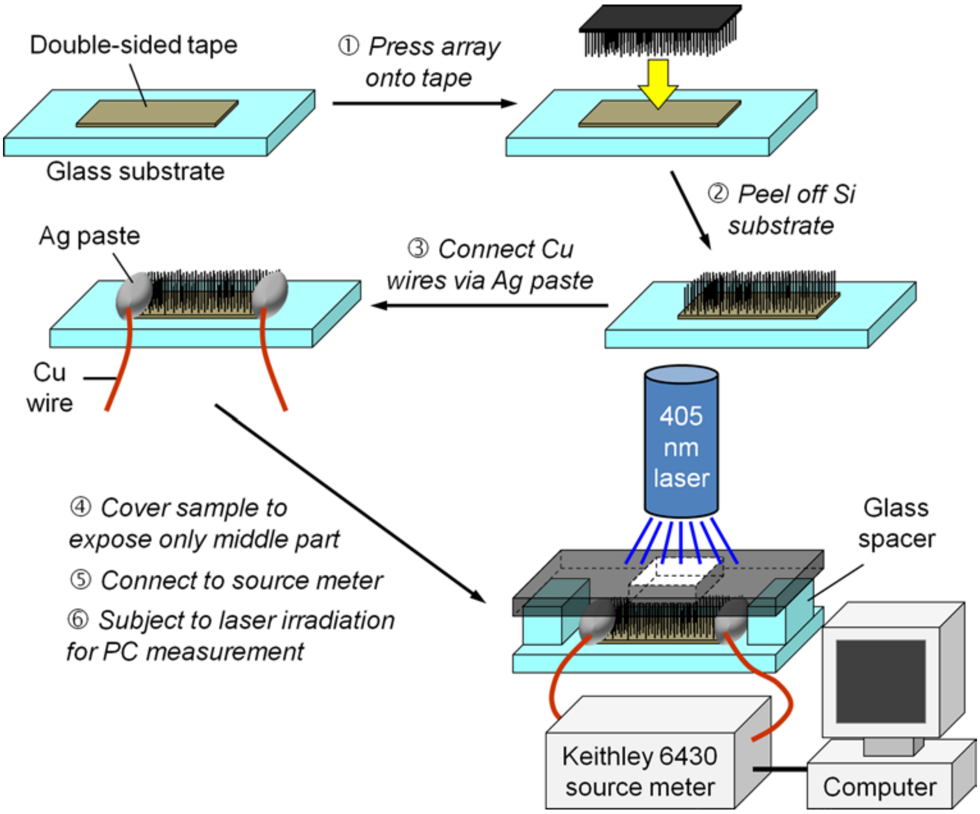

Figure 2.6: Schematic diagram for the measurement of *I*-*V* and PC response of MWCNT and MWCNT/PPV core-shell NWs.

Firstly, arrays to be studied were transferred onto double-sided tape adhered on glass substrate by pressing the array onto the tape, with the array facing down (Step 1 Figure 2.6). Then, Si substrate was slowly peeled off, leaving behind the array on the tape (Step 2 Figure 2.6). Both ends of the sample were subsequently connected to fine copper (Cu) wires using conductive silver (Ag) paste (Step 3 Figure 2.6). Once the paste dried, the sample was covered with an opaque card with a small opening of 2 mm × 2 mm, exposing only the middle part of the array to laser irradiation (Step 4 Figure 2.6). During measurements, it was ensured that the electrical connections at both ends of array were covered to prevent interference due to irradiation onto the Ag paste electrodes.

The set-up was then connected to Keithley 6430 Source Meter using metal clips for *I-V* and PC measurements (Step 5 and 6 Figure 2.6). For *I-V* measurement, the voltage was swept from -0.1 V to +0.1 V. For PC measurement, the current response was recorded over time in the absence and presence of irradiation at a constant bias voltage of 0.1 V. The presence of irradiation is denoted as the “on” state and when the beam is blocked, it is denoted as the “off” state. Blue laser (405 nm) with power of 1.5 mW/mm^2 was used as the light source.

2.9 Characterization techniques

2.9.1 Scanning Electron Microscopy (SEM)

SEM was performed in a JEOL JSM 6700-F operating at 10 μA and 5.0 kV to characterize the morphology and dimensions of the nanostructures obtained. Samples for analysis were prepared by sticking the free-standing array of nanostructures (which remained on their respective substrates) onto a metal stud (sample holder). The samples were then mounted into the SEM chamber for analysis. Samples with less conductive surfaces were sputtered with a thin layer of platinum using JEOL JFC-1600 Auto Fine Coater (operating at -20mA for 45s) before analysis.

2.9.2 Transmission Electron Microscope (TEM) and High Resolution TEM (HRTEM)

TEM was performed in a JEOL JEM 2010F with an acceleration voltage of 200 kV whereas HRTEM in a JEOL JEM 3010 with an acceleration voltage of 300kV. Sample preparation for TEM characterization varies for different type of nanostructures prepared in this thesis. For PPV samples in Chapter 3, the gold substrate was firstly removed by dipping into HNO_3:HCl = 1:3 mixture solution. The samples were rinsed with deionized water before releasing the nanostructures from AAO template using 0.5 M NaOH. The products were washed and centrifuged using distilled water until pH 7 was reached, followed by dispersion in ethanol. In Chapter 6, samples of MWCNT and MWCNT/PPV were prepared by scrapping off small bits of the nanostructures from the Si substrate and dispersed into 100μL of ethanol in microcentrifuge tube. Each solution containing the dispersed nanostructures was dripped onto a 200 mesh carbon-coated copper grid and dried in vacuum before TEM analysis.

2.9.3 Energy Dispersive X-ray Spectroscopy (EDX)

EDX analysis was carried out in a JEOL JSM 6701-F electron microscope operating at 10 μA and 15.0 kV, equipped with EDX detector. Samples for analysis were prepared by sticking the free-standing array of nanostructures (which remained on their respective substrates) onto a metal stud (sample holder). The samples were then mounted into the SEM chamber for analysis.

2.9.4 Diffuse Reflectance Fourier-Transform Infrared (DR-FTIR)

DR-FTIR spectra were obtained from Nicolet Continuμm FT-IR Microscope using reflectance mode. Samples to be analyzed would need to be on gold substrate for better signals. Since the PPV samples in Chapter 3 were free-standing on gold substrate, there was no need for further sample preparation.

2.9.5 Raman Scattering Spectroscopy

Micro-Raman spectra were obtained from Renishaw inVia Raman Microscope. For PPV samples in Chapter 3, laser excitation at 785 nm was chosen to avoid high fluorescence background interference which was observed if 532 nm was to be used as excitation source. As for Chapter 6, excitation wavelengths at 532 nm, 633 nm and 785 nm were employed and the differences in the Raman spectra are discussed in the Chapter. All Raman analyses were carried out directly on the free-standing nanostructures on substrate.

2.9.6 UV-Visible Absorption Spectroscopy

UV-visible absorption spectra were acquired from Shimadzu UV-3600, attached with integrated sphere. For the as-grown PPV samples in Chapter 3, the measurements were carried out with the nanostructures still embedded in AAO with the gold substrate removed. A baseline was obtained using pristine AAO membrane before measurement. As for the MWCNT and MWCNT/PPV core-shell NWs in Chapter 6, samples were prepared by scrapping the nanostructures from the Si substrate and blended with $BaSO_4$ using mortar and pestle. The mixture was then pressed onto sample holder. A baseline was obtained using $BaSO_4$ before measurements.

2.9.7 Photoluminescence (PL) Spectroscopy

In Chapter 3 and Chapter 6, selective-area PL spectra of the PPV NWs and NTs arrays (before and after laser patterning) and MWCNT/PPV nanostructures were obtained from Renishaw inVia Raman Microscope with laser excitation at 325 nm at room temperature. Analyses were carried out directly on the free-standing nanostructures without need of additional sample preparation.

2.9.8 Fluorescence Microscopy (FM)

In Chapter 3, the fluorescence images of the patterned PPV arrays were obtained from Nikon Eclipse T*i* Inverted Microscope. Illumination source was Mercury arc lamp and the filter used was UV-1A (excitation filter at

360-370 nm, dichromatic mirror cut-on at 380 nm, barrier filter cut-on at 420 nm).

2.9.9 X-ray Diffraction (XRD)

XRD patterns were recorded using a Philips X-ray diffractometer with Cu Kα radiation (λ = 1.54187 Å) scanning in the 2θ range of 10°-80°. The free-standing arrays of nanostructures were placed onto a glass slide and then mounted on the sample holder in the instrument for measurement.

2.9.10 X-ray Photoelectron Spectroscopy (XPS)

In Chapter 3, XPS measurements were performed on Kratos Analytical Axis Ultra DLD using monochromated Al Kα (1486.6 eV) X-ray source at emission current of 10 mA and voltage of 15 kV. To characterize the surface of PPV nanostructures before and after laser treatment, the scan spot size was fixed approximately at 220 μm, which is smaller than the region of 600 × 600 μm treated with laser.

2.10 References

1. T. H. Kim, S. M. Park. *Electrochim. Acta* **50** (2005) 1461-1467.
2. G. A. DiBari. *Plat. Surf. Finish.* **91** (2004) 23-26.
3. K. K. Lee, P. Y. Loh, C. H. Sow, W. S. Chin. *Electrochem. Commun.* **20** (2012) 128-132.
4. K. K. Lee, P. Y. Loh, C. H. Sow, W. S. Chin. *Biosens. Bioelectron.* **39** (2013) 255-260.

5. Y. H. Wang, J. Lin, C. H. Huan, G. S. Chen. *Appl. Phys. Lett.* **79** (2001) 680-682.

6. K. Y. Lim, C. H. Sow, J. Y. Lin, F. C. Cheong, Z. X. Shen, J. T. L. Thong, K. C. Chin, A. T. S. Wee. *Adv. Mater.* **15** (2003) 300-303.

Chapter 3

Fabrication and Micro-Patterning of Luminescent Poly(*p*-phenylene vinylene) Nanowire and Nanotube Arrays

Conducting polymers (CPs) have attracted much attention due to their chemically tuneable optical and electronic properties, as well as their ability for solution processing.[1, 2] These polymers have extended π-conjugation typically arises from alternating single and double C-C bonds along their polymer backbone. Some examples of conducting polymers are polyacetylene (PA), polypyrrole (PPy), polythiophene (PTh), polyaniline (PANI) and poly(*p*-phenylene vinylene) (PPV). 1D nanostructures fabricated from such polymers have been the subject of recent active research to exploit their unique physical, chemical, electronic and photonic properties.[3-6] One important aspect in the CPs NWs technologies is to develop reliable methods for the production of such nanostructures with a good control over critical parameters such as diameter, length, morphology, and chemical composition.

PPV consists of alternating benzene ring and C=C double bonds along its polymer chain. It is well-known to exhibit photoluminescence (PL),[7] electroluminescence,[8] and non-linear optical properties.[9] Despite all these potentials, fabrication of PPV in an intended shape of a desired dimension is extremely challenging due to the insolubility of PPV in any solvent and to its intractability. Therefore, one has to rely on soluble precursors that can be converted chemically or thermally to the final composition. The sulphonium precursor route first described by Wessling and Zimmerman[10] is one of the most widely used method.[8, 11, 12]

Hence, in the literature PPV NWs or NTs have been prepared from soluble precursor polymers into the desired morphology followed by thermal conversion. Some examples are chemical vapour deposition (CVD) polymerization into AAO template,[13] impregnation of precursor solution into AAO template[14] and electrospinning.[15-17] In general, these methods are tedious and/or costly as they require long hours of preparation and purification of the precursor, post-treatment of samples to convert the precursors to PPV, high temperature furnace and vacuum system. In addition, side products have to be removed during these processes, which are expected to generate many defects such as impurities and bubbles in the final product.

In this chapter, arrays of PPV 1D nanostructures were prepared by a simple electrochemical reduction of α,α,α’,α’-tetrabromo-*p*-xylene (TBX) into the nanochannels of AAO. While electrodeposition of PPV films had been reported,[18, 19] our work adapted the electrodeposition parameters together with AAO template to directly prepare free-standing arrays of PPV 1D nanostructures. We established optimal parameters for the electrodeposition into the AAO nanochannels and found that the morphology and length of the nanostructures were affected by the purity of plating solution, applied cathodic potential and amount of charge deposited.

In Section 3.2, we further demonstrated the ability to micro-pattern the PPV arrays using focused laser beam. A “red-shift” of the PL peak of PPV upon laser modification in ambient was observed. Further studies were carried out in attempt to understand the phenomenon.

3.1 PPV 1D nanostructures

Electrodeposition of PPV nanostructures was detailed in Section 2.2.1. Constant-potential coulometry was carried out to prepare PPV nanostructures inside the pores of AAO membrane. The template was then removed, giving free-standing array of PPV nanostructures on the gold substrate. The mechanism for electrochemical synthesis of PPV from TBX proposed by Kim *et al.*[18] is as shown in Figure 3.1.

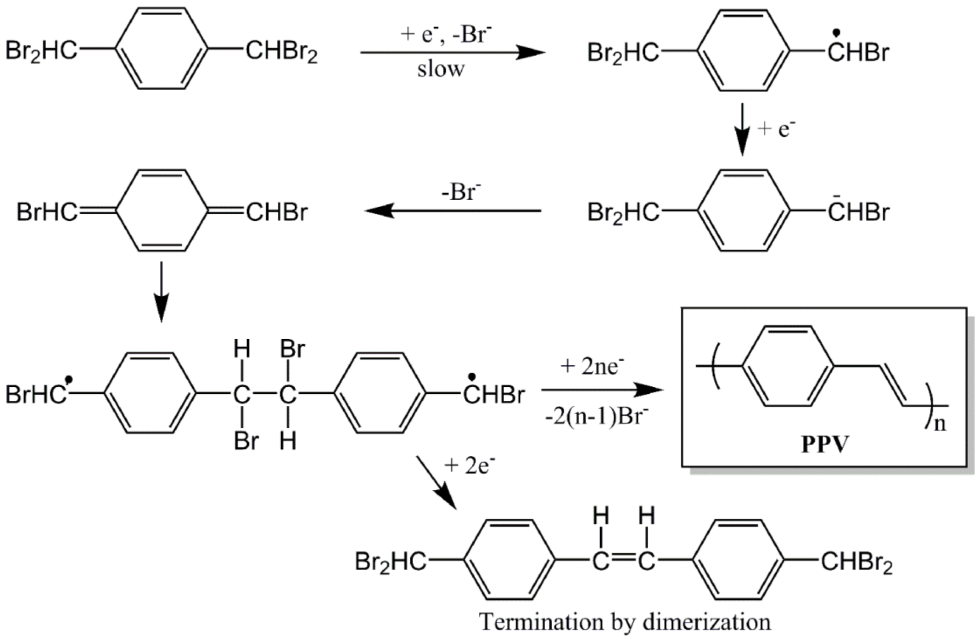

Figure 3.1: The mechanism for electrochemical polymerization of PPV from TBX as proposed by Kim *et al.*[18]

3.1.1 Effects of oxygen and moisture in the plating solution

Electropolymerization of PPV from the acetonitrile (ACN) (as-received) plating solution at constant potential of -2.34 V resulted in well-formed free-standing PPV NWs arrays as shown in Figure 3.2. As expected, the length of PPV NWs increased with an increase in charge deposited (Figure 3.2A-C). The correlation is illustrated by a plot of length versus charge deposited in Figure 3.2E. A self-limiting plateau was obtained, indicating that PPV NWs can be grown controllably up to about 1.2 μm in length with this method.

It was observed, however, that the tips of the NWs were not as well-formed when deposited with cathodic charge of 2.0 C and above (Figure 3.2D). This is probably due to bubbles that were observed on the surface of the AAO template during prolonged electrodeposition time. These bubbles were most likely hydrogen gas created from the reduction of oxygen and moisture in the plating solution. The reaction equations and their respective standard electrode potentials are summarized as follow:

$O_2\ (g) + 2H_2O\ (l) + 4e^- \rightarrow 4OH^-\ (aq)$ $E^0 = 0.4$ V (vs SHE) … (3.1)

$O_2\ (g) + 4H^+ + 4e^- \rightarrow 2H_2O\ (l)$ $E^0 = 1.23$ V (vs SHE) … (3.2)

$2H_2O\ (l) + 2e^- \rightarrow H_2\ (g) + 2OH^-\ (aq)$ $E^0 = -0.83$ V (vs SHE) … (3.3)

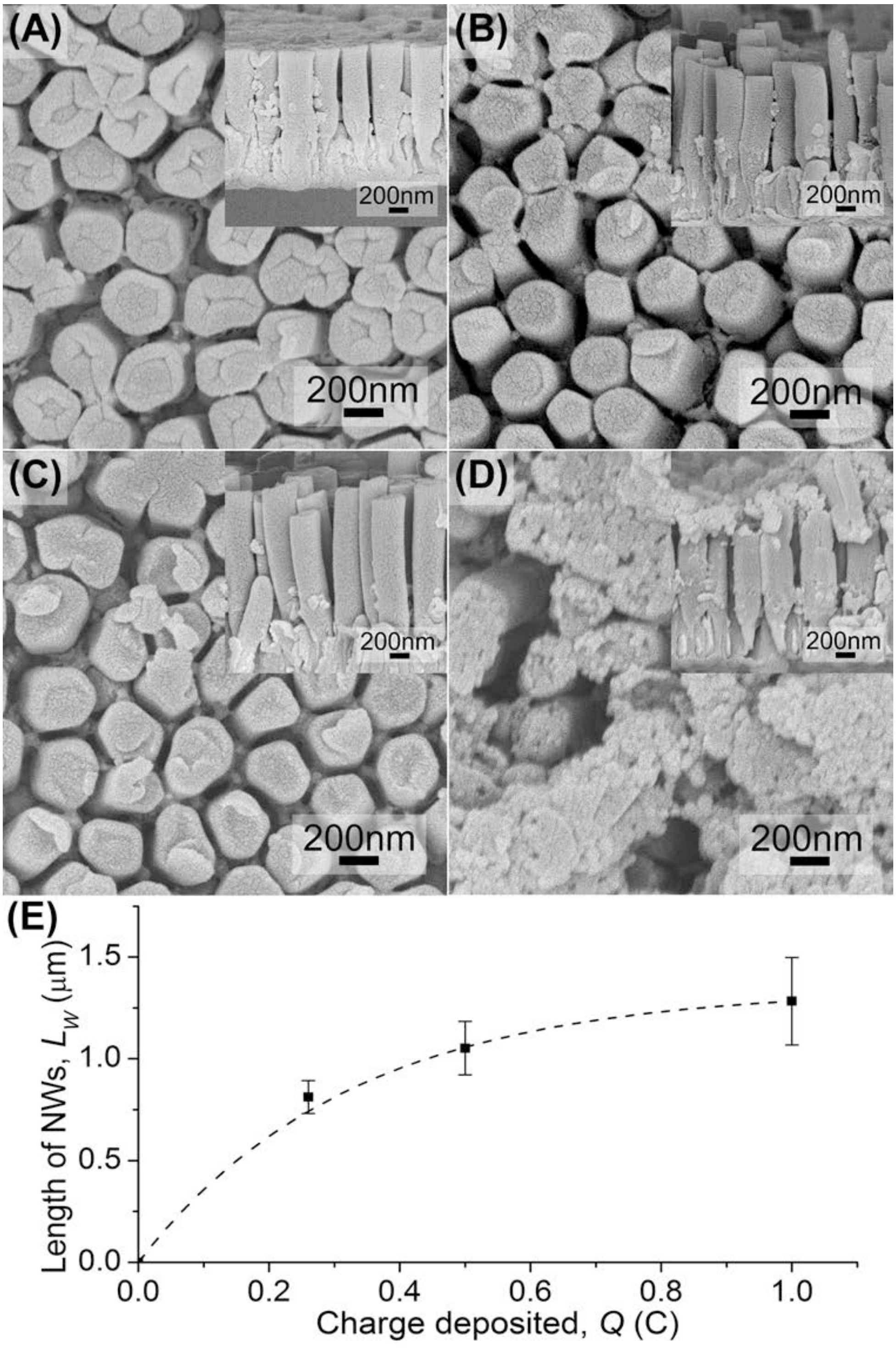

Figure 3.2: SEM images of PPV NWs electrodeposited at -2.34 V for cathodic charge of (A) 0.26 C, (B) 0.5 C, (C) 1.0 C and (D) 2.0 C. Insets show the side-view of the NWs. (E) A plot of the length of PPV NWs synthesized as a function of charge deposited. The line is drawn as a guide.

Since the deposition of larger amount of charge would necessitate longer deposition time, constant agitation from the bubbles formed would have affected further growth of PPV at the tips of the NWs during prolonged deposition. These tips could collapse after the removal of AAO template, forming ruptures or particles on top of the array. As observed in Figure 3.2D, this left behind short segments of NWs standing on the gold substrate.

On the other hand, we observed that different nanostructure morphology was obtained when the ACN solvent was distilled prior to use and the plating solution was purged with N_2 gas. For the convenience of our discussion, we refer this synthesis procedure as using “distilled ACN" solution. With the removal of moisture and oxygen from the plating solution through distillation and purging, well-formed arrays of PPV NTs were obtained using the same set-up and synthesis parameters (Figure 3.3A-D). These NTs were well-formed even when deposited at extended duration at cathodic charge of 2.0 C. However, the tubular section of the nanostructure was only found near the tips of NTs as clearly illustrated in the TEM images in Figure 3.3C-D. This NT-NW hybrid structure is quite common for conducting polymers grown by electrochemistry method using AAO as template.[20-22] The plot of length of NTs versus the amount of charge deposited in Figure 3.3E suggested a better linear correlation than that in Figure 3.2E. Thus, PPV NTs with much longer length can be prepared at the same amount of charge using distilled ACN plating solution.

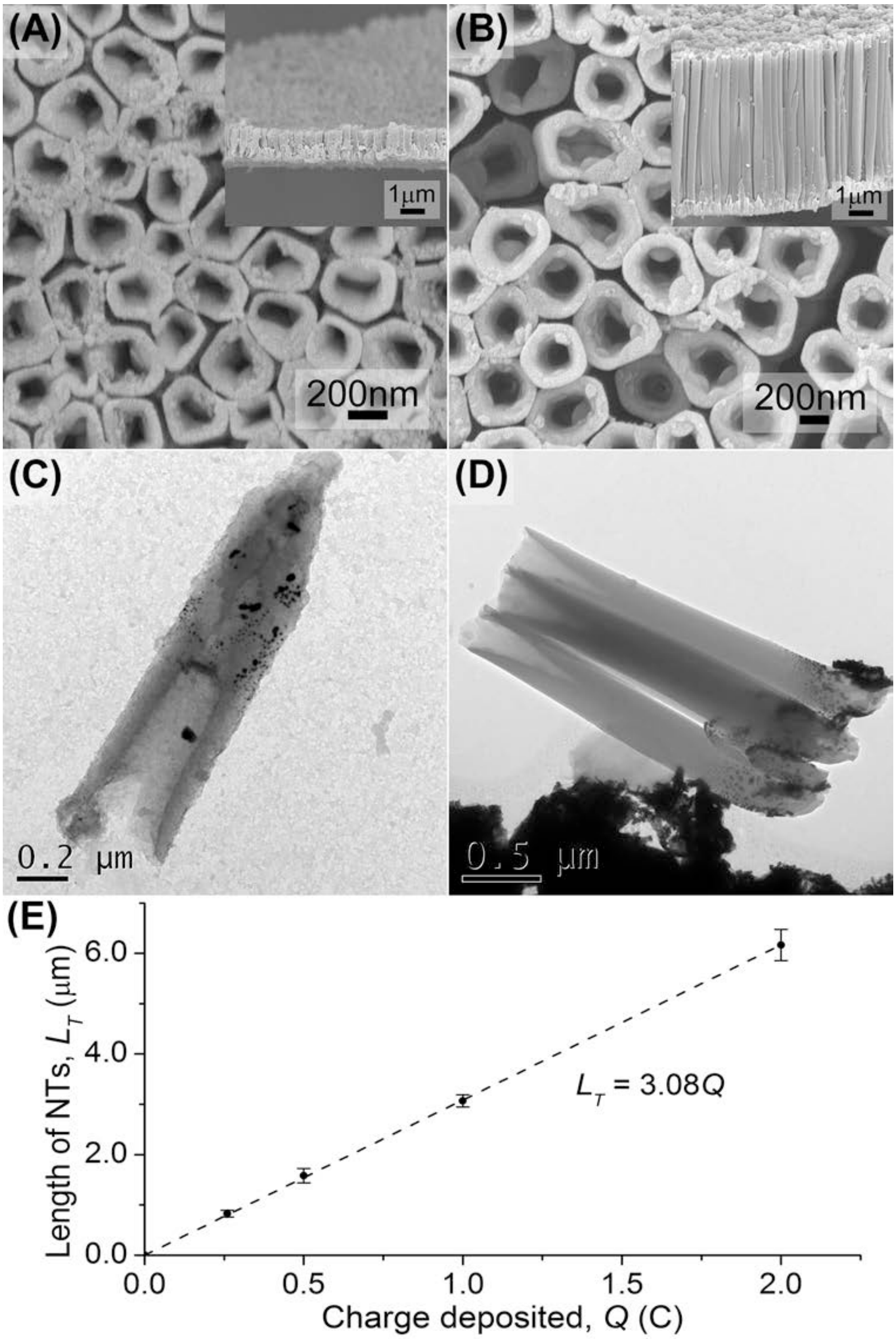

Figure 3.3: SEM images of PPV NTs electrodeposited at -2.34 V using distilled ACN plating solution for cathodic charge of (A) 0.26 C and (B) 2.0 C. The insets show side-view of the NTs. TEM images of PPV NTs prepared for cathodic charge of (C) 0.26 C and (D) 1.0 C. (E) A plot of the length of PPV NTs synthesized as a function of charge deposited.

The well-deposited PPV NTs from distilled ACN confirmed that the presence of moisture and oxygen have much effect on the electrodeposition of PPV in the AAO templates. We hypothesized that, in the presence of moisture and oxygen in the solution, bubbles evolved from the gold WE would disturb and increase the diffusion of monomers into the nanochannels. At constant deposition rate (i.e. applied potential), such increase in diffusion will lead to sufficient supply of monomers into the nanochannels and the formation of NWs. On the contrary, when both oxygen and moisture were removed, there were no bubbles evolved and diffusion would be slower, resulting to the growth of NTs at the same deposition rate. In addition, side reactions as indicated by Equations (3.1) to (3.3) would also affect the actual amount of charge contributing to the growth of PPV, i.e. shorter NWs were obtained at the same amount of charge deposited as the NTs.

3.1.2 Effects of applied potential

Next, we investigated the effect of applied potential used in electrodeposition. For electrodeposition in as-received ACN plating solution, NWs were obtained at cathodic potentials of -2.04 V and -2.34 V as shown by TEM images in Figure 3.4A and Figure 3.4B, respectively. When the cathodic potential was increased to -2.74 V, tubular section was observed at the tip of the nanostructure but was not well-formed (Figure 3.4C). On the other hand, electrodeposition in distilled ACN plating solution gave tubular NTs at -2.34 V (Figure 3.3 and Figure 3.4E), and the tubular section was found to decrease as the applied cathodic potential decreases from -2.04 V to -1.74 V (Figure 3.4D). These observations are similar to those reported for electrodeposition of CPs where an increase in deposition potential often gave more tubular nanostructures, which was explained by the diffusion mechanism.[20-23] Thus, at higher deposition potentials and the same precursor concentration, deposition rate is increased but growth is limited by diffusion of monomers, leading to the formation of NTs. Besides, it was also proposed that polymer tends to nucleate and grow from the channel walls of AAO due to attractive interaction such as solvophobic and electrostatic interactions between the reacting species and pore walls.[24, 25]

Other than morphology change, the nanostructures appeared to be longer for increasing cathodic potentials in both plating solutions. As the rate of electrodeposition increases with cathodic potential, the same amount deposited may have spread out to form tubular structures thus resulting in longer nanostructures.

To illustrate the correlation of tubular length and applied potential, a graph of relative tubular length against the applied cathodic potential was plotted in Figure 3.4F. This plot excluded the samples prepared at -2.74 V in the as-received ACN solution as they were not well-formed. There is no clear correlation obtained from these plots; nevertheless, it is evident that synthesis in distilled ACN always produces relatively longer tubular segment compared to that in the as-received ACN at the same amount of cathodic charge.

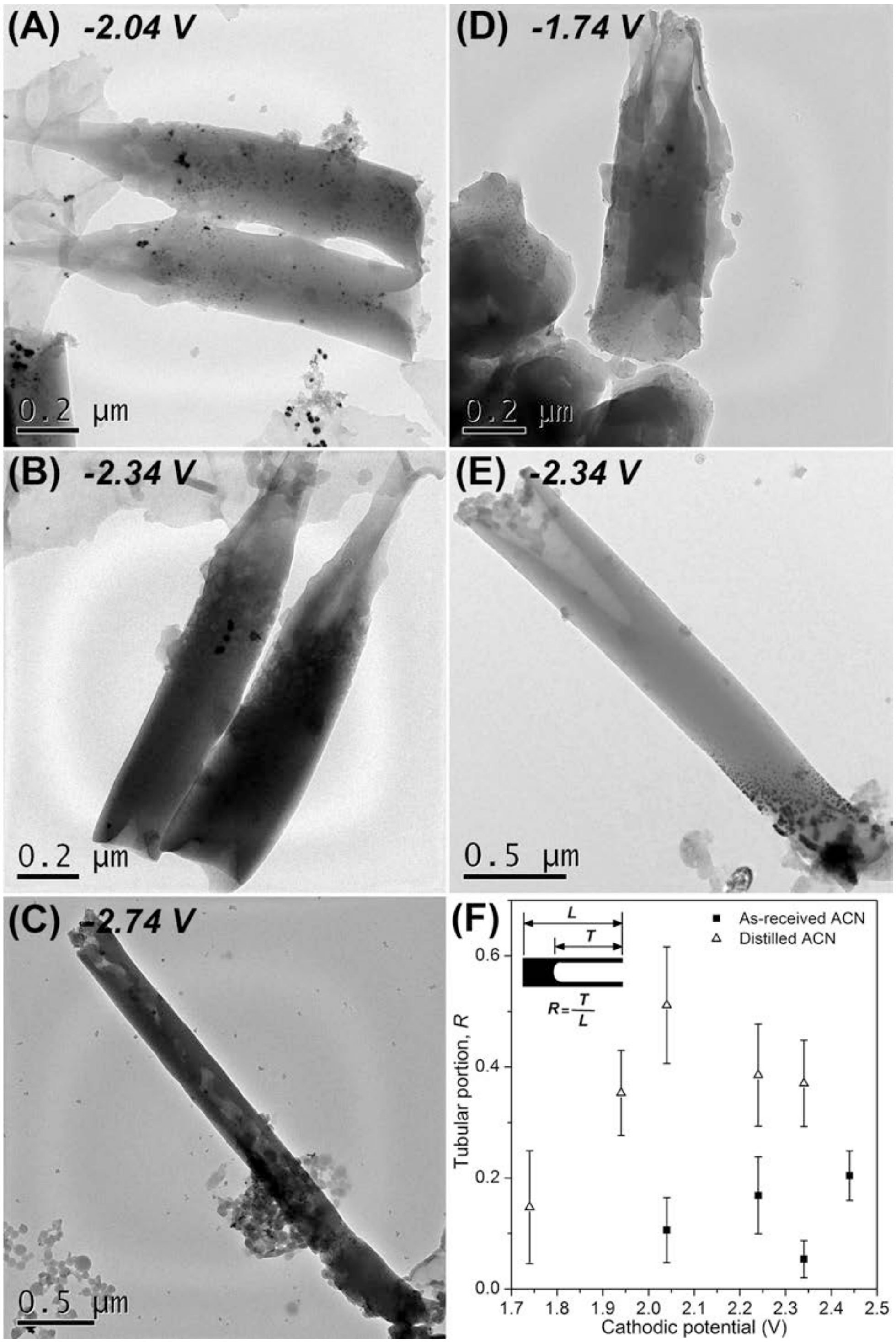

Figure 3.4: TEM images of PPV nanostructures electrodeposited from (A-C) as-received and (D-E) distilled ACN plating solutions for cathodic charge of 1.0 C at the potentials specified. (F) Plot of tubular portion versus applied cathodic potential.

In the following discussion, we have chosen to prepare PPV nanostructures at an optimal cathodic potential of -2.34 V for cathodic charge of 0.26 C. For convenience, we will label the samples obtained from the as-received ACN solution as PPV NWs while those from distilled ACN solution as PPV NTs.

3.1.3 Characterization of PPV nanostructures

The PPV nanostructures were characterized using DR-FTIR (Section 2.8.4) and micro-Raman (Section 2.8.5) to validate the successful electropolymerization of PPV. Typical IR and Raman spectra obtained are shown in Figure 3.5A and Figure 3.5B, respectively. Overall, the peak assignments (as tabulated in Table 3.1) are in good agreement with those reported for chemically-synthesized PPV films.[26] However, these PPV NWs and NTs may have some extent of oxidation along the polymer chain as shown by the presence of 1695 cm^{-1} peak in the IR spectra (Figure 3.5A), which could be assigned to the carbonyl C=O stretching mode. Thus, oxidation may have occurred during the synthesis. In the Raman spectra in Figure 3.5B, the presence of a weak 963 cm^{-1} band may reflect slight distortion of vinylene group from its planar trans form.[27] From studies of a series of oligophenylene vinylenes (OPVs),[28-31] it was reported that the relative ratio of peak intensities of 1552 cm^{-1} (mainly ring stretching) to 1628 cm^{-1} (mainly vinyl C=C stretch) increases with increasing number of repeating monomer units, and is up to 1 for the polymeric PPV. In our case, the relative ratios obtained were found to be about 0.49 and 0.50 respectively for PPV NWs and NTs, suggesting shorter conjugation lengths.

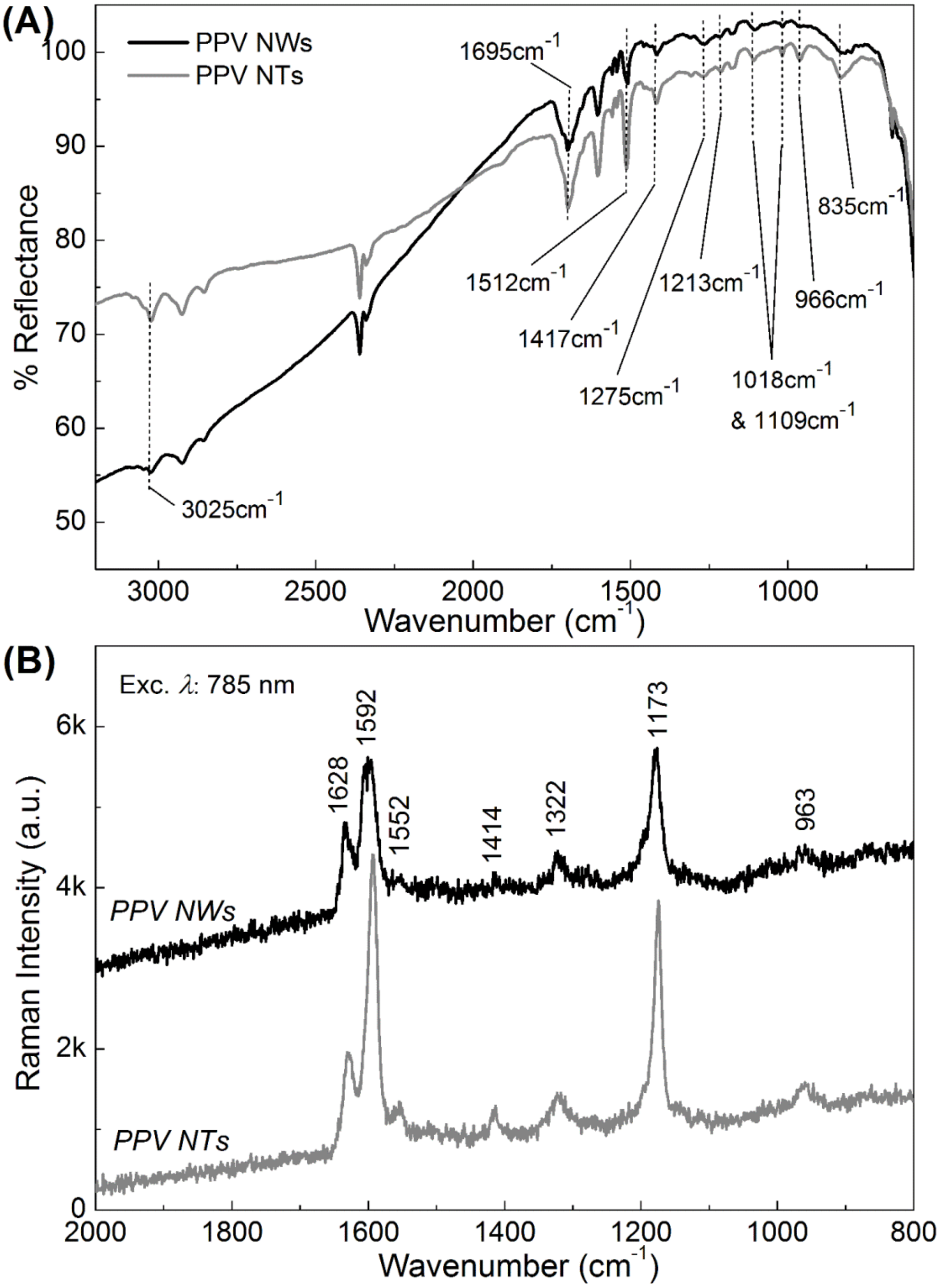

Figure 3.5: Representative (A) DR-FTIR and (B) Raman spectra of PPV NWs and NTs, with the characteristic FTIR and Raman peaks of PPV as labelled.[26] Detailed assignment is given in Table 3.1. Raman spectra were displaced for ease of comparison.

Table 3.1: Assignments of the observed vibrational bands of PPV.[26]

FTIR		Raman	
ν (cm^{-1})	**Mode**	**ν (cm^{-1})**	**Mode**
835	C-H out-of-plane bend for *p*-disubstituted benzene ring	963	C-H out-of-plane bend
966	C-H out-of-plane bend of trans-vinylene	1173	C-H in-plane bend
1018	CH in-plane bend	1322	Vinyl CH in-plane bend
1109	CH in-plane bend	1414	Ring stretch & in-plane deformation
1213	Vinyl CH in-plane bend	1552	Ring stretch
1275	Ring stretch	1592	Ring stretch, Vinyl C=C stretch
1417	Ring stretch and in-plane deformation	1628	Vinyl C=C stretch, ring stretch
1512	Ring stretch and in-plane deformation		
3025	Vinyl CH stretch		

Normalized UV-visible absorption and PL spectra of PPV NWs and NTs are shown in Figure 3.6. Samples preparations for both characterization methods were detailed in Section 2.8.6 and Section 2.8.7, respectively. For PPV NWs, it was observed that the absorption edge onset is at 442 nm and the absorption maximum appears near 337 nm. For PPV NTs, the onset is at 467 nm and a peak near 345 nm. The NWs exhibited absorption onset and peak at shorter wavelength than the NTs, although both of these values are at shorter wavelength compared to those reported.[7, 32] Studies of a series of OPVs had observed red-shift of absorption wavelengths with increasing number of repeating monomer units.[28-31] Various theoretical calculation methods were also applied and all demonstrated that the π-π* gap decreases with increase conjugation length. This suggests that the PPV obtained from our synthesis has relatively shorter conjugated chain lengths, which matches the observation derived from IR and Raman studies above. The relatively more blue-shifted absorption for the NWs may also indicate the formation of shorter conjugation chain length due to faster rate of electrodeposition as compared to the NTs.

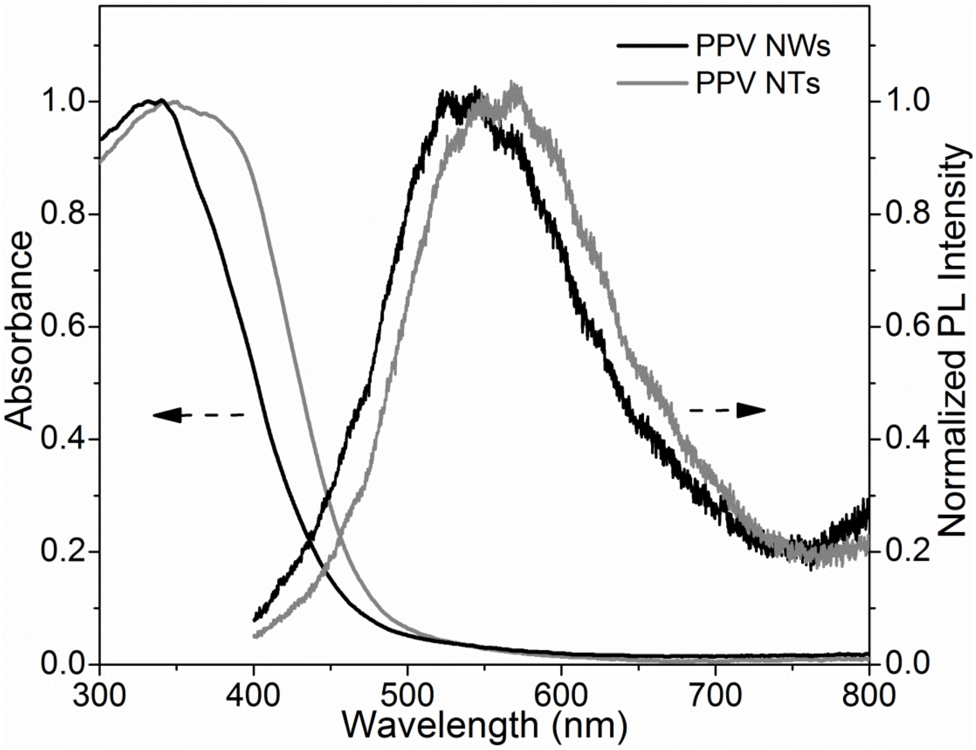

Figure 3.6: UV-visible absorption and PL spectra of PPV NWs and PPV NTs arrays. (Excitation wavelength for PL: 325 nm)

For the PL spectra in Figure 3.6, both the NWs and NTs showed a broad peak with maximum at 533 nm and 558 nm, respectively, at excitation wavelength of 325 nm. A stokes shift between the absorption and PL maxima indicates that there were relaxations of the excited state before emission. This broad PL profile is similar to that observed for PPV film prepared via electrochemical method,[32] which is rather lack of resolved vibronic progressions as compared to chemically prepared PPV.[7, 14, 16]

3.2 Micro-patterning of PPV nanostructures array via laser pruning technique

3.2.1 Laser pruning of PPV nanostructure arrays

The well-formed PPV nanostructures arrays were then subjected to micro-patterning using laser pruning technique[33] as described in Section 2.4. As an initial attempt, a diode laser of wavelength 660 nm (red laser) was employed and laser power was varied from 20 mW to 40 mW. It was found that the focused laser beam at power at or above 20mW readily cuts away the directly exposed PPV NWs and NTs. The patterns obtained and the areas cut with laser power of 40 mW were imaged using SEM as shown in Figure 3.7. Based on the tilted views at the bottom panels of each figure in Figure 3.7, the high laser power had trimmed away almost all of the PPV NWs and NTs arrays in the exposed areas. The high-power laser has transferred large amount of energy to the nanostructures, which could then burn/cut away the organic nanostructures that were exposed to the focused laser beam.

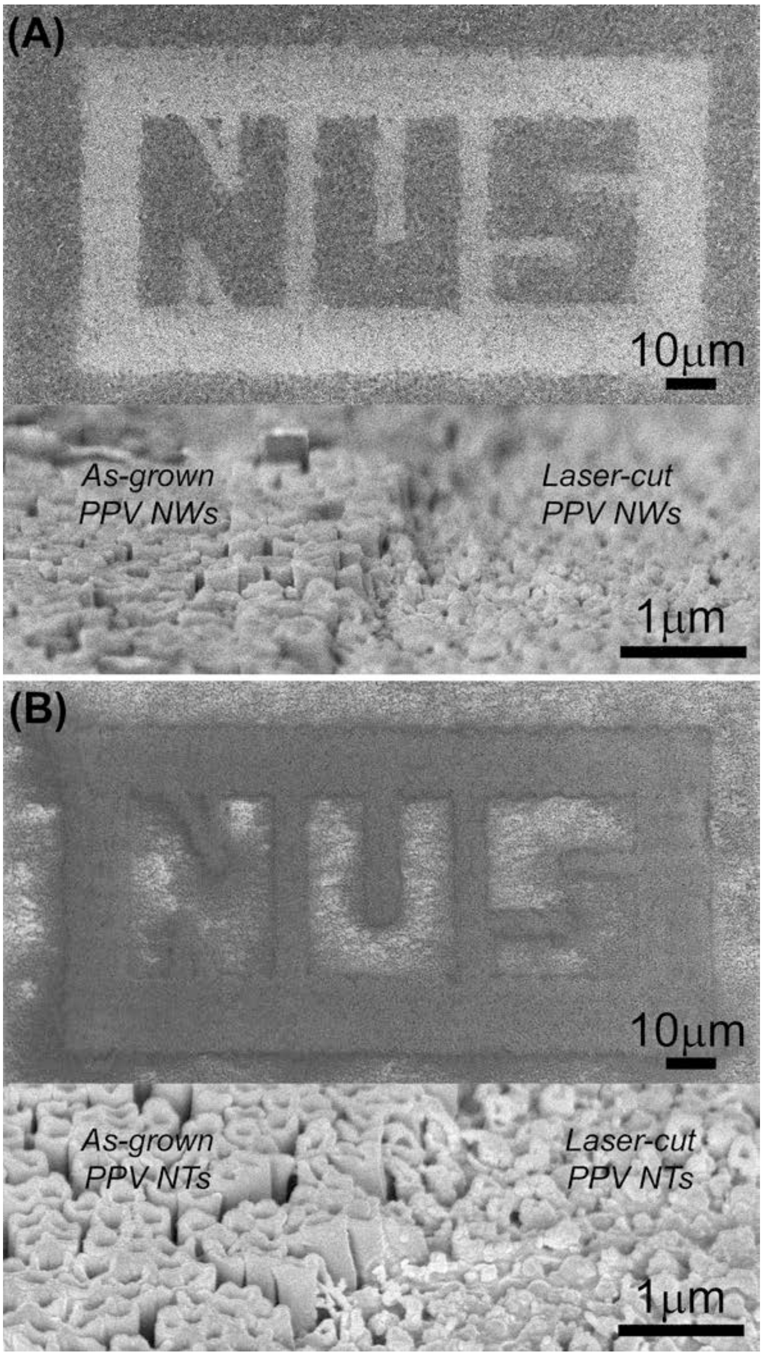

Figure 3.7: SEM images of patterns and areas cut using 40mW focused red laser for (A) PPV NWs array and (B) PPV NTs array. Top panels show top views of the laser-pruned patterns. The alphabets "NUS" are the uncut arrays while the surrounding square areas were cut away. Bottom panels show tilted views of the nanostructures areas after laser pruning.

3.2.2 Optical properties of laser-modified PPV arrays

These regions treated by laser were readily identified under the optical microscope, hence micro-PL spectra (excitation wavelength = 325 nm) from these regions could be captured. The PL spectra for areas cut by various laser powers as well as those of the as-grown PPV NWs and NTs were compared. It should be noted that the overall PL intensities for areas modified by laser are much lower than that of the as-grown PPV nanostructures. This is expected since PL signal arise from the emitting polymer nanostructures and there is less remained after the laser pruning. Thus, these PL spectra, as presented in Figure 3.8, were normalized for better comparison. From here, we observed interestingly that laser pruning gave rise to an apparent “red-shifting” of the PL maxima, which appears to be increasing with increasing laser power used. At higher laser power, we had only expected larger amounts of PPV would be removed. However, such red-shift is relatively less obvious for the controlled samples cut under inert atmosphere, i.e. vacuum (2 mTorr) and helium (200 mTorr) environment (Figure 3.8).

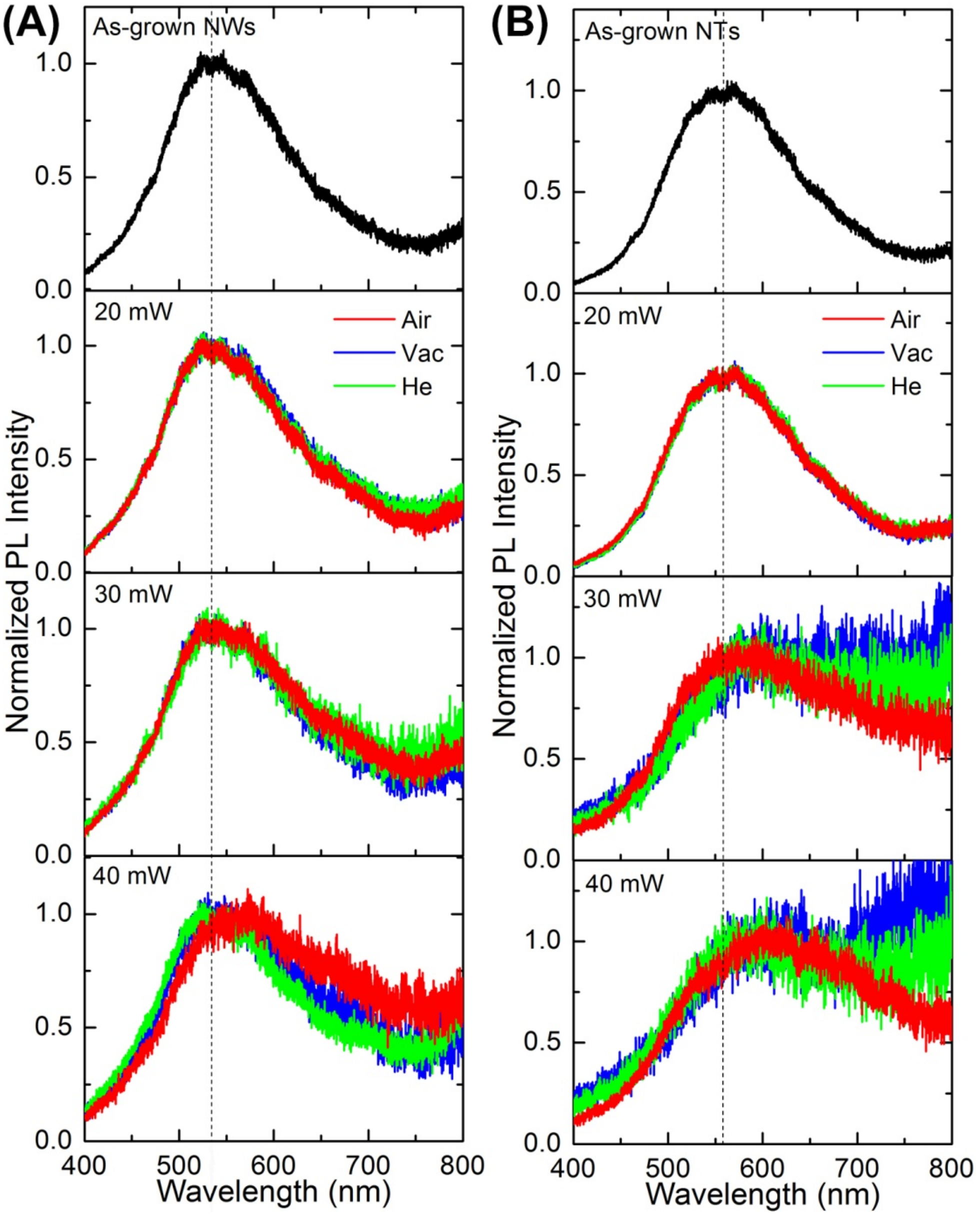

Figure 3.8: PL spectra of (A) PPV NWs and (B) PPV NTs arrays, as-grown and laser-modified (at power 20, 30 and 40 mW) in air, vacuum and helium by focused red laser. (Excitation wavelength: 325 nm)

This apparent “red-shifting” of the PL maximum is also displayed by a change of emission colour observed under fluorescence microscope (Section 2.8.8). The representative images are shown in Figure 3.9A and Figure 3.9B for PPV NWs and NTs, respectively. The greenish blue regions are the as-grown PPV nanostructures, while the darken regions are the cut areas. Note that the region modified by 40 mW laser in air appears now in orange-brownish colour. Areas modified in vacuum and helium environment are dark, nevertheless, due to diminished emission intensity.

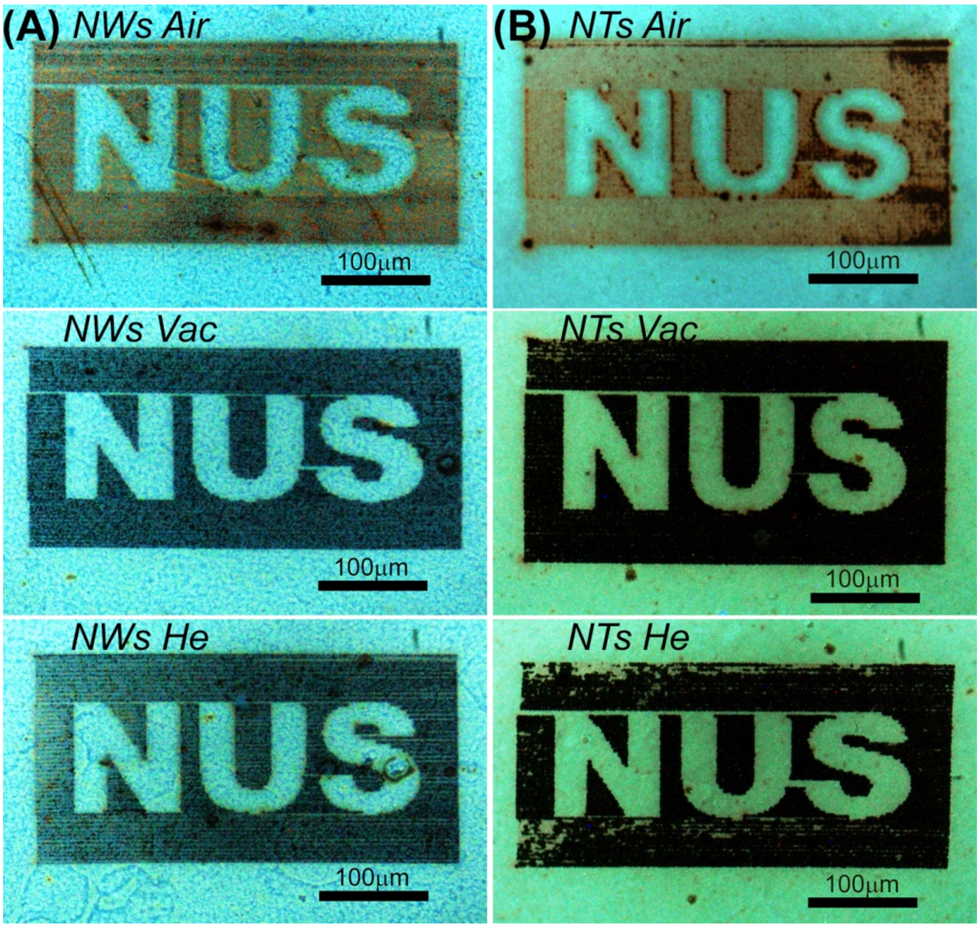

Figure 3.9: Fluorescence microscopic images of patterns cut on (A) PPV NWs array and (B) PPV NTs arrays using 40 mW red laser (660 nm) in air, vacuum and helium environment.

3.2.3 Effect of focused laser beam on PPV NTs arrays

Since the red-shift of PL maxima was more significant in samples modified in the air, it was suspected that the phenomenon could be related to the oxidation of PPV. This led us to investigate changes in the chemical structures of PPV upon laser pruning in air and in inert environment. Given that the chemical structure is the same for both PPV NW and NT nanostructures and similar effects have been observed in both vacuum and helium environment, we will focus the following discussions on NTs sample and laser pruning only in air and in vacuum.

To characterize changes of functional groups on the PPV, DR-FTIR and Raman spectra were obtained before and after the modification in air and vacuum. From the DR-FTIR spectra as shown in Figure 3.10A, it was observed that peak area at 1275 cm^{-1} and 1695 cm^{-1} increased significantly while the 966 cm^{-1} peak diminished with increasing laser power for samples modified in air. These peaks (as indicated by the arrows in the figure) correspond to the C-O stretching for carboxyl group, C=O stretching for carbonyl group and C-H out-of-plane bending of trans-vinylene mode, respectively.[34] For samples modified in the vacuum, the increase of 1695 cm^{-1} peak seems to be less than that treated in air. These observations point towards focused laser-induced oxidation of PPV upon laser pruning, to larger extent in the air.[34]

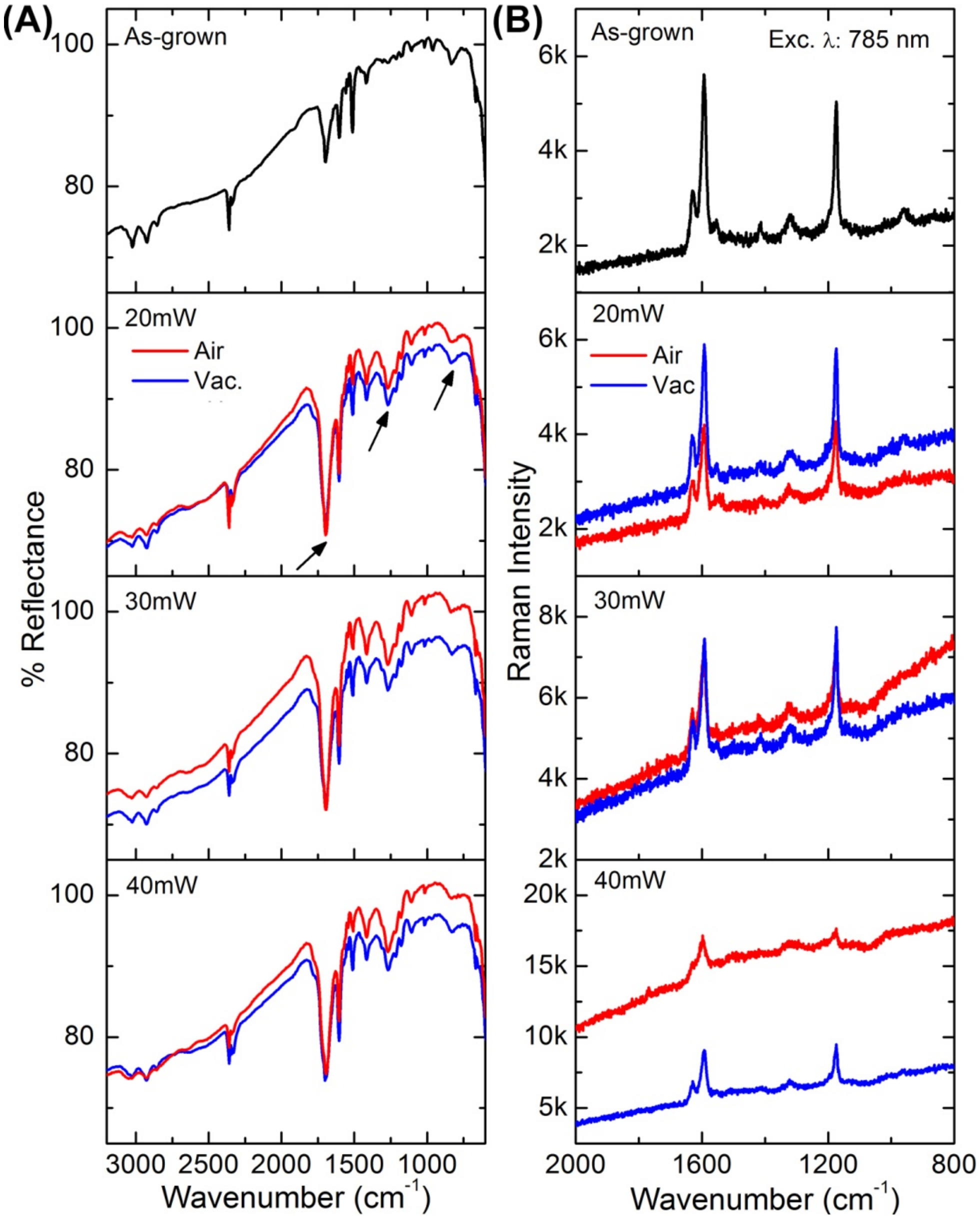

Figure 3.10: (A) DR-FTIR and (B) Raman spectra of PPV NTs, as-grown and laser-modified in air and vacuum by focused red laser.

A comparison of Raman spectra shown in Figure 3.10B indicated no new peaks for samples modified with laser either in air or in vacuum. Generally, the peak intensities decreased with increasing laser power. But, as laser power increases, there is also an increase in the background of the spectra, at a larger extent for samples modified in air. This is especially obvious for laser pruning in air at 40 mW where the baseline already starts at a rather high Raman intensity. This may be due to high fluorescence background interference[27] and corresponds to the red-shifting of PL maximum upon laser pruning in air as shown in Figure 3.8B.

In order to compare the elemental composition of PPV array before and after laser modification, XPS spectra were obtained for Br 3d, C 1s and O 1s peaks as shown in Figure 3.11. Details of the measurement were shown in Section 2.8.10. For ease of comparison, the integral intensities are calibrated to unity and offset for display. As-grown PPV NTs was found to contain minute amount of Br with a peak at 71.2 eV as shown in Figure 3.11A. The amount of Br is about 2 % of the total content as estimated from peak area. Referring to the synthesis mechanism in Figure 3.1, Br may present as end groups in probable termination by dimerization. The presence of Br may also arise from minor incomplete electropolymerization. However, upon laser pruning, no Br 3d peak was observed, indicating the laser beam had removed this impurity from the surface.

For the C 1s and O 1s core levels, their XPS spectra are as shown in Figure 3.11B and Figure 3.11C. It was noted that the C 1s peaks for samples modified in vacuum have similar peak profile as that for the untreated PPV array. For samples modified in air at high laser power, nevertheless, the C 1s peak broadened and the intensity decreased. O 1s peak for samples modified in air also broadened but the intensity increased compared to the as-grown PPV NTs. The increased amount of oxygen agrees with the increase of C=O stretching IR mode as shown in Figure 3.10A, indicating larger extent of oxidation upon laser modification in air.

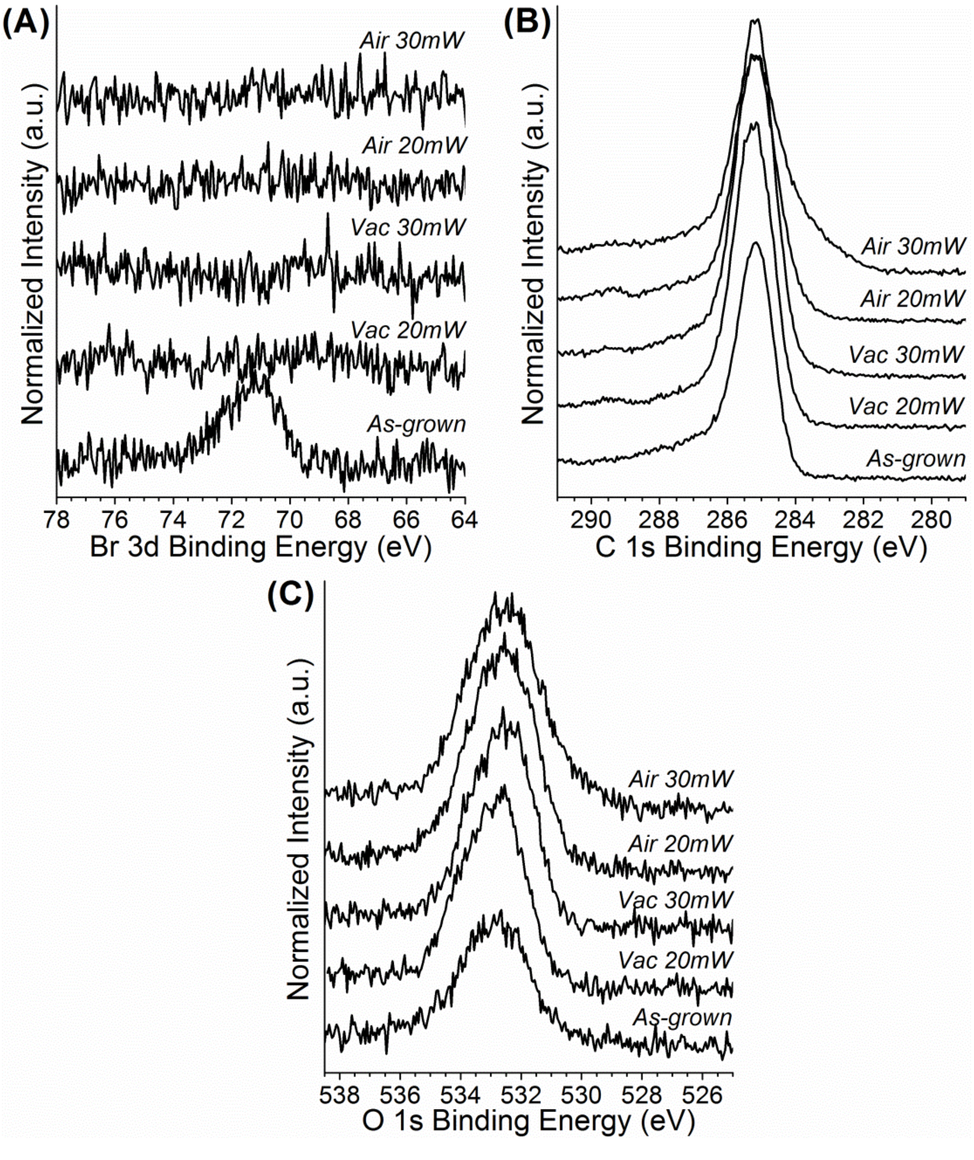

Figure 3.11: XPS spectra for (A) Br 3d, (B) C 1s and (C) O 1s binding energy for PPV NTs, as-grown and after laser pruning in air and vacuum using focused red laser. All spectra are normalized with their integral intensities calibrated to unity and offset for ease of comparison.

To evaluate the change in the chemical states, the C 1s and O 1s peaks for both as-grown and laser-modified (in air at 30mW) PPV samples, were fitted as shown in Figure 3.12. For the as-grown sample, three components were fitted for the C 1s spectrum (Figure 3.12A). The maximum component at 285.2 eV is due to the aromatic carbons in PPV structure, 286.9 eV is for C-O carbon and 288.1 eV is for C=O carbon.[35, 36] On the contrary, the C 1s spectrum of the laser-modified PPV has four components fitted (Figure 3.12C). The additional peak of ~18.5 % of fitted area appears at lower binding energy of 283.8 eV, and is commonly assigned to graphitic C. In addition, the total normalized peak area for oxygen-attached carbons were increased, from 44.4 to 51.0 upon laser modification in air (Table 3.2).

In agreement with the DR-FTIR results, O 1s peak is detected for the untreated sample indicating slight oxidation of the polymer chain after synthesis. As shown in Figure 3.12B, this peak can be fitted to two components at 533.5 eV and 532.4 eV. The same two components are found in the corresponding O 1s spectrum of the laser-modified PPV except with an overall increase in intensity (Figure 3.12D). Total peak area was increased from 26.1 to 48.2 (Table 3.2). Thus, we conclude that laser pruning in air had resulted in the oxidation and graphitization of PPV.

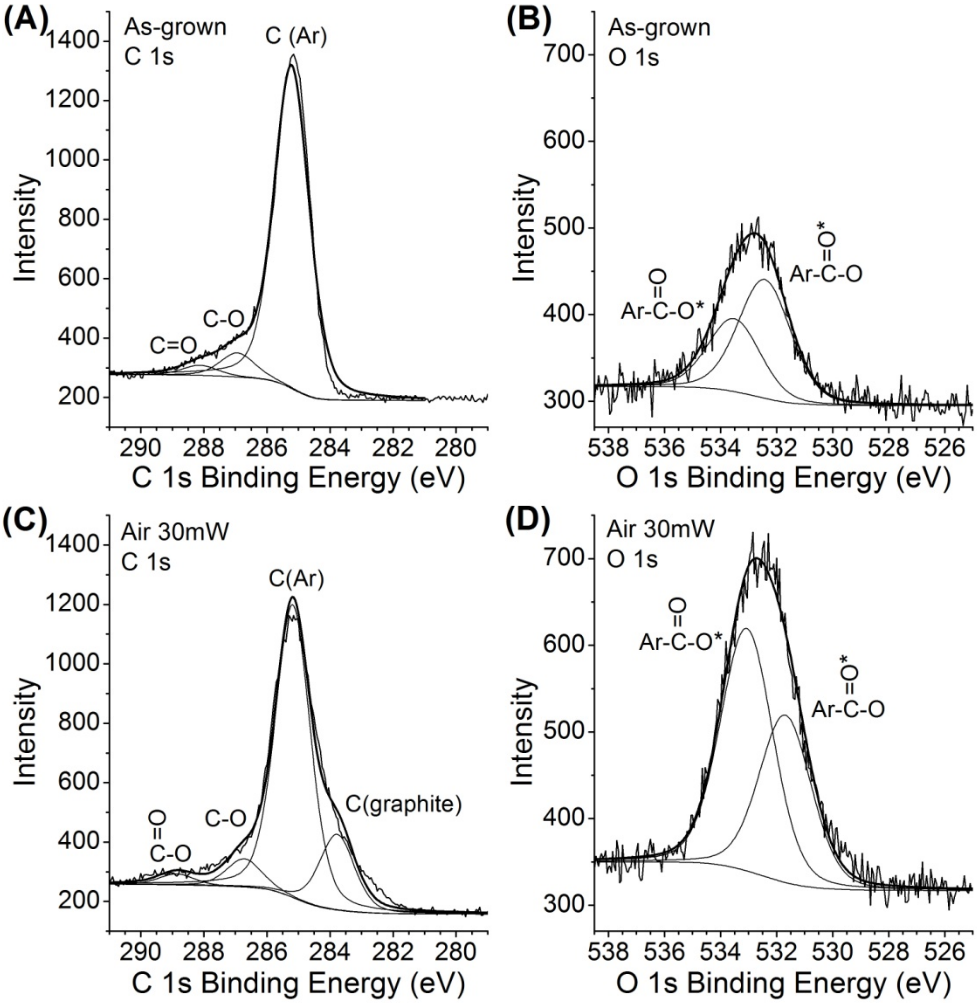

Figure 3.12: XPS spectra for C 1s and O 1s of PPV NTs: (A), (B) as-grown, (C), (D) modified in air using 30 mW focused red laser.

Table 3.2: Peak areas for all fitted components of C 1s and O 1s XPS spectra as shown in Figure 3.12. Data were normalized by respective atomic sensitivity factor (ASF) and number of scans.

Component	Normalized peak area	
	As-grown PPV	**Laser-modified PPV**
C (graphite)	-	98.4
C (Ar)	418.9	380.4
C (C-O)	31.2	36.6
C (C=O)	13.2	14.4
O (C=O)	21.2	19.7
O (C-O)	4.9	28.5

In order to further study the effect of laser treatment, we computed the ratios of FTIR peak area at 1695 cm^{-1} (C=O stretching) to 1512 cm^{-1} (ring stretching and in-plane deformation), and also the ratio of XPS O 1s peak area to C 1s peak. We plotted these ratios as well as the PL peak maximum as a function of laser power as shown in Figure 3.13. It is apparent that both the FTIR peak area ratio and the computed XPS elemental ratio increase steadily with laser power. In both cases, the increase is most obvious for laser power at 20 mW, and samples cut in air always showed higher ratios as compared to those cut in vacuum. Comparing with the PL shift, we noted that there was no obvious red-shift for samples cut at 20 mW in both air and vacuum, although the general increasing trend is similar at higher laser power.

The above results from DR-FTIR and XPS confirmed that PPV had undergone oxidation upon laser pruning in air. Oxidation could be induced by the high local temperature generated by the focused laser beam, particularly in the presence of surrounding oxygen. It was known that oxidation of PPV (either thermally or photo-induced) commonly occur at the vinylene groups; free radicals are generated and carboxyl functional groups are formed, resulting in the scissions of polymer chains.[37] In studies that had employed broad band light with wavelengths > 300 nm and unfocused lasers (456 nm and 514 nm) as global irradiation source, a blue-shift in the UV-visible absorption peak was observed and attributed to shortening of polymer chains due to oxidation.[34, 37, 38] It was also mentioned that the PL spectral position remained unchanged due to diffusion of exciton to non-degraded layer of polymer film. To the best of our knowledge, there has been no report on red-shifting of PL peak of PPV upon laser irradiation in air.

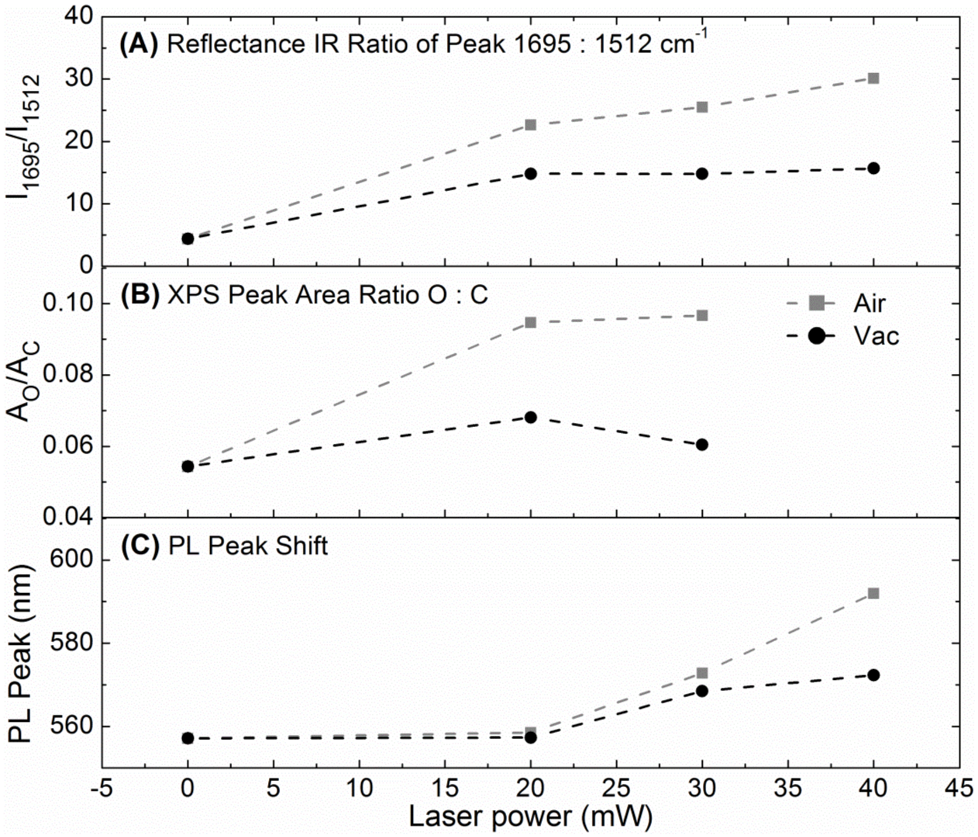

Figure 3.13: Effect of laser power used for patterning on the (A) FTIR peak area ratio of 1695 cm^{-1} to 1512 cm^{-1}, (B) XPS peak area ratio of O 1s to C 1s peaks and (C) PL maxima of PPV NTs, for samples treated in air and in vacuum. Excitation wavelength for PL: 325 nm.

To compare photo-induced oxidation of our PPV NTs to that reported of PPV films, blue laser (405 nm, unfocused) was globally irradiated on the PPV NTs array for 26 minutes and the samples were analyzed. Similar to those reported,[34, 37, 38] UV-visible absorption spectra were blue-shifted upon irradiation in air and in vacuum (Figure 3.14A). DR-FTIR spectra also confirmed an increase of peak area at 1275 cm^{-1} and 1695 cm^{-1} (as indicated by the arrows in the figure), demonstrating the occurrence of oxidation (Figure 3.14B). However, contrary to the literatures, Figure 3.14C showed that the PL peak of our PPV nanostructures red-shifted upon irradiation in air by the blue laser, although it remained the same for that treated in vacuum. This clearly indicated that the observed red-shifting of PL peak is caused by reasons more than oxidation.

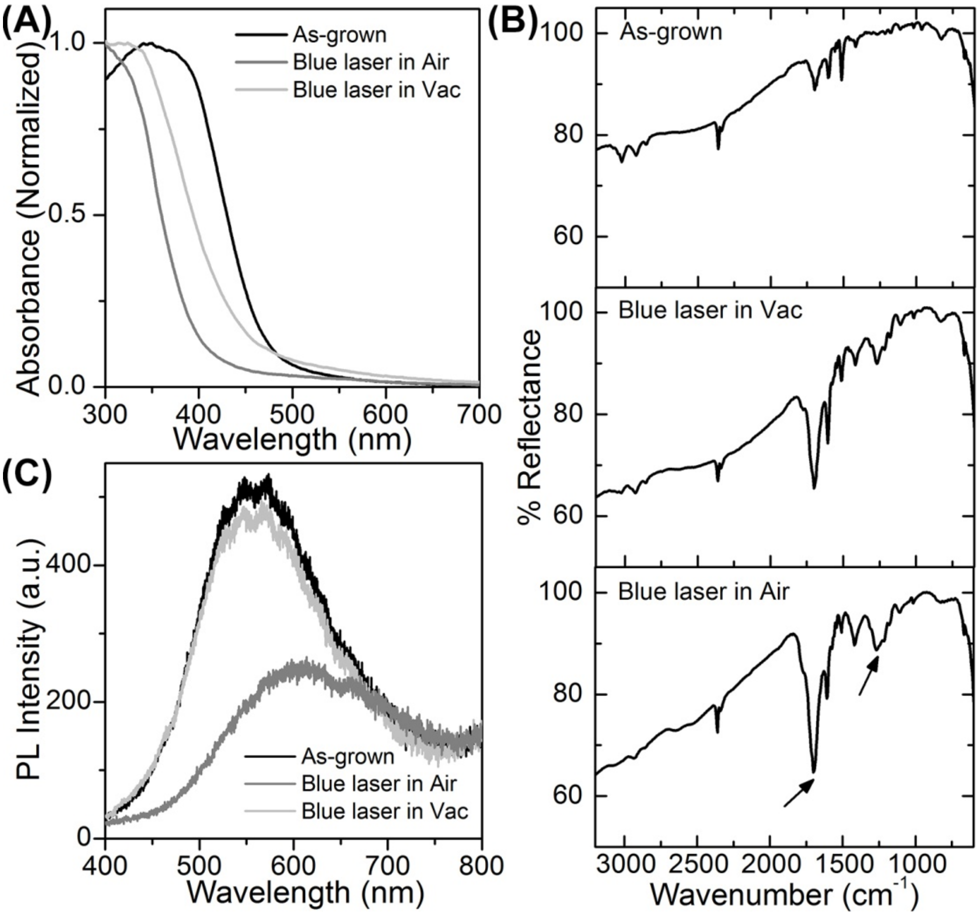

Figure 3.14: (A) UV-visible absorption spectra, (B) DR-FTIR spectra and (C) PL spectra of PPV NTs array before and after global blue laser (405 nm, unfocused) irradiation in air and vacuum. Excitation wavelength for PL: 325 nm.

We further investigated the effect using focused green laser at 532 nm. As shown in Figure 3.15A, the PL peak red-shifted by about 21 nm for PPV modified in air at 10 mW, as compared to the as-grown PPV. For samples modified in vacuum, the PL peaks remained similar at lower laser power (5 mW) but the intensity diminished completely after 10 mW. It seems that laser pruning in the vacuum using green laser at high power could remove the NTs completely. Similarly, oxidation of PPV was deduced from the DR-FTIR spectra in Figure 3.15B. The IR peak area at 1275 cm^{-1} and 1695 cm^{-1} (as indicated by the arrows in the figure) increased significantly upon laser modification at 5 mW in air, compared to that in vacuum.

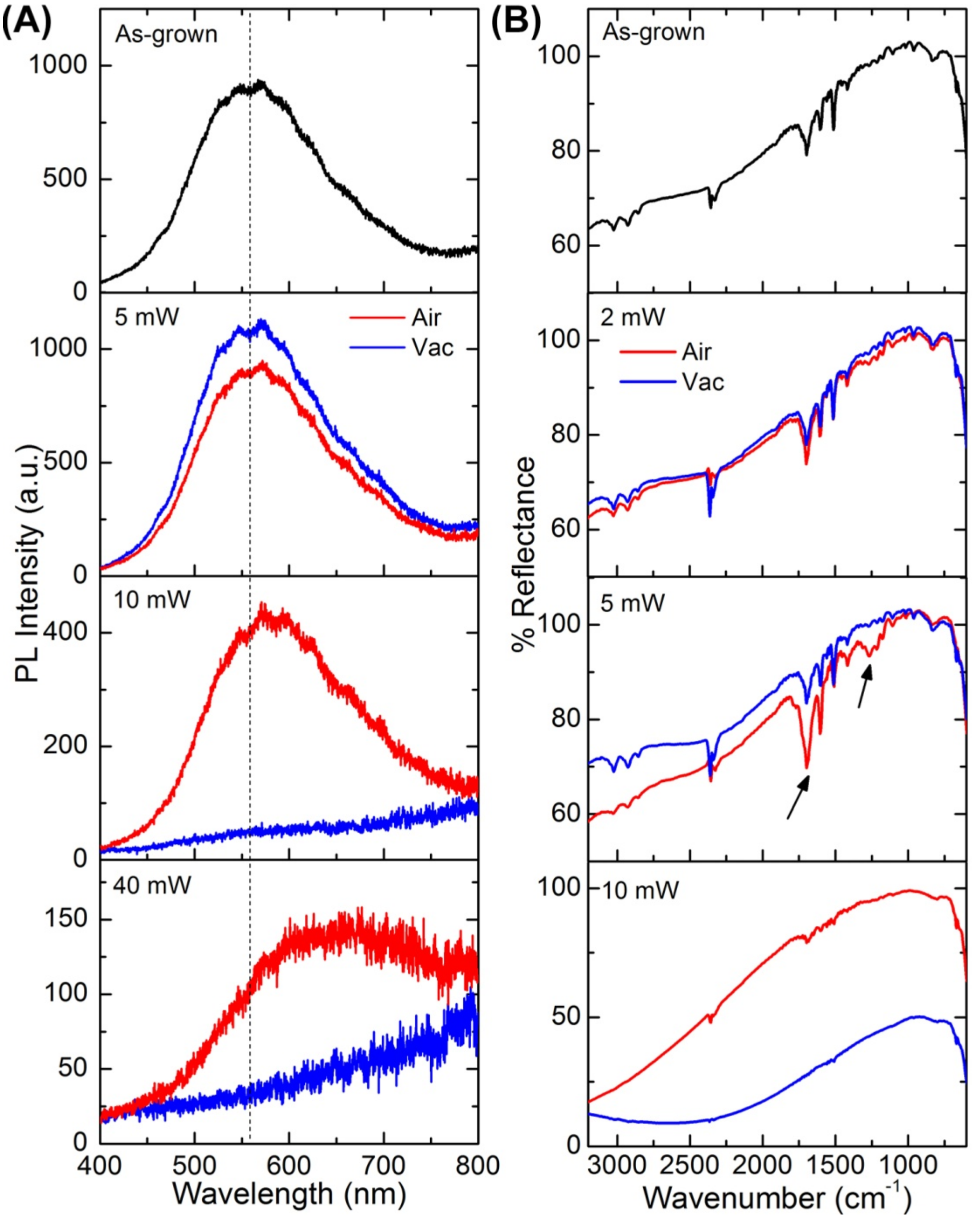

Figure 3.15: (A) PL and (B) DR-FTIR spectra of PPV NTs, as-grown and laser-modified in air and vacuum by focused green laser. (Excitation wavelength for PL: 325 nm)

Compared to red laser, the green laser had caused obvious PL red-shift effect at even lower laser power (10 mW). This could be due to the higher absorbance of PPV NTs array at 532 nm compared to that at 660 nm (refer Figure 3.6). With higher absorbance, the percentage of energy uptake by

PPV from that particular laser wavelength is higher even at the same laser power. To demonstrate this, a few calculations were carried out using the following Equation 3.4 to 3.9:

Absorbance, $A = -\log_{10}(\frac{I}{I_0})$ (3.4)

% Absorption of incident radiation, $I_{abs} = (1 - \frac{I}{I_0}) \times 100\ \%$ (3.5)

$= (1 - 10^{-A}) \times 100\ \%$ (3.6)

Time taken for laser beam to remain at one position, $t = \frac{d_L}{v_R}$ (3.7)

Energy provided by laser beam, $E_L = \frac{P_L\ t}{A_L}$ (3.8)

Energy absorbed by PPV at particular wavelength, $E_{abs} = I_{abs} \times E_L$ (3.9)

where I_0 and I are the intensities of radiation before and after absorption by PPV, d_L is the diameter of laser beam (~5 μm), v_R is raster speed of patterning (65 μm/s), P_L is the laser power (W) and A_L is the area of laser spot (mm^2). Results of the calculations were compiled in Table 3.3. The table clearly illustrates that energies absorbed by PPV at 2, 5 and 10 mW of focused green laser are similar to that at 20, 30 and 40 mW of focused red laser, respectively. This suggests a reason for efficient laser pruning of PPV NTs arrays at laser power as low as 2 mW using focused green laser while the same occurred at 20 mW for red laser. Similarly, PL red-shift effect was significant at 10 mW for focused green laser while it was at 30 mW or 40 mW for focused red laser. As for unfocused blue laser irradiation, the energy absorbed by PPV was actually similar to that when PPV was subjected to 40 mW focused red laser and 10 mW focused green laser. Hence, the effect of this global blue laser irradiation may be similar to that when under these lasers. However, PPV was not visibly cut using the blue laser, probably because it was not focused to a tight laser spot.

Table 3.3: Energy provided by laser spot and energy absorbed by PPV NTs at the specified wavelengths.

	Red			**Green**				**Blue**
λ (nm)	660			532				405
A_L (mm^2)	1.963×10^{-5}			1.963×10^{-5}				78.54
t (s)	0.0769			0.0769				1560
A	0.0057			0.0320				0.6976
I_{abs} (%)	1.31			7.11				79.93
P_L (mW)	20	30	40	2	5	10	40	0.118
E_L (J/mm^2)	78.35	117.52	156.70	7.83	19.59	39.17	156.70	2.34
E_{abs} (J/mm^2)	1.03	1.54	2.05	0.56	1.39	2.78	11.14	1.87

3.3 Summary

In summary, free-standing arrays of 1D PPV NWs and NTs were successfully prepared via electrochemical polymerization of TBX inside the nanochannels of AAO template. The tubular segment of these NWs and NTs can be manipulated by using as-received or distilled plating solution as well as controlling the applied cathodic potential, while their lengths can be controlled by the electrodeposition duration. DR-FTIR spectra provided fingerprint of PPV and suggested slight oxidation of the as-grown PPV NWs and NTs. Comparing the UV-visible absorption with the literatures, we believe this synthesis method produces PPV with shorter conjugation lengths of the polymer chains. Both PPV NWs and NTs exhibit intense but broad PL spectra.

Patterning of PPV NWs and NTs were successfully demonstrated using laser pruning technique that employs focused laser beam. Both red (660 nm) and green (532 nm) lasers showed feasibility to pattern the 1D nanostructures array. Interesting “red-shifting” of the PL maxima was observed upon laser modification in air but not in inert (vacuum and helium) environment. This was found to correlate with the oxidation of PPV upon exposure to focused laser beam. We then attempted to induce photo-oxidation of PPV NTs via an unfocused blue laser irradiation. Similar to that observed in the literature, UV-visible and FTIR spectra respectively indicated scission of polymer chain and increase of C=O peak due to oxidation. In contrary, PL peak red-shifted upon irradiation in air although it remained the same for that treated in vacuum. To the best of our knowledge, there was no report in the literature on oxidation of PPV that caused red-shifting of PL. Hence, oxidation upon laser modification should not be the only reason for the red-shifting PL observed.

We postulate that the laser modification may have introduced some trap intermediate states in the band gap, leading to a red-shift of PL maximum. However, more studies should be carried out to further understand this phenomenon.

3.4 References

1. S. R. Forrest. *Nature* **428** (2004) 911-918.
2. G. Malliaras, R. Friend. *Phys. Today* **58** (2005) 53-58.
3. A. N. Aleshin. *Adv. Mater.* **18** (2006) 17-27.
4. J. Jang, V. Springer. Conducting Polymer Nanomaterials and Their Applications, in: Emissive Materials: Nanomaterials, Springer-Verlag Berlin, Berlin, 2006, pp. 189-259.
5. L. Liu, Y. M. Zhao, N. Q. Jia, Q. Zhou, C. J. Zhao, M. M. Yan, Z. Y. Jiang. *Thin Solid Films* **503** (2006) 241-245.
6. Y. Z. Long, M. M. Li, C. Z. Gu, M. X. Wan, J. L. Duvail, Z. W. Liu, Z. Y. Fan. *Prog. Polym. Sci.* **36** (2011) 1415-1442.
7. R. H. Friend, D. D. C. Bradley, P. D. Townsend. *J. Phys. D: Appl. Phys.* **20** (1987) 1367-1384.
8. J. H. Burroughes, D. D. C. Bradley, A. R. Brown, R. N. Marks, K. Mackay, R. H. Friend, P. L. Burns, A. B. Holmes. *Nature* **347** (1990) 539-541.

9. J. I. Jin, H. K. Shim. Nonlinear-Optical Properties of Poly(1,4-Phenylenevinylene) and Its Derivatives, in: G.A. Lindsay, K.D. Singer (Eds.) Polymers for Second-Order Nonlinear Optics, 1995, pp. 223-238.

10. R. A. Wessling. *J. Polym. Sci., Pol. Sym.* (1985) 55-66.

11. J. D. Stenger-Smith, R. W. Lenz, G. Wegner. *Polymer* **30** (1989) 1048-1053.

12. A. Marletta, D. Goncalves, O. N. Oliveira, R. M. Faria, F. E. G. Guimaraes. *Adv. Mater.* **12** (2000) 69-74.

13. K. Kim, J. I. Jin. *Nano Lett.* **1** (2001) 631-636.

14. F. Massuyeau, J. L. Duvail, H. Athalin, J. M. Lorcy, S. Lefrant, J. Wery, E. Faulques. *Nanotechnology* **20** (2009) 155701.

15. Y. Xin, Z. H. Huang, E. Y. Yan, W. Zhang, Q. Zhao. *Appl. Phys. Lett.* **89** (2006) 053101.

16. W. Zhang, Z. H. Huang, E. Y. Yan, C. Wang, Y. Xin, Q. Zhao, Y. B. Tong. *Mater. Sci. Eng., A* **443** (2007) 292-295.

17. Y. Xin, Z. B. Ling, S. Y. Li, T. T. Lin, G. D. Liu. *Mater. Sci. Eng., B* **177** (2012) 1094-1097.

18. T.-H. Kim, S.-M. Park. *Electrochim. Acta* **50** (2005) 1461-1467.

19. H. Nishihara, M. Akasaka, M. Tateishi, K. Aramaki. *Chem. Lett.* (1992) 2061-2064.

20. S. I. Cho, W. J. Kwon, S. J. Choi, P. Kim, S. A. Park, J. Kim, S. J. Son, R. Xiao, S. H. Kim, S. B. Lee. *Adv. Mater.* **17** (2005) 171-175.

21. S. I. Cho, D. H. Choi, S. H. Kim, S. B. Lee. *Chem. Mater.* **17** (2005) 4564-4566.

22. R. Xiao, S. Il Cho, R. Liu, S. B. Lee. *J. Am. Chem. Soc.* **129** (2007) 4483-4489.

23. O. Reynes, S. Demoustier-Champagne. *J. Electrochem. Soc.* **152** (2005) D130-D135.

24. C. R. Martin. *Adv. Mater.* **3** (1991) 457-459.

25. C. R. Martin. *Chem. Mater.* **8** (1996) 1739-1746.

26. K. Honda, Y. Furukawa, H. Nishide. *Vib. Spectrosc.* **40** (2006) 149-154.

27. A. Sakamoto, Y. Furukawa, M. Tasumi. *J. Phys. Chem.* **96** (1992) 1490-1494.

28. B. Tian, G. Zerbi, R. Schenk, K. Mullen. *J. Chem. Phys.* **95** (1991) 3191-3197.

29. B. Tian, G. Zerbi, K. Mullen. *J. Chem. Phys.* **95** (1991) 3198-3207.

30. T. P. Nguyen, V. H. Tran, P. Destruel, D. Oelkrug. *Synth. Met.* **101** (1999) 633-634.

31. E. Mulazzi, A. Ripamonti, J. Wery, B. Dulieu, S. Lefrant. *Phys. Rev. B* **60** (1999) 16519-16525.

32. W. P. Chang, W. T. Whang, P. W. Lin. *Polymer* **37** (1996) 1513-1518.

33. K. Y. Lim, C. H. Sow, J. Y. Lin, F. C. Cheong, Z. X. Shen, J. T. L. Thong, K. C. Chin, A. T. S. Wee. *Adv. Mater.* **15** (2003) 300-303.

34. T. Zyung, J. J. Kim. *Appl. Phys. Lett.* **67** (1995) 3420-3422.

35. C. D. Wagner, W. M. Riggs, L. E. Davis, J. F. Moulder. *Handbook of X-ray Photoelectron Spectroscopy: A Reference Book of Standard Spectra for Identification and Interpretation of XPS Data* G.E. Muilenberg, Perkin-Elmer Corporation, Physical Electronics Division, Eden Prairie, Minnesota, U.S.A. (1979).
36. G. G. Andersson, W. J. H. van Gennip, J. W. Niemantsverdriet, H. H. Brongersma. *Chem. Phys.* **278** (2002) 159-167.
37. S. Chambon, A. Rivaton, J. L. Gardette, M. Firon. *Polym. Degrad. Stab.* **96** (2011) 1149-1158.
38. Y. G. Gobato, A. Marletta, R. M. Faria, F. E. G. Guimaraes, J. M. de Souza, E. C. Pereira. *Appl. Phys. Lett.* **81** (2002) 942-944.

Chapter 4

Synthesis of Controllable Core-shell Nanostructures via Pore Widening Method

Core-shell NTs and NWs with coupled core and shell materials have been of great scientific and technological interests due to their potential applications in solar cells, sensors and energy storage.[1-4] Various core-shell 1D hetero-nanostructures have been explored with varied combinations of semiconductor, metal, metal oxide and conductive polymer.[1-16] Some of these hetero-nanostructured architecture reported functional advantages such as protection of the core material from oxidation,[5] or formation of coaxial *p*-*i*-*n* junction.[1] Others also demonstrated enhanced performance due to synergistic effect between the core and the shell components.[3, 4]

Arising from the above advantages, much effort has been dedicated to explore simple and versatile synthetic strategies to prepare core-shell 1D hetero-nanostructures. Various synthetic strategies have been proposed, including redox reaction,[6] atomic layer deposition (ALD),[7] electrospinning[8] and high-temperature chemical vapour deposition (CVD).[1, 5, 9-11] However, these methods often include the use of bulky equipment, high temperature and high vacuum system which increases the cost of fabrication. Template-assisted synthesis using nanoporous membranes such as AAO is certainly a cheaper alternative. A range of methodologies have been employed together with AAO, such as sol-gel,[12] pyrolysis,[13] surface thermal oxidation,[14] core shrinkage[15] and pore etching,[16] to generate core-shell structures.

One of the attractive attributes of template-assisted synthesis method is the potential to control the dimensions of the core and shell components independently. However, it is normally more difficult to control the thickness of the shell component. In the “core shrinkage” method,[15] while the length of the gold sheath in the polyaniline (PANI)/Au core-shell nanostructures could be controlled, the control of shell thickness remains a challenge. Another work which reports on pore-etching using diluted NaOH solution also did not show control of the shell thickness.[16, 17] Fast dissolution of AAO may make NaOH unsuitable for precise control of the pore-etching and thus the consequent shell thickness. Hence, it would be more meaningful to find a general way that can achieve core-shell structures composed of different materials.

In this Chapter, a versatile “Pore Widening” method that can lead to various multi-layered 1D hetero-nanostructures with adjustable shell thickness is reported. Here, diluted phosphoric acid (H_3PO_4) was used instead of NaOH, which offers more control on the size of the annular gap in the AAO nanochannels and consequently the thickness of the shell. The versatility of this approach would be demonstrated through the fabrication of various types of bi- and multi-layered core-shell NWs and NTs.

4.1 Synthesis and characterizations of core-shell nanostructures

The strategy for the growth of core-shell nanostructures arrays is illustrated in Figure 4.1. For demonstration purpose, materials employed are polypyrrole (PPy) as the conductive polymer and copper (Cu), nickel (Ni) and gold (Au) as the choice of metal components. Synthesis parameters for each component were detailed in Section 2.2.2. As shown in Figure 4.1, polymer (or first metal M1) was first electrodeposited into the nanochannels of AAO (Step 1). We then immersed the AAO containing the cores into 6 wt.% H_3PO_4 (Step 2). Such solution was found to slowly remove the AAO nanochannel walls, leaving an annular gap around the as-prepared cores (“Pore Widening”). Metal (or second metal M2) was subsequently electrodeposited into the gap (Step 3) and 1D core-shell nanostructure array could be achieved after removing the template with 1M NaOH (Step 4).

Since 6 wt.% H_3PO_4 and 1 M NaOH are respectively used for pore-widening and template removal, the choice of materials for the core and inner shell layer is limited to those inert to the 6 wt.% H_3PO_4 and 1 M NaOH. Nonetheless, through judicious selection of materials and sequences of steps, this “Pore Widening” method remain versatile and various desired layered 1D nanostructures can be prepared. Using this “Pore Widening” strategy as shown in Figure 4.1, deposition of a range of coaxial 1D hetero-nanostructures such as polymer/metal, metal/metal, polymer/metal/metal and metal oxide/metal core-shell nanostructures, will be demonstrated in the following sub-sections.

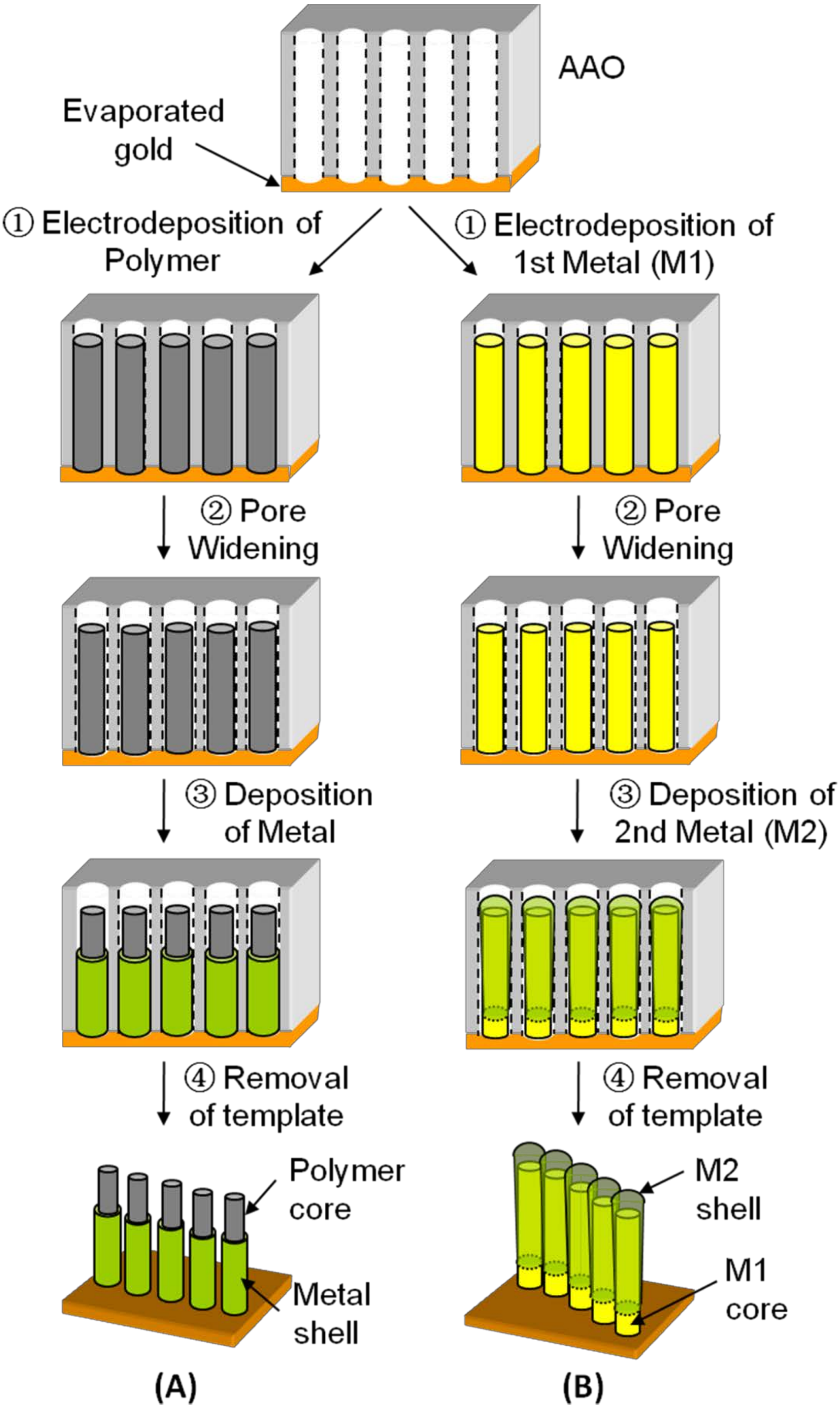

Figure 4.1: Schematic of the "Pore Widening" steps to generate (A) polymer/metal and (B) metal/metal (M1/M2) core-shell nanostructures.

4.1.1 Polymer/metal core-shell nanowires

Polymer/metal core-shell NWs such as PPy/Ni can be obtained via the procedure illustrated in Figure 4.1A. In this case, there is no limitation to the choice of core polymer because most polymers are inert to 6 wt.% H_3PO_4 but the shell metal must be inert to 1 M NaOH. Before subsequent deposition of metal shell, the core (PPy NWs) must be ensured to be longer than the prospective height of the shell to-be grown so as to prevent the core from being over-grown by the shell. To enable estimation of the length of PPy NWs, the growth was first calibrated as function of charge deposited. Shown in Figure 4.2A is the SEM image representative of the PPy NWs. From the SEM characterization, length of the NWs with respect to charge deposited was obtained as shown in Figure 4.2B. As expected, the length of the polymer NWs increases linearly with respect to the charge deposited.

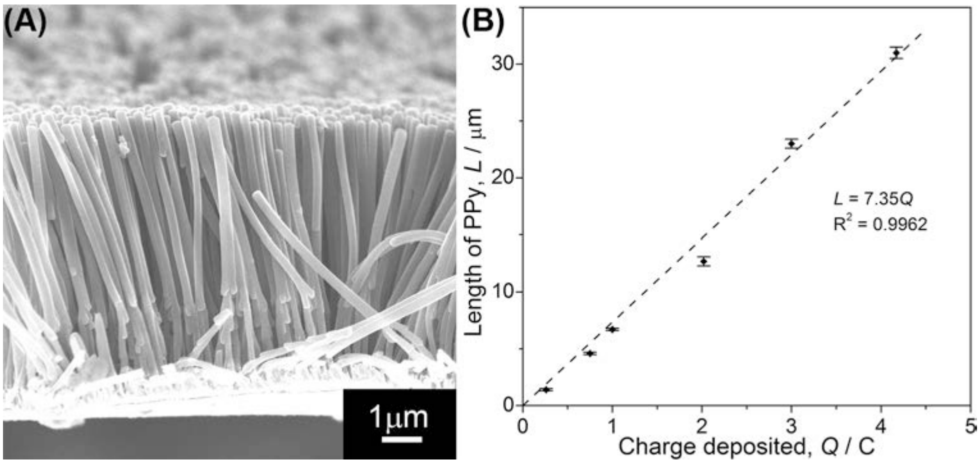

Figure 4.2: (A) SEM image of as-grown PPy NWs array and (B) graph of length of PPy NWs as a function of charge deposited.

The final PPy/Ni core-shell NWs was characterized using SEM and Figure 4.3 shows the side views (A and B) and top views (C and D) SEM images of the core-shell NWs after widening the pores for 1 hour (A, C) and 2 hours (B, D), respectively. The formation of a layer of metal shell around the core polymer after the “Pore Widening” procedure is clearly illustrated. The success of this strategy hinges on the fact that 6 wt.% H_3PO_4 can gently dissolve and polish the walls of the AAO nanochannels, which was the reason for this acid to be widely used in the final step of making AAO membrane.[18, 19] A closer examination of the SEM images shows that the metal sheath grows thicker with the increase of the pore-widening time. The average shell thickness are estimated to be 25 nm and 55 nm for the pore-widening time of 1 hour (Figure 4.3A, C) and 2 hours (Figure 4.3B, D), respectively. This is as expected because the annular gap is created by the slow dissolution of AAO channel walls by the diluted H_3PO_4. The longer the AAO is immersed in the acidic solution for pore-widening, the more AAO is dissolved to give larger annular gap, leading to thicker shell layer.

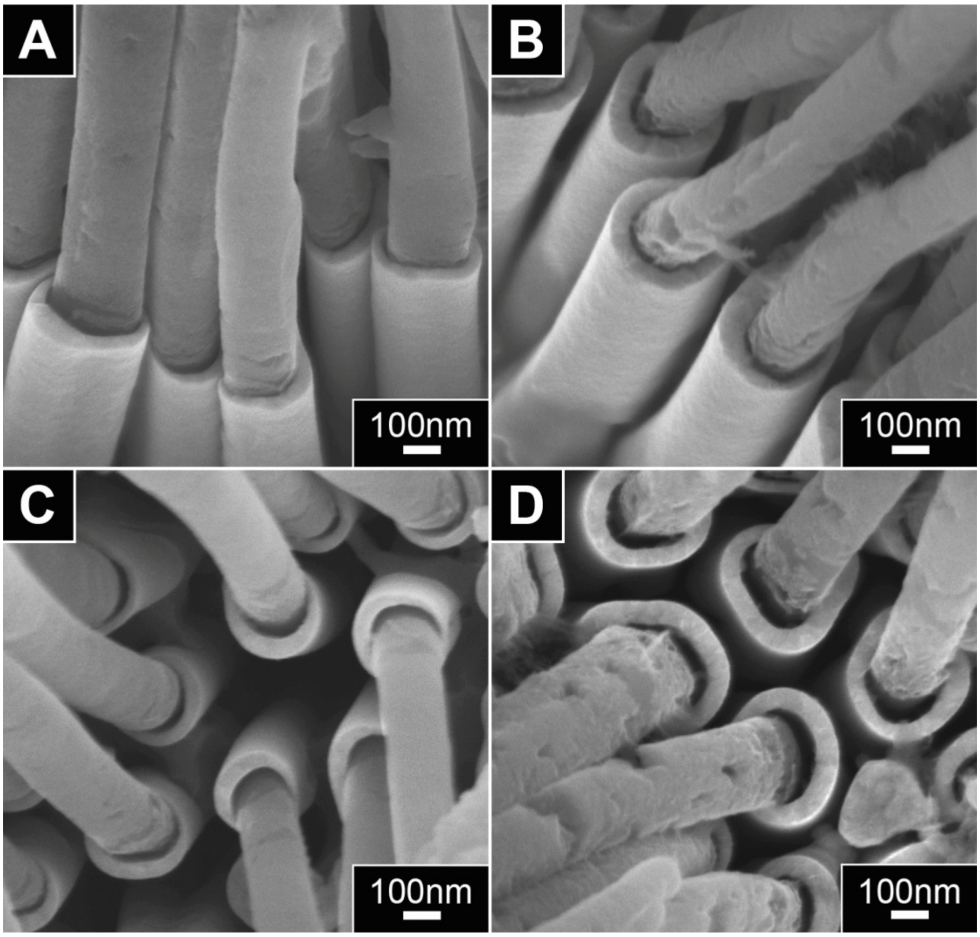

Figure 4.3: Side (A and B) and top view (C and D) SEM images of the PPy/Ni core-shell NWs prepared after pore widening for 1 hour (A, C) and 2 hours (B, D), respectively.

In order to clearly show the shell thickness, the nanostructures were exposed to oxygen reactive ion etching (O_2 RIE) (Section 2.5) for 15 mins which partially remove the extending PPy NWs. With the obstructing PPy NWs being removed, the SEM images in Figure 4.4A and B now evidently show the difference in shell thickness corresponding to varying pore-widening time. By systematically varying the duration of pore-widening, a calibration plot of shell thickness as function of pore-widening time was obtained as shown in Figure 4.4C. Shell thickness was found to increase linearly with pore-widening time, clearly demonstrating the ability of this method in controlling the shell thickness. In addition, this method also enables deposition of shells made of various type of metals, only by using different plating solution during the stage of metal shell deposition (Step 3 in Figure 4.1A). Now, different PPy/metal core-shell NWs in varying shell thickness, including Ni, Au and Cu can be readily prepared. One example shown here in Figure 4.4D is the PPy/Cu core-shell NWs array.

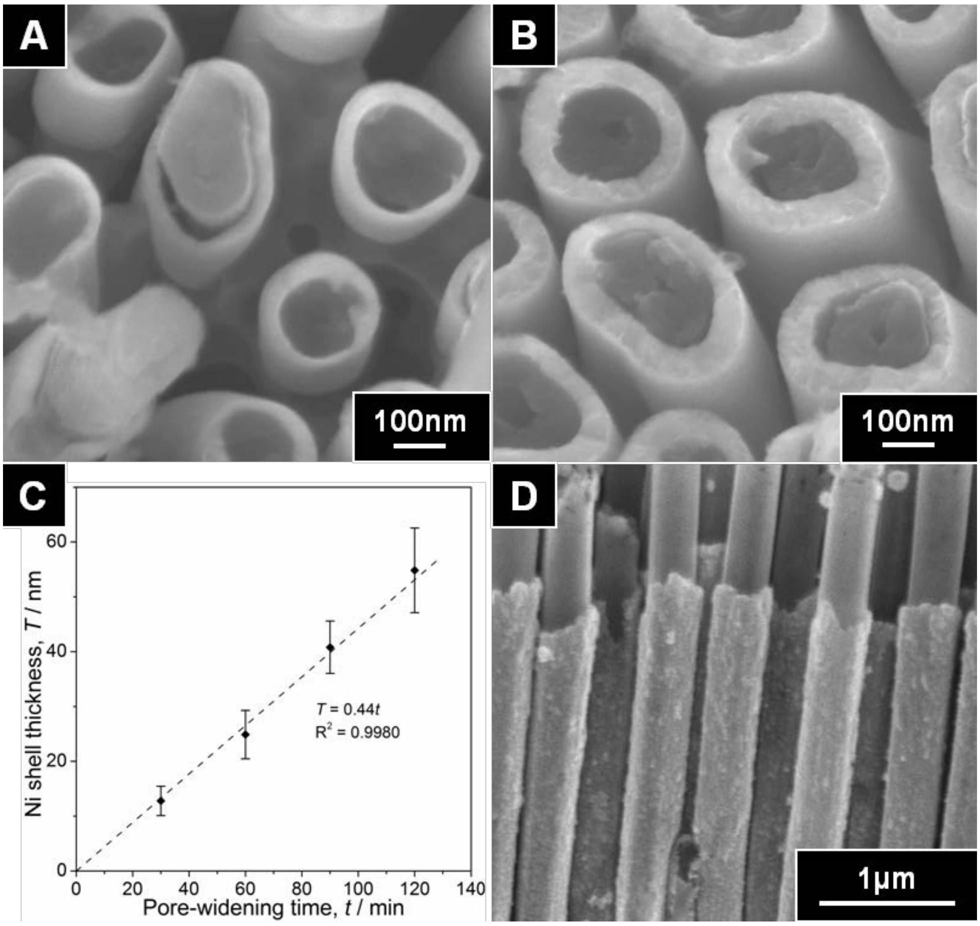

Figure 4.4: (A, B) Top view SEM images of the core-shell PPy/Ni NWs prepared at pore-widening time of (A) 1 hour and (B) 2 hours after exposure to oxygen reactive ion etching for 15 minutes. (C) Graph of Ni shell thickness as function of pore-widening time. (D) Side view SEM image of PPy/Cu core-shell NWs array.

Since it is well-known that polymers can be readily removed by suitable solvent dissolution or heat treatment,[8, 20] they may serve as “soft template” for the fabrication of NTs with controllable wall thickness via our “Pore Widening” method. This thus opens up another way of making NTs and even multi-layered NTs (which will be demonstrated in the following Section 4.1.4), in addition to previously reported NTs synthesis.[8, 12, 21, 22] Here, we illustrate a one-step process to obtain nickel oxide NTs using heat treatment in air (Section 2.5). Figure 4.5A show the SEM image of the same PPy/Ni sample as in Figure 4.3A after heat treatment at 400°C for 3 hours in ambient air. Indeed the high temperature burnt away the PPy NWs, leaving behind an array of free-standing NTs.

After the heat treatment, it is noted that the shell surface become roughened and the thickness increased from about 25 nm to about 60 nm. Both these observations suggested that the Ni shell have been oxidized into Ni oxide during the treatment. This is indeed confirmed by EDX analysis (Section 2.9.3) as shown in Figure 4.5B, which shows a clear oxygen peak for sample after the heat treatment. The roughening of the surface and increased thickness of NTs are due to expansion caused by the intercalation of oxygen into the crystal lattice of Ni metal during the heat treatment.

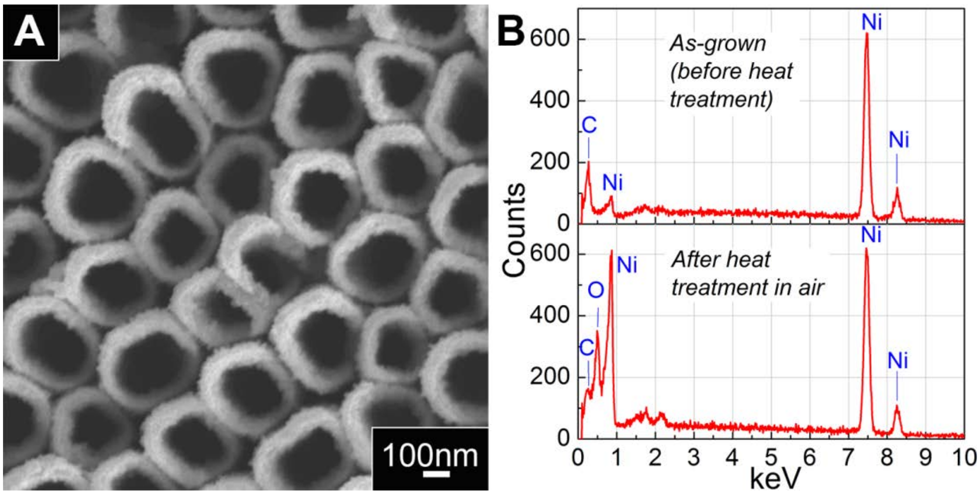

Figure 4.5: Analysis of PPy/Ni core-shell NWs shown in Figure 4.3A after heat treatment at 400°C in air for 3 hours. (A) Top view SEM image, and (B) a comparison of the EDX spectra before and after the heat treatment.

4.1.2 Metal/metal core-shell nanowires

This pore-widening approach also allows fabrication of metal/metal core-shell NWs. As already mentioned, the choice of metal for the core is limited to those inert to the 6 wt.% H_3PO_4 used for pore-widening step. The synthesis procedures follow the steps as illustrated in Figure 4.1B for deposition of M1/M2 core-shell nanostructures. As an example, Cu/Ni core-shell NWs was prepared using this method where Cu and Ni are the M1 and M2, respectively. The resulting morphology is as shown in the SEM image in Figure 4.6. The Ni shell and Cu core are clearly distinguishable since the surface of Cu portions often appear roughen due to the formation of a thin layer of oxide when exposed to air. To further confirm the location of the Ni shell and Cu core, EDX analyses (Section 2.9.3) were carried out at three different locations: the tip (a), the trunk (b) and the root (c) of the NWs. From the EDX spectra in Figure 4.6a-c, it is noticed that the relative intensity of Ni to Cu peak gradually decreases from the tips to the roots of the NWs. This indicates that Ni shells are grown capped at the tips of Cu NWs.

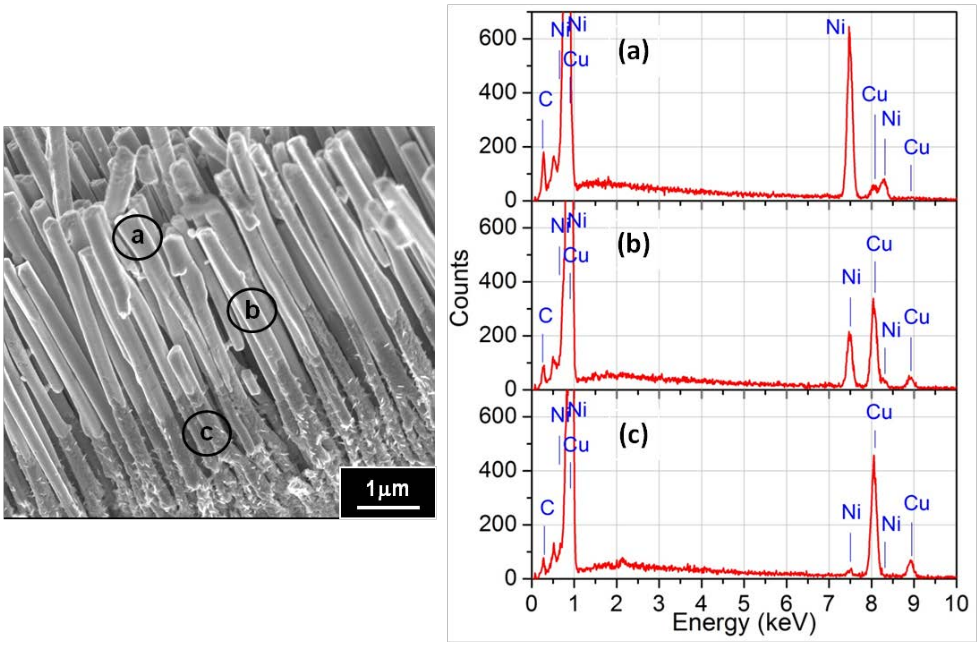

Figure 4.6: Cu/Ni core-shell NWs array prepared using the “Pore Widening” method. The EDX spectra on the right were taken at three different locations marked as a, b and c on the SEM image on the left.

A question thus arise: why does the morphology of the metal/metal core-shell NWs (Figure 4.6) differ from that of the polymer/metal core-shell NWs (Figure 4.3)? Here, an attempt to rationalize the growth mechanism is shown schematically in Figure 4.7. While doped PPy is a conductive polymer, its conductivity is inferior in comparison to metal. Thus, atoms of the shell metal will have higher tendency to deposit directly onto the gold cathode, causing the shell growth to start from the bottom of the widened

AAO nanochannels (Figure 4.7A). Similar mechanism had been proposed for the preparation of PANI/Au core-shell nanostructure.[15]

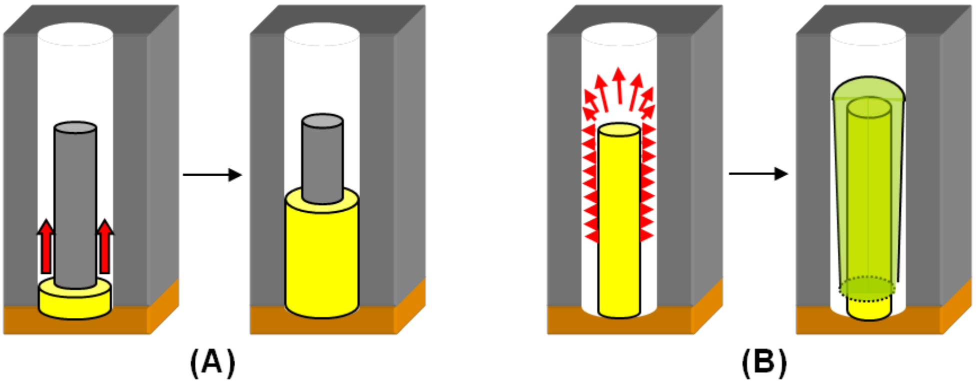

Figure 4.7: Schematic of the growth mechanism of (A) polymer/metal and (B) metal/metal core-shell NWs in a single nanochannel of AAO template.

On the other hand, for fabrication of metal/metal (M1/M2) core-shell NWs, the shell deposition can also occur along the length of the conducting core metal (M1) inside the widened nanochannels as shown in Figure 4.7B. Due to "point effect", the deposition of shell metal (M2) will be more pronounced on the tip rather than at the root of the core metal. The shell layer would quickly build up at the tips, blocking any diffusion of metal ions into the bottom gold cathode. This thus prevents the growth of shell at the cathode or at the root of the core metal, resulting in something like the "baseball bat" nanostructure as observed in Figure 4.6.

4.1.3 Multi-layered nanowires

In clear contrast to the "core shrinkage" method,[15] deposition is certainly not limited to one single shell component in our method. Additional "Pore

Widening" step can be advantageously applied to create space for subsequent deposition of second layer of shell to give multi-layered NWs. The synthesis steps are as shown schematically in Figure 4.8. Here, the polymer/metal core-shell NWs obtained after Step 3 in Figure 4.1A is subjected to second pore-widening step which opens up an annular gap followed by deposition of second shell layer.

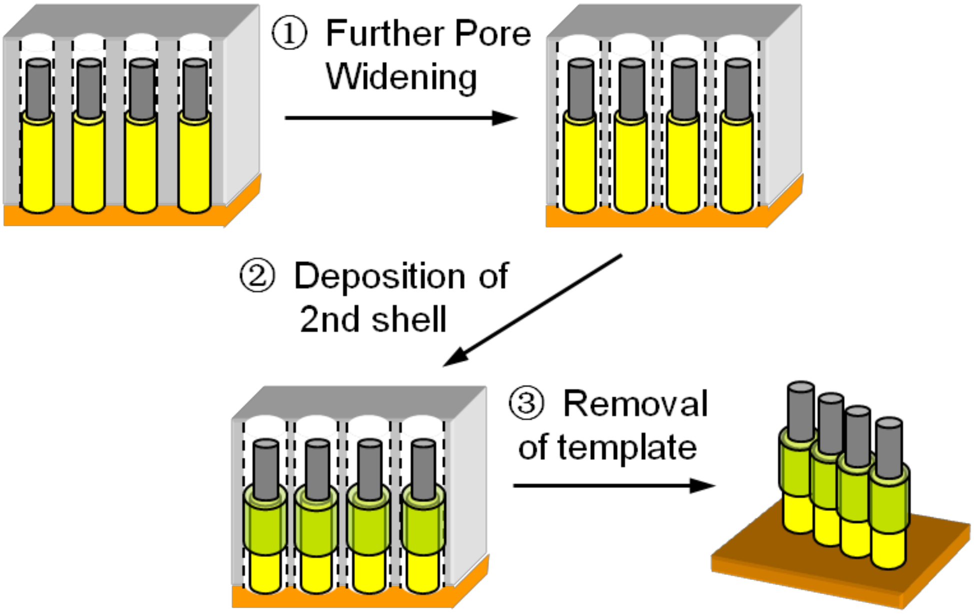

Figure 4.8: Schematic of further "Pore Widening" strategy for synthesis of polymer/metal/metal tri-layered core-shell NWs by repeating steps depicted in Figure 4.1.

An example of such multi-layered core-shell nanostructures is PPy/Cu/Ni tri-layered core-shell NWs, with the PPy as the core, and Cu and Ni as the first and second shell layer, respectively. The resulting morphology is as shown in a typical SEM image in Figure 4.9B. As observed from this SEM image, the outmost shell layer (Ni) appears to be coating only at the tips of the inner shell layer (Cu), based on the slight difference in the brightness of the image.

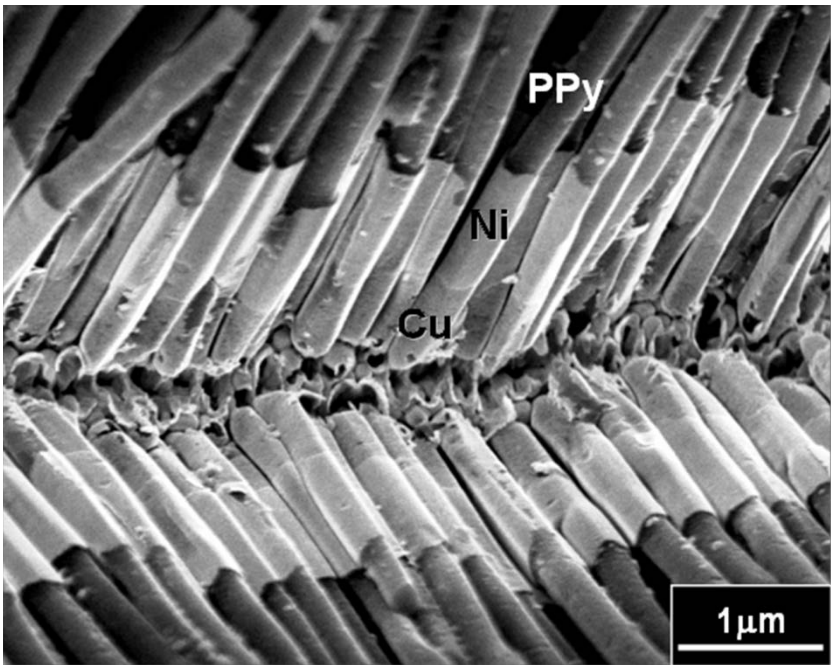

Figure 4.9: SEM image of PPy/Cu/Ni tri-layer core-shell NWs.

To prove the presumption above, elemental profile of this tri-layered nanostructure was obtained from EDX line analysis (Section 2.9.3) as shown in Figure 4.10. It is clearly shown here that the tips of the shell consists mostly of Ni while nearer to the root of the NWs shows larger amount of Cu, indicating that the inner shell layer is exposed. These observations proved that the outmost second metal shell (Ni) is deposited only at the tips but not at the root of the first metal shell layer (Cu). This correlates to the "point effect" growth mechanism which was discussed in previous section (Section 4.1.2) for the deposition of metal/metal core-shell NWs.

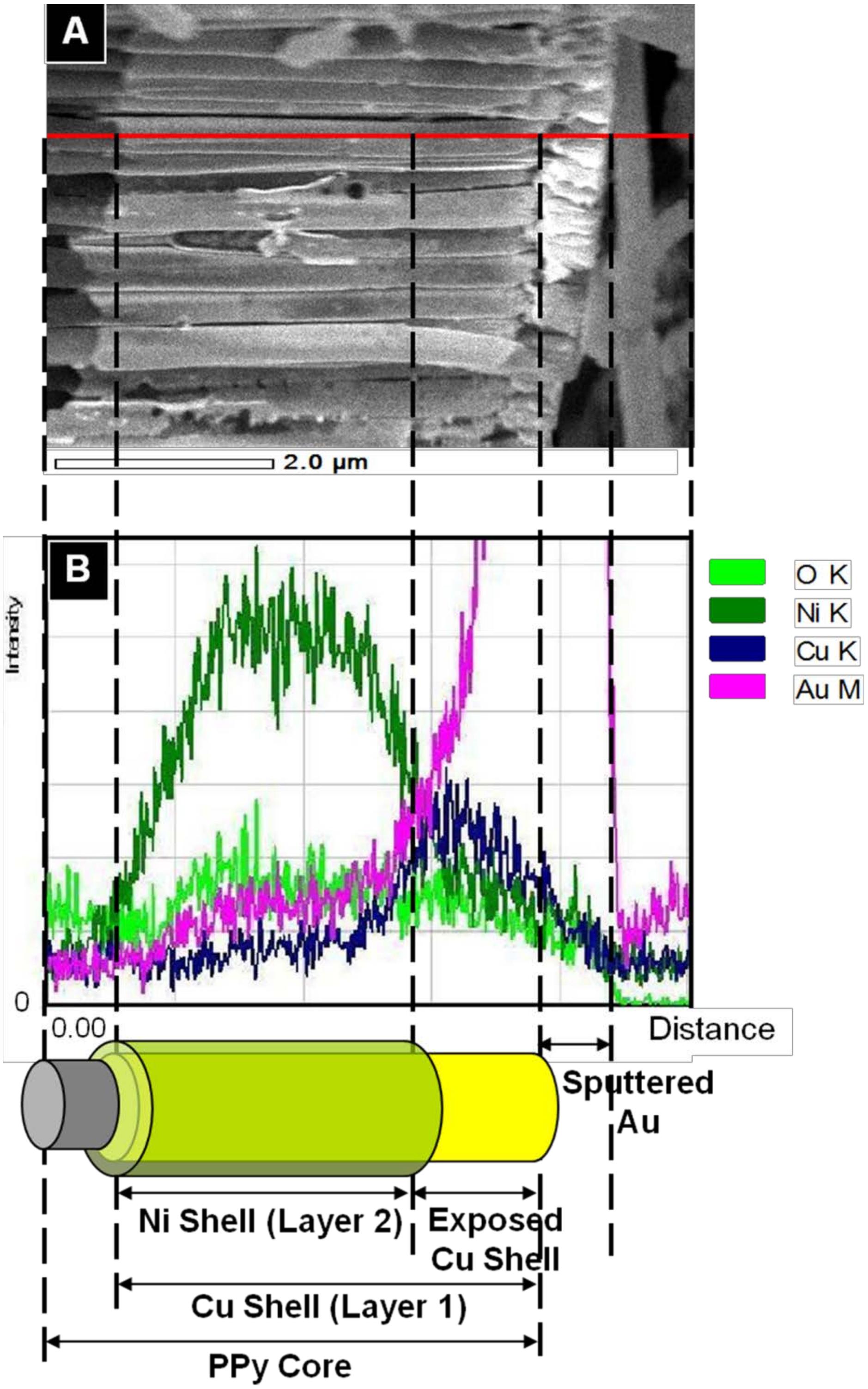

Figure 4.10: EDX line analysis of the tri-layered NWs: (A) SEM image of the PPy/Cu/Ni tri-layered core-shell NWs array and (B) the compositional line profiles probed by EDX along the red line in (A), showing well-correlated Ni and Cu signals along the NW axis.

4.1.4 Multi-layered nanotubes

The versatility of this "Pore Widening" method can be further demonstrated by generating multi-layered NTs via a sensible selection of materials and sequences of steps. As an example, Figure 4.11 shows the utilization of the "Pore Widening" method to fabricate metal oxide/metal double-walled NTs (DWNT). In this case, PPy/Cu core-shell NWs obtained via procedures in Figure 4.1A would be the starting material. The core-shell NWs was then subjected to further pore-widening step to provide additional space for deposition of second layer of shell. Subsequently, the sample was heated to 300 °C for 40 minutes to decompose the PPy core as well as to oxidize the Cu shell to Cu_xO, followed by deposition of second shell layer. Removal of the template then resulted in the final Cu_xO/metal DWNT arrays.

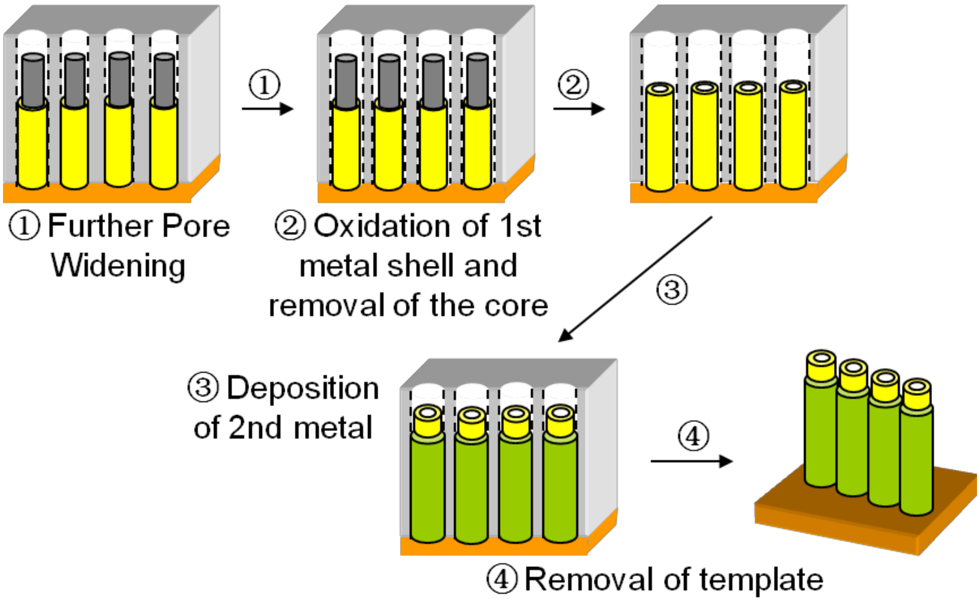

Figure 4.11: Schematic procedures for the synthesis of metal oxide/metal DWNT.

Here, Ni was used as the second shell metal and morphology of the resulting Cu_xO/Ni DWNT array is as shown in Figure 4.12B. Since Cu_xO is insulating, the subsequent metal shell deposition was found to start from the bottom electrode, thus forming a fairly uniform Cu_xO/Ni DWNT.

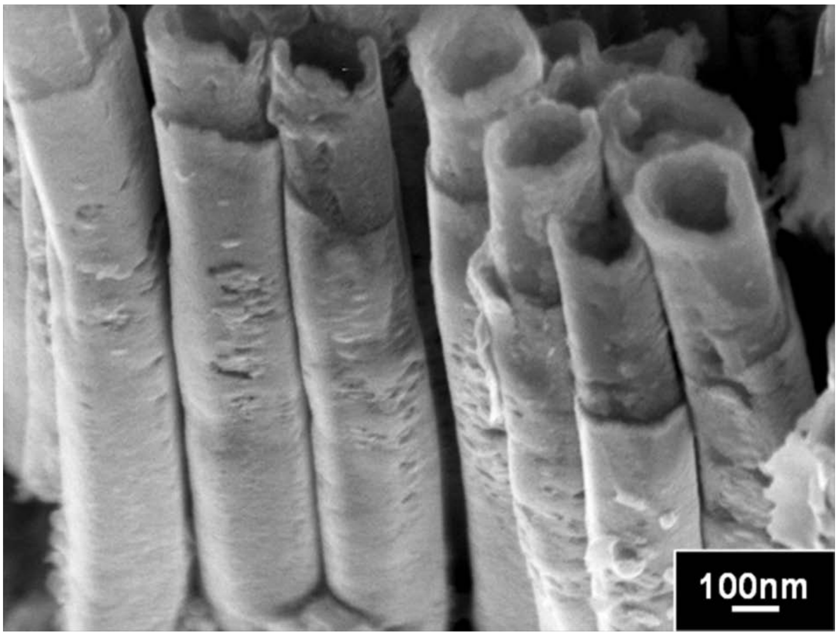

Figure 4.12: SEM image showing Cu_xO/Ni DWNT.

To confirm the elemental profile of this DWNT, EDX line analysis (Section 2.9.3) were carried out and the spectrum obtained is as shown in Figure 4.13. The cartoon at the bottom of the figure act as illustration for clear understanding of the EDX spectrum. Based on this analysis, the tips of the DWNT consist of mainly Cu with certain amount of O, indicating presence of Cu_xO which was supposed to be the inner wall. These signals from the inner wall are detected since the inner wall is not over-grown by the outer shell and is seen protruding from the DWNT in the SEM images in both Figure 4.12B and Figure 4.13. Meanwhile, the outmost layer from the root of the NTs shows signal of Ni, confirming the part grown as the outer shell consists of Ni. This demonstrates the successful deposition of Cu$_x$O/Ni DWNT via the “Pore Widening” method.

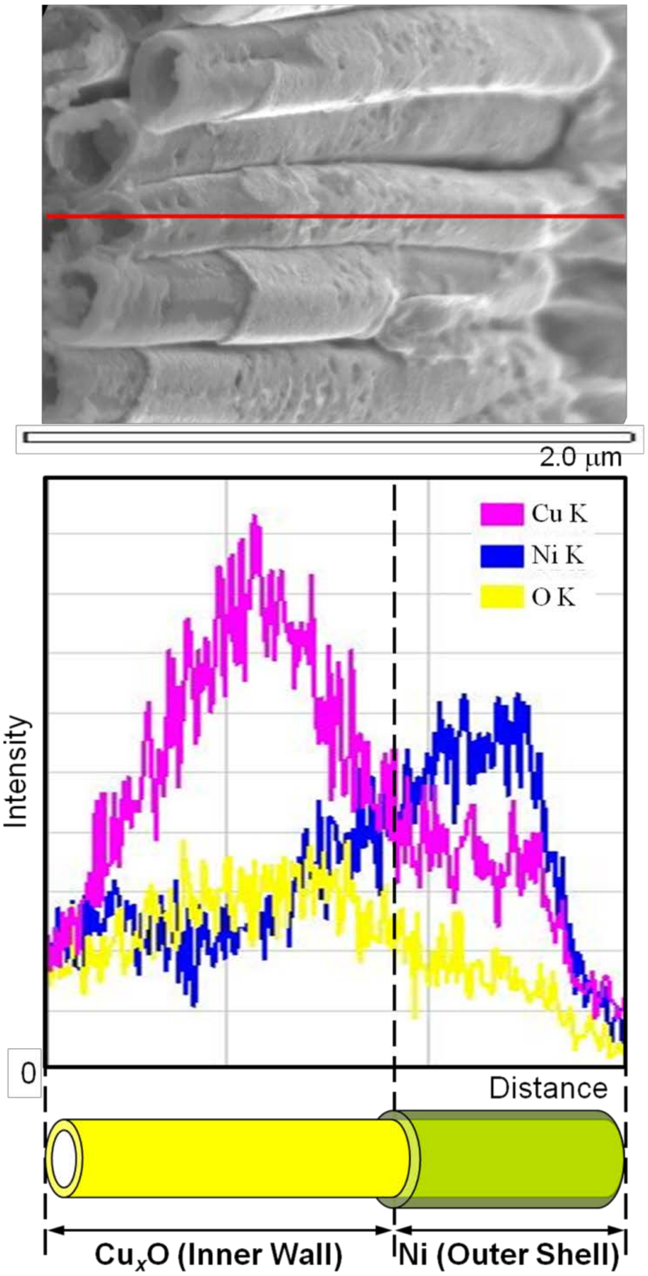

Figure 4.13: EDX line analysis of the Cu$_x$O/Ni DWNT, indicating a fairly uniform distribution of the metal and oxide.

4.2 Summary

The versatility of “Pore Widening” method in creating various coaxial multi-layered 1D hetero-nanostructures was successfully demonstrated. Diluted H_3PO_4, which has been used to chemically remove the barrier layer during the fabrication of AAO membrane, is advantageously used here to generate an annular gap between the deposited core and the wall of AAO nanochannel. The presence of this gap thus allows deposition of another layer of material as the sheath, forming coaxial 1D hetero-nanostructure. Besides, it was shown that the size of the annular gap and thus the subsequent thickness of the shell, can be controlled by carefully tuning the duration of pore-widening. This is of course limited by the thickness of the AAO nanochannel walls.

Expanding from the architectures demonstrated here, we suggest that our “Pore Widening” method can be used to fabricate coaxially multi-layered NWs and NTs with varied combinations of materials. As in most AAO template-assisted synthesis, the final core and shell components must be inert to NaOH used to remove the template. Thus, in addition to Au, Cu, Ni and PPy demonstrated in this report, other possible materials include PANI,[11] poly(*p*-phenylene vinylene),[26, 27] silver,[28] SiO_2,[16] ZnS,[19] Bi and Bi_2O_3.[18] The additional limitation of “Pore Widening” method, of course, is that the core or inner shell material must also be inert to dilute H_3PO_4. We believe many polymeric materials are suitable in this aspect, as well as most of the inert metals and elements. Hence, we envisage that many interesting nanostructures can be generated using this “Pore Widening” approach which will be useful in potential functional devices in various areas.

4.3 References

1. B. Z. Tian, X. L. Zheng, T. J. Kempa, Y. Fang, N. F. Yu, G. H. Yu, J. L. Huang, C. M. Lieber. *Nature* **449** (2007) 885-890.
2. X. H. Xia, J. S. Luo, Z. Y. Zeng, C. Guan, Y. Q. Zhang, J. P. Tu, H. Zhang, H. J. Fan. *Sci. Rep.* **2** (2012) 981.
3. C. Y. Yan, H. Jiang, T. Zhao, C. Z. Li, J. Ma, P. S. Lee. *J. Mater. Chem.* **21** (2011) 10482-10488.
4. X. H. Xia, J. P. Tu, Y. Q. Zhang, X. L. Wang, C. D. Gu, X. B. Zhao, H. J. Fan. *ACS Nano* **6** (2012) 5531-5538.
5. Y. C. Zhu, Y. Bando, D. F. Xue, F. F. Xu, D. Golberg. *J. Am. Chem. Soc.* **125** (2003) 14226-14227.
6. X. G. Wen, S. H. Yang. *Nano Lett.* **2** (2002) 451-454.
7. J. Hwang, B. D. Min, J. S. Lee, K. Keem, K. Cho, M. Y. Sung, M. S. Lee, S. Kim. *Adv. Mater.* **16** (2004) 422-425.
8. D. Li, Y. N. Xia. *Nano Lett.* **4** (2004) 933-938.
9. Q. Li, C. R. Wang. *Appl. Phys. Lett.* **82** (2003) 1398-1400.
10. Y. B. Li, Y. Bando, D. Golberg, Z. W. Liu. *Appl. Phys. Lett.* **83** (2003) 999-1001.
11. S. Y. Bae, H. W. Seo, H. C. Choi, D. S. Han, J. Park. *J. Phys. Chem. B* **109** (2005) 8496-8502.

12. N. I. Kovtyukhova, T. E. Mallouk, T. S. Mayer. *Adv. Mater.* **15** (2003) 780-785.

13. J. C. Bao, K. Y. Wang, Z. Xu, H. Zhang, Z. H. Lu. *Chem. Commun.* (2003) 208-209.

14. L. Li, Y. W. Yang, G. H. Li, L. D. Zhang. *Small* **2** (2006) 548-553.

15. M. Lahav, E. A. Weiss, Q. B. Xu, G. M. Whitesides. *Nano Lett.* **6** (2006) 2166-2171.

16. W. R. Hendren, A. Murphy, P. Evans, D. O'Connor, G. A. Wurtz, A. V. Zayats, R. Atkinson, R. J. Pollard. *J. Phys.-Condes. Matter* **20** (2008) 362203.

17. P. R. Evans, W. R. Hendren, R. Atkinson, R. J. Pollard. *J. Electrochem. Soc.* **154** (2007) K79-K82.

18. G. E. Thompson, G. C. Wood. *Nature* **290** (1981) 230-232.

19. H. Masuda, K. Fukuda. *Science* **268** (1995) 1466-1468.

20. J. E. Mark, ed., *Polymer data handbook*, Oxford University Press, New York, 2nd edn, 2009.

21. L. Li, Y. W. Yang, X. H. Huang, G. H. Li, R. Ang, L. D. Zhang. *Appl. Phys. Lett.* **88** (2006) 103119.

22. X. C. Dou, G. H. Li, X. H. Huang, L. Li. *J. Phys. Chem. C* **112** (2008) 8167-8171.

Chapter 5

Synthesis and Electrochemical Properties of Cobalt/Aluminium Layered Double Hydroxides Hierarchical Nanostructures

Layered double hydroxides (LDH) are a family of anionic clays consisting of alternating stacking of positively charged brucite-type metal hydroxide layers and negatively charged interlayer of counter-anions and water molecules. The positive charge of the brucite-type layer is due to partial isomorphous substitution of divalent metal cations by trivalent cations. The general structure of an LDH is shown in Figure 5.1 and can be defined by the general formula $[M^{II}_{1-x}M^{III}_{x}(OH)_2]^{x+}(A^{n-})_{x/n}.mH_2O$, where M^{II} and M^{III} are the di- and trivalent metal ions and A^{n-} is the counter-anion.[1] Since the naturally occurring mineral hydrotalcite (HT) $Mg_6Al_2(OH)_{16}CO_3.4H_2O$ belongs to this class of materials, LDH are also commonly known as HT-like materials. The nature of M^{II}, M^{III}, A^{n-} (e.g. Cl^-, SO_4^{2-}, CO_3^{2-}) and the value of the stoichiometric coefficient x can be tailored to modulate the properties of LDH for various applications.[2-5] The only limitation is that the ionic radii of M^{II} and M^{III} must not differ much from those of Mg^{2+} and Al^{3+}, respectively.[1] In the subsequent paragraphs, a particular LDH will be referred to using the short formula M(II)/M(III)-LDH.

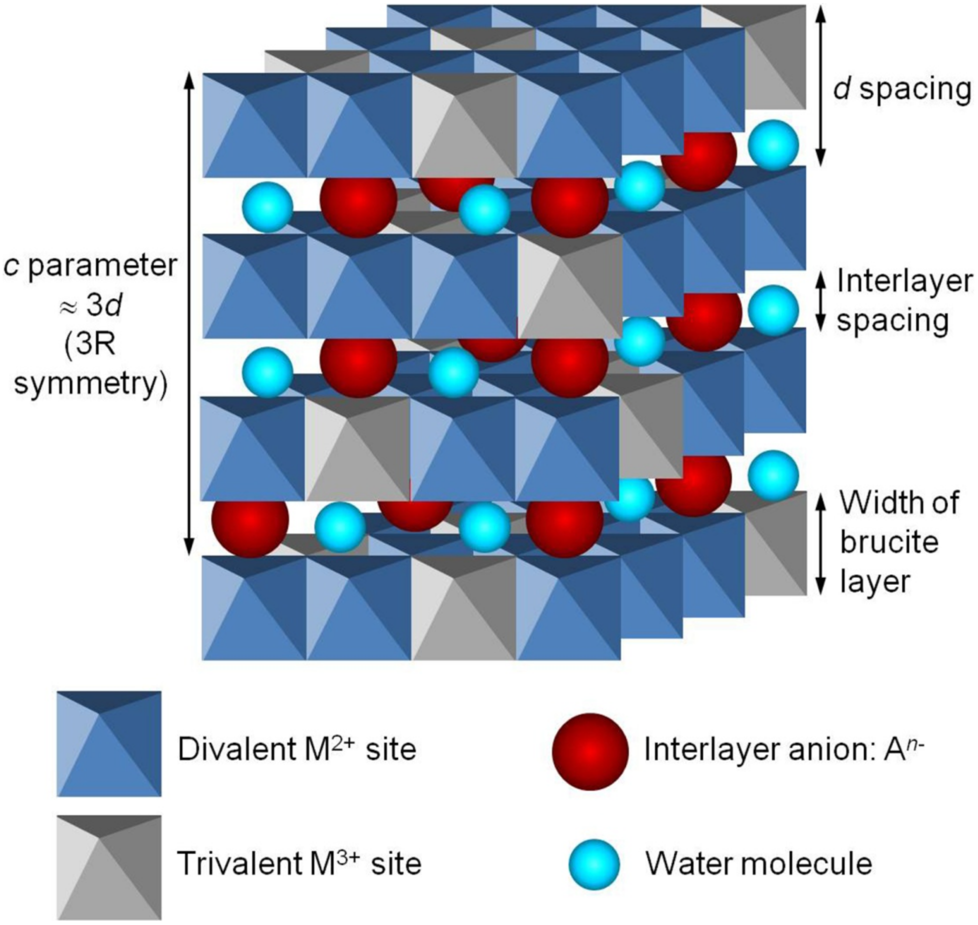

Figure 5.1: General structure of a layered double hydroxide (LDH), with several parameters as defined. [Schematics redrawn and adapted from Ref. 1, 6]

Co/Al-LDH, with Co^{2+} as the M^{II} ion and Al^{3+} the M^{III} ion, is among the most commonly studied LDH, popular for its excellent electrochemical properties.[5, 7-10] The Co metal centre is responsible for the redox reaction that gives the electrochemical properties of the material. The incorporation of Al^{3+} was found to enhance the electrochemical properties of Co/Al-LDH as compared to pure $Co(OH)_2$, as it enables the electrochemical oxidation of Co to higher oxidation state in a multi-electron process.[11, 12] According to Taube, octahedral Co(III) complexes are inert and inaccessible for rapid electron transfer due to their d^6 low-spin configuration.[13, 14] For Co/Al-LDH, the octahedral symmetry of the Co ligands in the hydroxide layer is deformed by the smaller and more highly charged Al^{3+} ion. In this way, the Co(III) obtained from oxidation of Co(II) can be further oxidized to higher oxidation state, i.e. Co(IV), resulting in an increase of specific energy in the high potential range (where Co(III)/Co(IV) redox would occur) in addition to that in the lower potential range (for Co(II)/Co(III) redox).[7, 15, 16] This is in contrast to that of pure $Co(OH)_2$, where only the latter is observed.[17, 18] Due to such improvement via the partial isomorphous substitution of Co^{2+} by Al^{3+}, Co/Al-LDH has gained importance in the development of electrochemical capacitors (ECs) and electrochemical sensors (ESs). We will briefly review each of these applications in the followings.

ECs are power devices that can complement or replace batteries in the energy storage field due to their fast charging time, high power delivery or uptake in shorter times, long cycle life, excellent safety and eco-friendly nature.[19, 20] There are two categories of ECs which operate on different mechanisms, namely, electric double-layer capacitors (EDLCs) and pseudocapacitors. EDLCs store electrical charge at the interface between the electrode and electrolyte. For pseudocapacitors, their capacitance arises from Faradaic redox reactions taking place at the electrode/electrolyte interface at an appropriate potential range. Comparing these two, pseudocapacitors generally exhibit larger capacitance, energy density and lower working voltage than EDLCs, since the Faradaic redox processes could occur both on surface and in the bulk near the surface of the solid electrode.[21-23] Ruthenium oxide (RuO_2) has been one of the most promising electrode materials for pseudocapacitors but it is too expensive for commercial use.[24] Recent development has found interests in using LDH as a cheaper alternative but with higher capacitive performance.[2, 5] With the enhanced electrochemical properties via the incorporation of Al^{3+} and the lower cost of Co,[25] Co/Al-LDH has good potential as a cost-effective electrode material for pseudocapacitor.[7, 8]

ESs are chemical sensors which give an electrical signal in response to chemical reaction between the analyte and the electrode. The signal obtained can arise from a change in current (amperometry), voltage (potentiometry) or resistance (conductometry). Majority of the studies were devoted to amperometric detection of glucose (Glc) that has great importance in the diagnosis and treatment of diabetes mellitus, as well as in monitoring and control of food processes. Various amperometric Glc sensors based on glucose oxidase (GOx) enzyme have been investigated.[26, 27] Despite the low detection limit, these enzymatic Glc sensors are often unstable due to the intrinsic nature of the enzyme.[28] This then leads to the increased attention towards the development of non-enzymatic sensors, which are more stable, simple, reproducible and free of oxygen limitation.[28, 29] Electrodes made up of noble metals and their alloys have been explored but they are too costly and prone to poisoning by chloride ions.

There is recently a growing trend of exploring LDH as a cheaper alternative for Glc sensors.[4, 5] LDH can either be used as host matrices to immobilize enzyme or directly as redox catalyst that mediates the electrooxidation of Glc.[4, 5] The latter is applicable as non-enzymatic Glc sensors and the LDH used often contain redox-active metal centres such as Ni(II) and Co(II),[5] which are responsible for their electrocatalytic behaviour in basic solution. There were only a few reports on the application of Co/Al-LDH for electrochemical Glc sensing. Initial reports showed that Co/Al-LDH is selective towards polyhydric compounds (e.g. glycerol, Glc and sucrose) in the presence of alcohols, thus it can be used as a complementary electrode to remove the signals from sugars for determination of ethanol in beer samples.[30, 31] Only recently, Co/Al-LDH was applied to amperometric and colorimetric detection of Glc in serum samples, but it was mainly focused on the latter.[9]

Nanotechnology is becoming increasingly important in the development for ECs and ESs applications. The high surface area of nanostructured materials such as nanoflakes (NFs), nanosheets (NSs) and nanowires (NWs) can offer more active sites, better utilization of materials and rapid transfer of electron and charge transport, all which can improve the performance of ECs and ESs.[28, 32-34] Hierarchical nanostructures, consisting of a combination of nanostructures, were recently shown to enhance electrode performance by further improving the surface area and also the efficiency of charge transport.[17, 35]

In this Chapter, we demonstrate a direct synthesis of hierarchical nanostructure of Co/Al-LDH NFs supported on Co NWs on conductive substrate. These arrays of nanostructures are ready for use without the need of binder, thus simplifying the electrode preparation process. Effect of various synthesis parameters and their electrochemical properties for pseudocapacitor and Glc sensing will be presented in Section 5.2 and Section 5.3, respectively.

5.1 Synthesis and characterizations of Co/Al-LDH hierarchical nanostructures

Hierarchical Co/Al-LDH nanostructures were synthesized according to details as described in Section 2.2.3. This simple procedure involves first electrodepositing Co NWs into the AAO nanochannels followed by NaOH alkaline treatment to remove the template and at the same time forming the LDH as NFs on the Co NWs surfaces. The length of the Co NWs grown within the AAO nanochannels can be readily controlled via electrodeposition duration. The working linear correlation is demonstrated in Figure 5.2 and, in this Chapter, Co NWs of about 5 μm prepared at 90 minutes were used throughout.

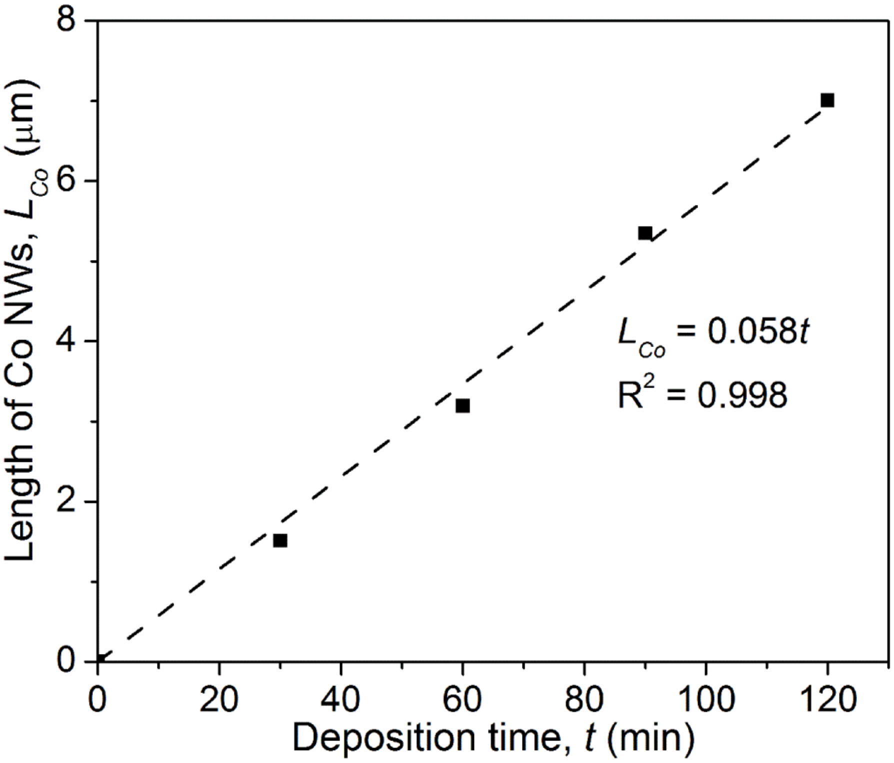

Figure 5.2: Average length of Co NWs obtained as a function of electrodeposition duration.

After the alkaline treatment in 2.5 M NaOH, some NFs were observed on both the top and sides of the Co NWs as shown in Figure 5.3. These NFs could arise due to the corrosion of Co NWs in the concentrated alkaline solution, leading to the precipitation of less soluble $Co(OH)_2$.[36] In the presence of Al^{3+} arising from the dissolution of AAO template, some Al^{3+} could isomorphously substitute Co^{2+} during the hydroxide formation to the final LDH NFs. Generally, it can be seen that more NFs were formed with longer alkaline treatment time, especially on top of the NWs array. Moreover, the NF crystals also became larger and the hexagonal shape became more defined for prolonged alkaline treatment as shown from the top views in the right panel of Figure 5.3.

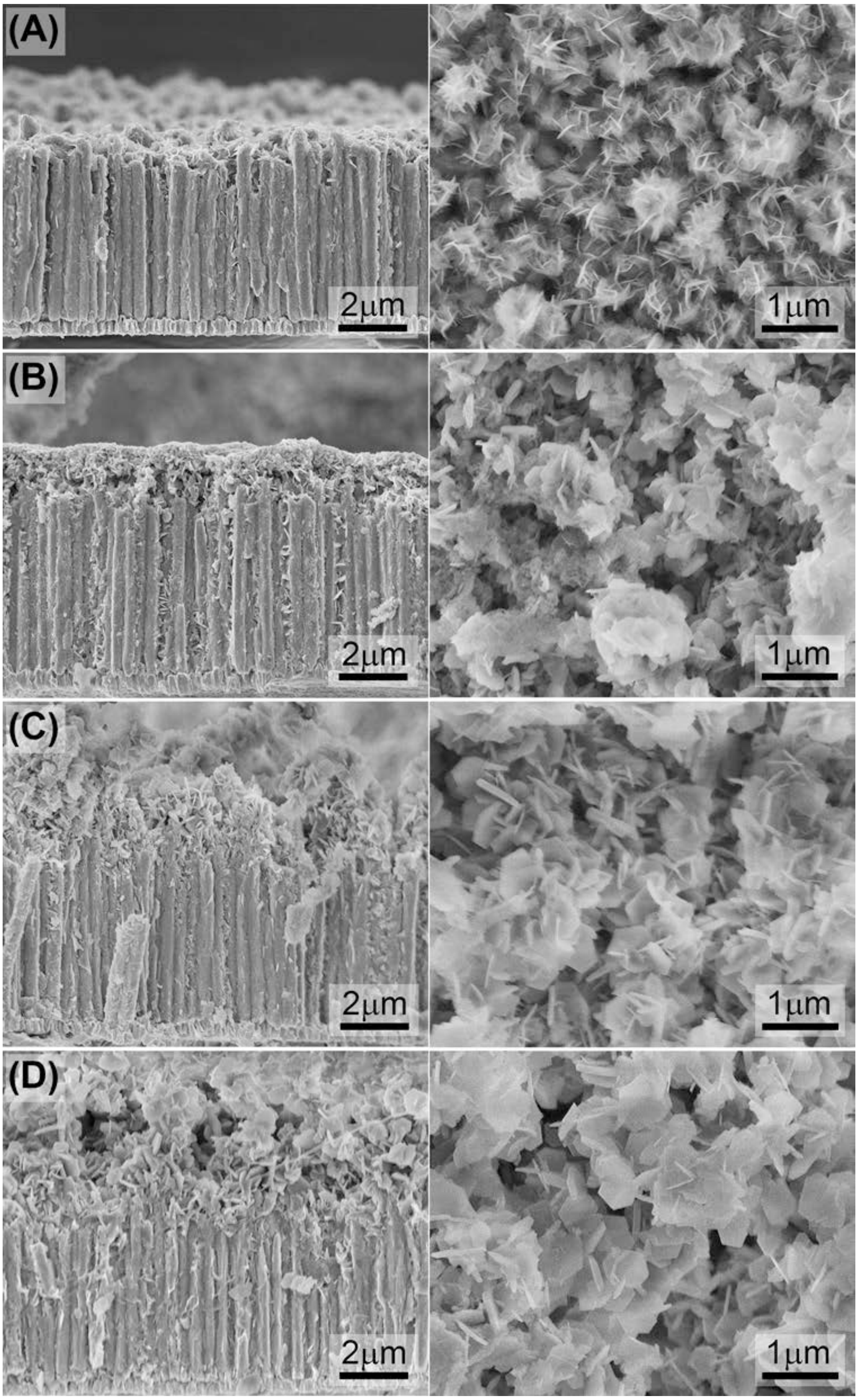

Figure 5.3: SEM images of Co/Al-LDH samples after alkaline treatment for (A) 1, (B) 18, (C) 24 and (D) 48 hours. The left and right panels show respectively the side and top views for each samples.

In comparison to the top layer, NFs on the sides of the NWs are much smaller in size and the hexagonal shapes less defined. The growth of larger crystals may be restricted on the sides due to the density of the NWs as the gap in between the NWs is less than 100 nm. Diffusion of NaOH to replenish the depleted OH^- ions would be much slower in these gaps than at the top of the NWs.

EDX analysis (Section 2.9.3) confirmed that the NFs contain Al and their content in atomic percentage ratio, i.e. x = Al / (Al + Co), are estimated as given in Table 5.1. The Al in the NFs has to originate from the Al^{3+} ions provided by the dissolution of the AAO template that is made up of amorphous amphoteric alumina, Al_2O_3. Etching by alkaline solution can be described by Equations 5.1 and 5.2:

$$2\ NaOH + Al_2O_3 \rightarrow 2\ NaAlO_2 + H_2O \quad (5.1)$$

$$NaAlO_2 + 2\ H_2O \rightarrow NaOH + Al(OH)_3 \quad (5.2)$$

With the presence of Al^{3+} ion in the alkaline solution, this ions can be doped into the lattice of cobalt hydroxide during the hydroxide formation. This is similar to the formation of HT-like Co/Al-LDH where some Co^{2+} are isomorphously substituted by Al^{3+} during the formation of cobalt hydroxide in the presence of both Co^{2+} and Al^{3+} ions in the alkaline solution.[8]

From Table 5.1, we found that the Al content increases with the duration of alkaline treatment but seems to reach a plateau after 24 hours of treatment. Longer duration of treatment allows time for more Al^{3+} to be integrated into the cobalt hydroxide, forming more Co/Al-LDH. The Al content in the NFs would reach a constant either because the amount of Al^{3+} was limited by the AAO template.

Table 5.1: Average atomic percentage obtained from EDX analyses of Co/Al-LDH samples for each alkaline treatment time.

Treatment time (hr)	**Co (at%)**	**Al (at%)**	**O (at%)**	**Al content, *x* [Al / (Al + Co)]**
1	93.04 ± 0.93	0.62 ± 0.14	6.34 ± 0.90	0.01 ± 0.01
18	72.69 ± 2.77	6.78 ± 1.03	20.54 ± 1.80	0.09 ± 0.02
24	68.55 ± 1.04	8.30 ± 0.26	23.15 ± 1.09	0.11 ± 0.01
48	60.90 ± 1.44	8.62 ± 0.29	30.47 ± 1.26	0.12 ± 0.01

The formation of Co/Al-LDH was verified using XRD (Section 2.9.9) and their diffraction patterns are given in Figure 5.4. Peaks characteristic of metallic Au, Co and Cu are observed and these arise from the Au substrate, Co NWs and Cu tape, respectively. Cu tape was used to hold the template to the sample holder for analysis. Other than that, the XRD patterns match well with characteristic peaks of $Co_6Al_2CO_3(OH)_{16}.4H_2O$ (JCPDS card no. 00-051-0045), indicating that our Co/Al-LDH nanostructures are isomorphous with the hydrotalcitic phase of the reference. These peaks, especially the (003) diffraction peak, became more intense at longer duration of alkaline treatment. The increasing XRD peak intensities and the

EDX Al content indicate that this LDH species is increasingly dominant on the surface of our samples as treatment time increases. By referencing to the standard XRD database, these samples may contain carbonate (CO_3^{2-}) as the interlayer anions in the LDH. This may be due to the presence of carbon dioxide (CO_2) gas in the solution during alkaline treatment.[1, 15]

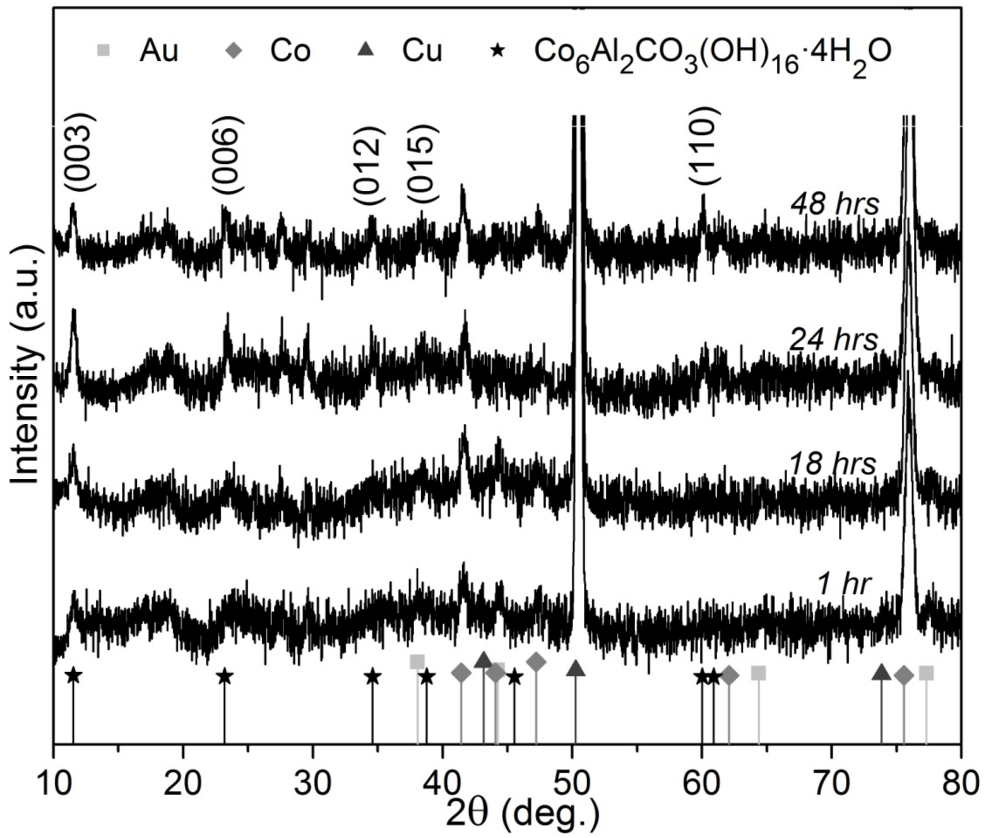

Figure 5.4: XRD pattern of Co/Al-LDH samples prepared at the specified alkaline treatment time. Characteristic peaks for Co/Al-LDH are as labelled. Reference peaks: Au (JCPDS 01-071-4614), Co (JCPDS 01-071-4652), Cu (JCPDS 01-071-4611) and $Co_6Al_2CO_3(OH)_{16}\cdot 4H_2O$ (JCPDS 00-051-0045).

In the following sections, we investigate the applications of these unique Co/AL-LDH NFs on Co NWs structures as pseudocapacitors and sensors. For ease of discussion, we will label these electrodes as Co/Al-NWNF-*y*, with *y* being the hours of alkaline treatment time during sample preparation. From Table 5.1 and the above discussion, it should be noted that the Al content, or the amount of Co/Al-LDH NFs, increases with *y* in these samples.

5.2 Electrochemical capacitance of Co/Al-LDH hierarchical nanostructures

The electrochemical behaviour of these Co/Al-NWNF nanostructures for application as EC was first studied via cyclic voltammetry (CV) and galvanostatic charge-discharge (C-D) measurements (Section 2.6). Typical CV curves scanned at 10 mV/s in 1 M KOH for samples prepared at various alkaline treatment time are shown in Figure 5.5. All the curves show two sets of redox peaks (labelled as I/I' and II/II') that are due to the Faradaic reactions as shown in Equation 5.3 and 5.4, respectively.[7]

$$Co(OH)_2 + OH^- \leftrightarrows CoOOH + H_2O + e^- \qquad (5.3)$$

$$CoOOH + OH^- \leftrightarrows CoO_2 + H_2O + e^- \qquad (5.4)$$

Initially when the sample was alkaline-treated for 1 hour (Co/Al-NWNF-1), the Faradaic current for redox I/I' at lower potential range (-0.05 V to 0.1 V) is larger than that for redox II/II' (0.2 V to 0.5 V). The CV profile for Co/Al-NWNF-18 shows a reversing trend, however, as the Faradaic current for redox II/II' begin to increases. The current for redox II/II' further increases while that for redox I/I’ decreases significantly for Co/Al-NWNF-24 and Co/Al-NWNF-48.

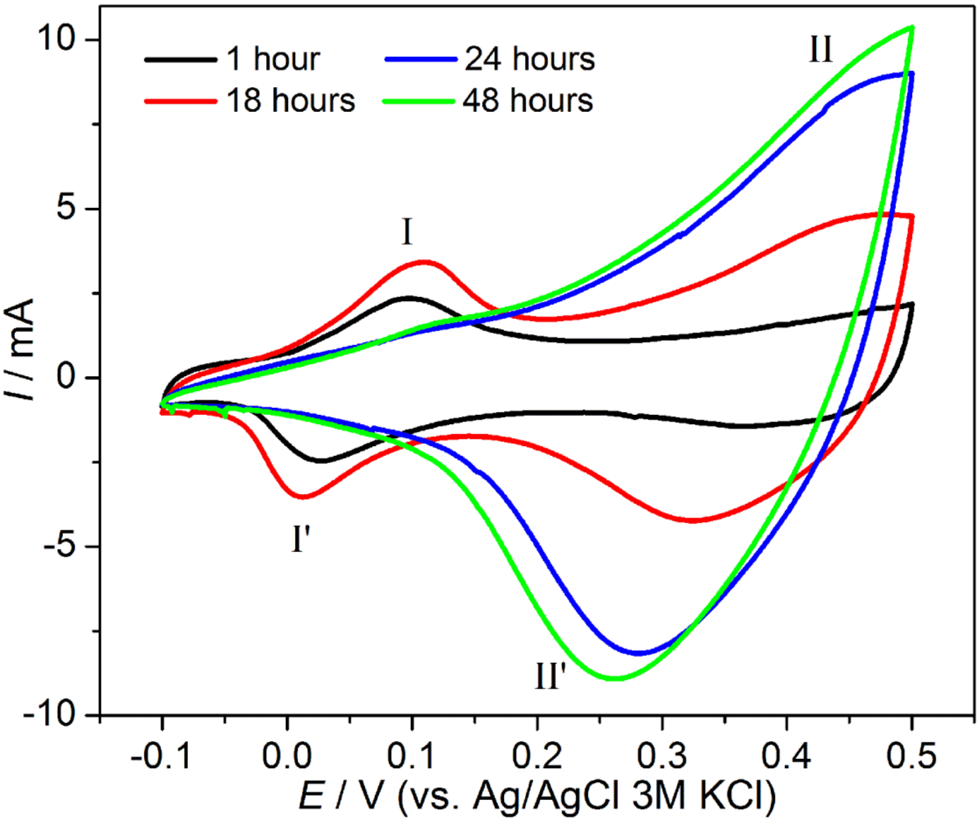

Figure 5.5: CV curves at scan rate of 10 mV/s for Co/Al-NWNF electrodes in 1 M KOH electrolyte. Samples prepared at varying alkaline treatment time are compared.

These CV curves suggest that Al content in the NFs has significant effect on the capacitance at high potential range. This observation is similar to that reported by Gupta et al. for their Al-substituted α-cobalt hydroxide nanosheet film.[7] As mentioned, the incorporation of Al^{3+} would distort the octahedral symmetry of Co ligands, enabling the supposedly inert Co(III) sites to be further oxidized to Co(IV). This thus increases the capacitance in the high potential range.[11, 12]

The respective charge-discharge (C-D) curves for the Co/Al-NWNF samples at 2.5 mA/cm^2 in 1M KOH are shown in Figure 5.6. All curves show the near symmetrical triangular shape, suggesting good supercapacitive behaviour. Similarly, it was observed that the capacitance at high potential range also increases with the increase in Al content.

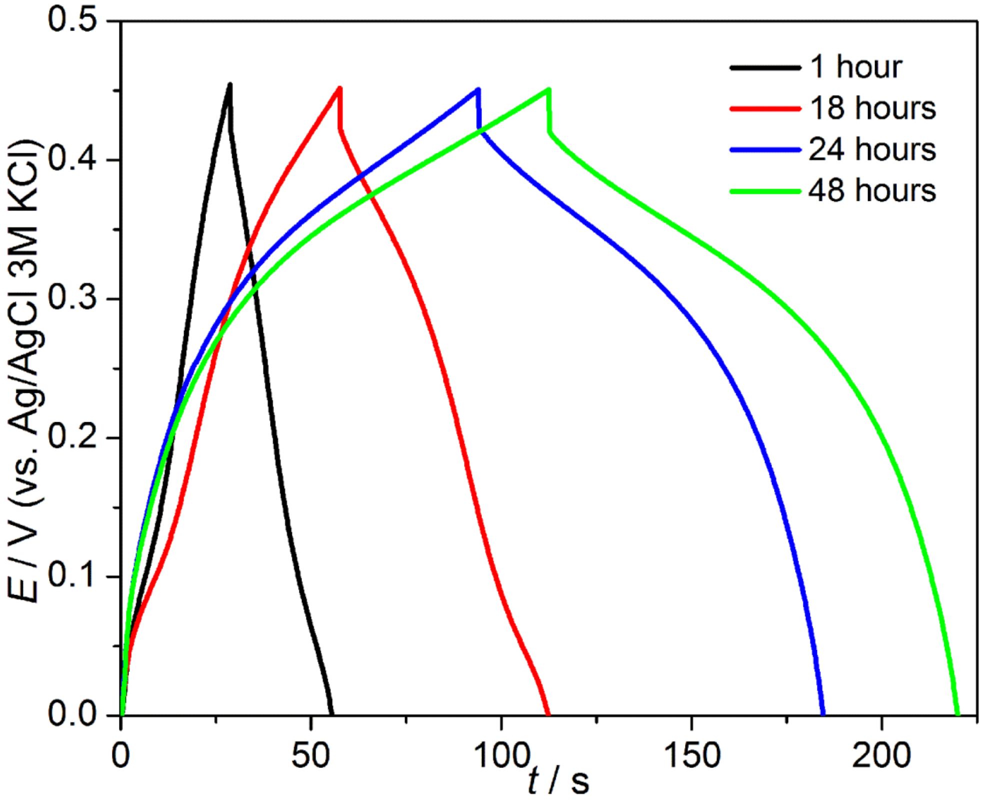

Figure 5.6: C-D curves at 2.5 mA/cm^2 current density for Co/Al-NWNF electrodes in 1 M KOH electrolyte. Samples prepared at varying alkaline treatment time are compared.

From these discharge curves, area-specific capacitance (C_a) can be calculated using Equation 5.5:

$$C_a = \frac{I_d \ \Delta t}{\Delta V} \tag{5.5}$$

where I_d (A/cm^2) is the discharge current density, Δt (s) is the discharge time and ΔV (V) is the discharge potential range. Thus, C_a for each Co/Al-NWNF electrode obtained at various current densities were calculated and plotted in Figure 5.7, together with their corresponding Al content. It is clearly seen from both plots that C_a and the Al content increase with the alkaline treatment time in the same way, indicating that the enhancement of capacitance is correlated to the formation of Co/Al-LDH NFs. The largest capacitance of 0.510 F/cm^2 is obtained from Co/Al-NWNF48, containing 12% Al, measured at current density of 2.5 mA/cm^2.

Based on Figure 5.7, all our Co/Al-NWNF electrodes were found to have similar high-rate capability compared to each other, preserving about 66% of the capacitance at 2.5 mA/cm^2 when the current density is increased to 12.7 mA/cm^2. One aspect that could affect the high-rate capability is the electrode resistance. It was reported for Co/Al-LDH film, however, that increasing Al content in would decrease the high-rate capability because the non-electroactive Al increases the internal resistance of the electrode.[8] Our samples are thus unique as the high-rate capability is unaffected by the Al content. We believe that in our case, the probable increase of resistance is offset by an improved electron transport due to the hierarchical geometry of Co/Al-LDH NFs supported on Co NWs grown on gold current collector.[17] The NWs allow a direct electron path from the NFs to the current collector and thus provide a facile electron path for charge transport, reducing the electrode resistance.

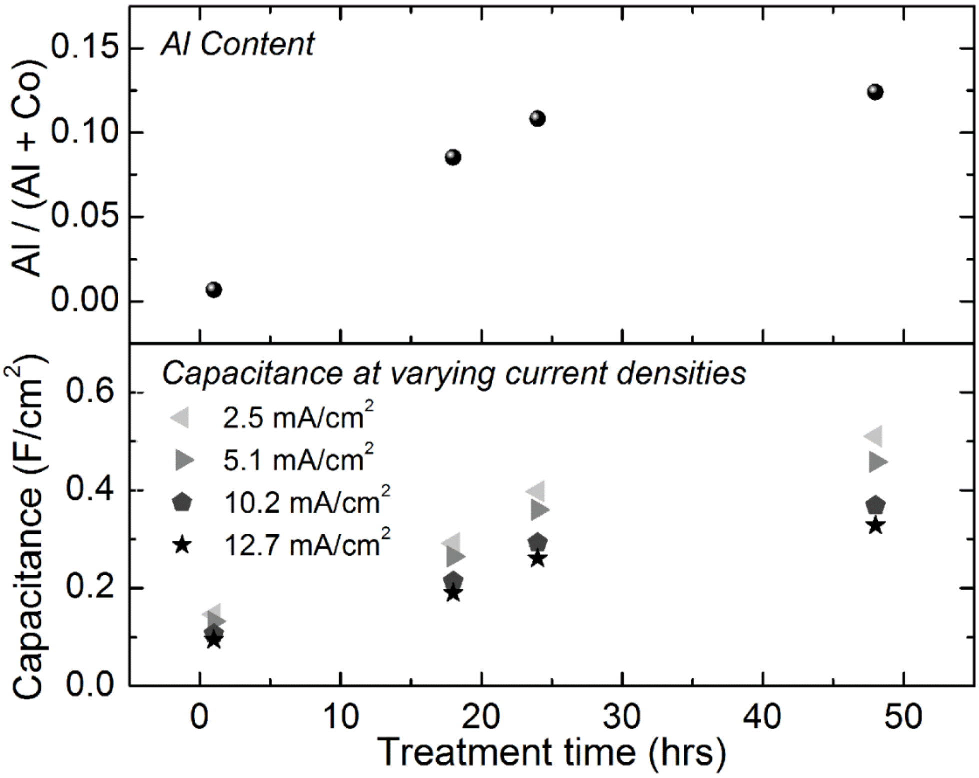

Figure 5.7: Correlation for Al content and area-specific capacitance at varying current densities against alkaline treatment time.

Coulombic efficiency or charge/discharge efficiency is the efficiency where charge is transferred or transported in a system. This can be estimated using the equation: $\eta = t_d/t_c$ x 100%, where t_d and t_c are the discharge and charge time in seconds, respectively. The coulombic efficiencies for all samples at each current density are thus calculated and plotted as shown in Figure 5.8. For the Co/Al-NWNF-48 sample, the efficiency dropped from 97% to 89% whereas for Co/Al-NWNF-1 sample, the value dropped from 97% to 74%. This shows that samples treated at longer duration (which contain high amount of Al) have better reversibility at large current density than those at shorter treatment time (which contain low amount of Al).

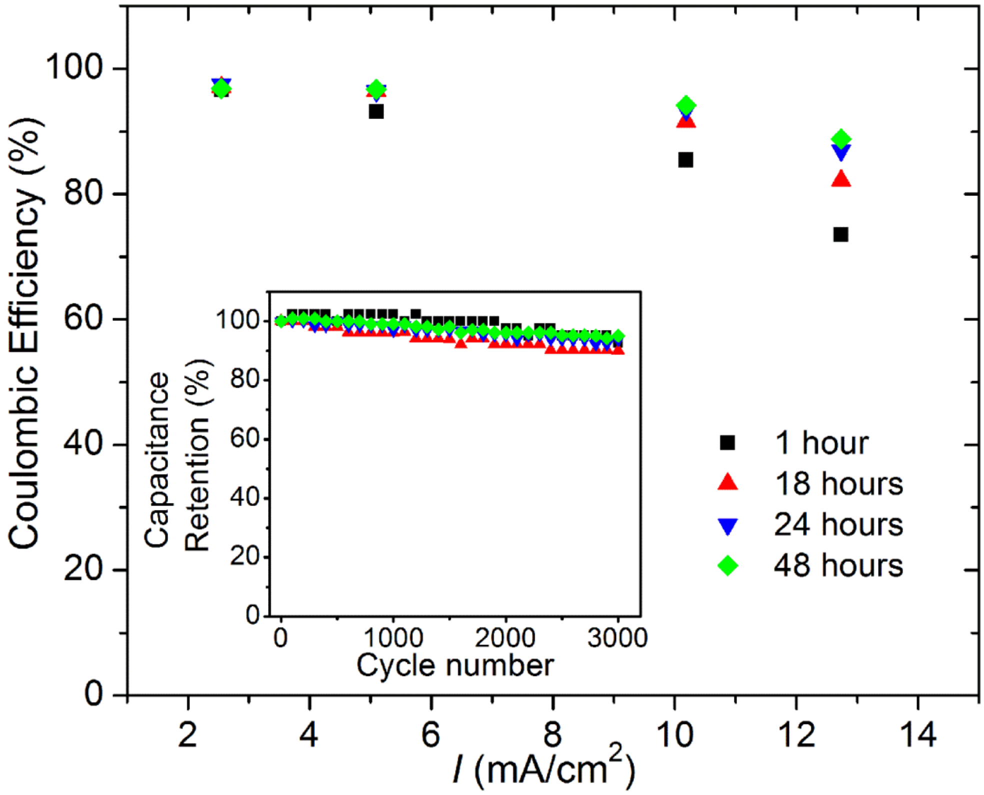

Figure 5.8: Coulombic efficiency against current density for samples at varying alkaline treatment time. Inset: cycle life data at 12.7 mA/cm^2.

The electrochemical stability of our Co/Al-NWNF samples was tested and the result is shown in the inset of Figure 5.8. All electrodes were subjected to 3000 continuous C-D cycles at 12.7 mA/cm^2 in 1 M KOH within potential range of 0 V to 0.45 V. Good cycling life was observed regardless of the alkaline treatment time or Al content in the NFs. After

3000 cycles, the capacitance was retained at more than 90% of their original capacitance, showing excellent electrochemical stability.

Numerous studies on using Co/Al-LDH as the electrode material for pseudocapacitor were reported since the last decade.[7, 8, 35, 37-40] EC performances of a few examples are tabulated in Table 5.2. However, fair comparison is extremely difficult among these literature studies since electrode performance is dependent on experimental conditions such as the type of electrolyte, electrolyte pH, electrode matrix and type of current collectors. Comparatively, our Co/Al-NWNF electrodes exhibit several merits such as large capacitance and good electrochemical stability.

Table 5.2: Examples of Co/Al-LDH-based electrodes reported in the literatures and their EC performances.

Electrode Material / Current Collector	**Method**	**C_m (F/g)**	**C_a (F/cm^2)**	**Rate capabi-lity**	**Cycle life (cycle no.)**	**Ref.**
Co/Al-NWNF-48 / Au	GS (2.5 mA/cm^2, 0-0.45V vs Ag/AgCl 3M KCl in 1M KOH)	-	0.510	66 %	92% (3000)	This study
$Co_{0.92}$-$Al_{0.08}$ LDH / SS	GS (1 A/g, 0-0.4V vs Ag/AgCl sat. KCl in 1M KOH)	843	0.176*	-	-	7
$Co_{0.75}$-$Al_{0.25}$ LDH / ITO	GS (1.3 A/g, 0-0.55V vs Hg/HgO in 6M KOH)	833	0.046*	-	95 % (2000)	8
Co/Al-LDH / Ni foam	GS (60 mA/g, -0.15-0.55V vs Hg/HgO in 6M KOH)	684	13.68*	-	80 % (1000)	38
Co/Al-LDH / Ni foam	GS (2 A/g, -0.1-0.5V vs SCE in 1M KOH + 0.1M $K_3Fe(CN)_6$)	712	-	-	67.0 % (200)	40
MnO_2-CoAl LDH / CFs	GS (1 A/g, -0.2-0.6V vs Hg/HgO in 1M LiOH)	944	1.153*	64.6 %	98.2% (6000)	35

* Values calculated based on details of setup as described in the literature.
SS: stainless steel, ITO: Indium-doped tin oxide, CFs: carbon fibers,
GS: Galvanostatic charge-discharge.

5.3 Electrochemical glucose sensing of Co/Al-LDH hierarchical nanostructures

Other than electrochemical capacitor, Co/Al-LDH was also studied for its electrocatalytic behaviour applicable as electrochemical sensor. In this Section, we investigated the electrocatalytic activity of Co/Al-NWNF-1 and Co/Al-NWNF-24 electrodes towards Glc oxidation for potential application as amperometric non-enzymatic Glc sensor.

Firstly, the electrocatalytic activity of the electrodes towards oxidation of Glc in alkaline solution was analyzed using CV (Section 2.7). CV curves of the two electrodes at scan rate of 10 mV/s in the absence and increasing amount of Glc in 0.1 M NaOH are shown in Figure 5.9A. In this electrolyte, both electrodes showed two redox couples (labelled as I/I’ and II/II’) that are related to the process Co(II)/Co(III) and Co(III)/Co(IV), which appear to be overlapping. This overlapping of peaks is similarly observed for the Co/Al-LDH films deposited on indium tin oxide (ITO) substrate by Scavetta *et al*.[9] Upon the addition of Glc, current increase at redox couple II/II’ is found to be higher than that at I/I’. This confirms that the electrooxidation of Glc in alkaline solution at our Co/Al-NWNF electrodes is mainly mediated by the Co(III)/Co(IV) redox couple, similar to other works on Co and Ni-based electrochemical Glc sensors.[9, 41, 42] The Co(III) centres can act as redox mediators for Glc oxidation according to the following equations and the mechanism is illustrated by the cartoon shown in Figure 5.9B:[9]

$$\text{Co(III)-LDH} + \text{OH}^- \leftrightarrows \text{Co(IV)-LDH(OH}^-) + e^- \quad (5.6)$$

$$\text{Co(IV)-LDH(OH}^-) + \text{Glc} \rightarrow \text{Co(III)-LDH} + \text{OH}^- + \text{gluconolactone} \quad (5.7)$$

Based on Equation 5.7, Co(IV) centres would be consumed and reduced to give more Co(III) in the presence of Glc. Reaction as shown in Equation 5.6 would be pushed forward, resulting in enhancement of anodic peak for II/II' redox as reflected in the CV curves in Figure 5.9A.

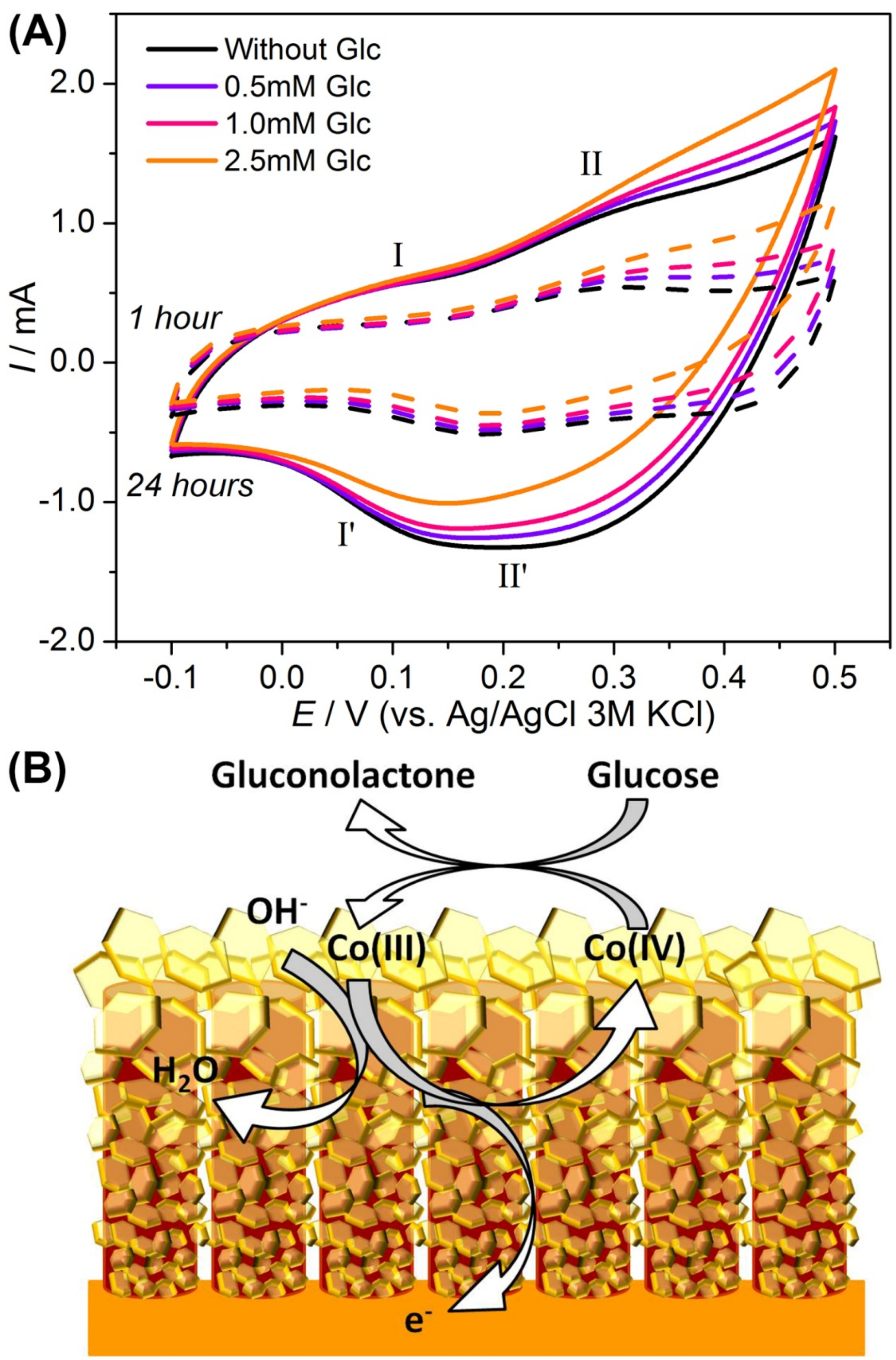

Figure 5.9: (A) CV curves at 10 mV/s in the absence and increasing amount of glucose (Glc) in 0.1 M NaOH solution. Dashed and solid lines are for Co/Al-NWNF-1 and Co/Al-NWNF-24 samples, respectively. (B) A cartoon showing the electrooxidation of glucose on Co/Al-LDH NFs grown on Co NWs.

Since the electrooxidation of Glc at both electrodes is more pronounced at region after 0.25 V, applied potentials of 0.3 V and 0.4 V were chosen to conduct the amperometric Glc sensing measurements (Section 2.7). Figure 5.10 shows rapid and stable current response upon the successive addition of Glc for both electrodes. As expected from observations derived from CV curves (Figure 5.9A), the increase of current upon addition of Glc is larger at 0.4 V than at 0.3 V. Comparing the two electrodes at the same applied potential, Co/Al-NWNF-24 gives rise to larger current response than that for Co/Al-NWNF-1. However, as the total Glc concentration in the electrolyte increases with further addition, the current responses gradually decrease. This is most probably due to higher tendency of the analyte and electrocatalytic reaction intermediates to adsorb onto the active sites of the electrode, thus hindering the catalytic activities and leads to a reduction in current response. Consequently, this would affect the linear range of the electrodes at each applied potential as will be discussed in the following paragraph.

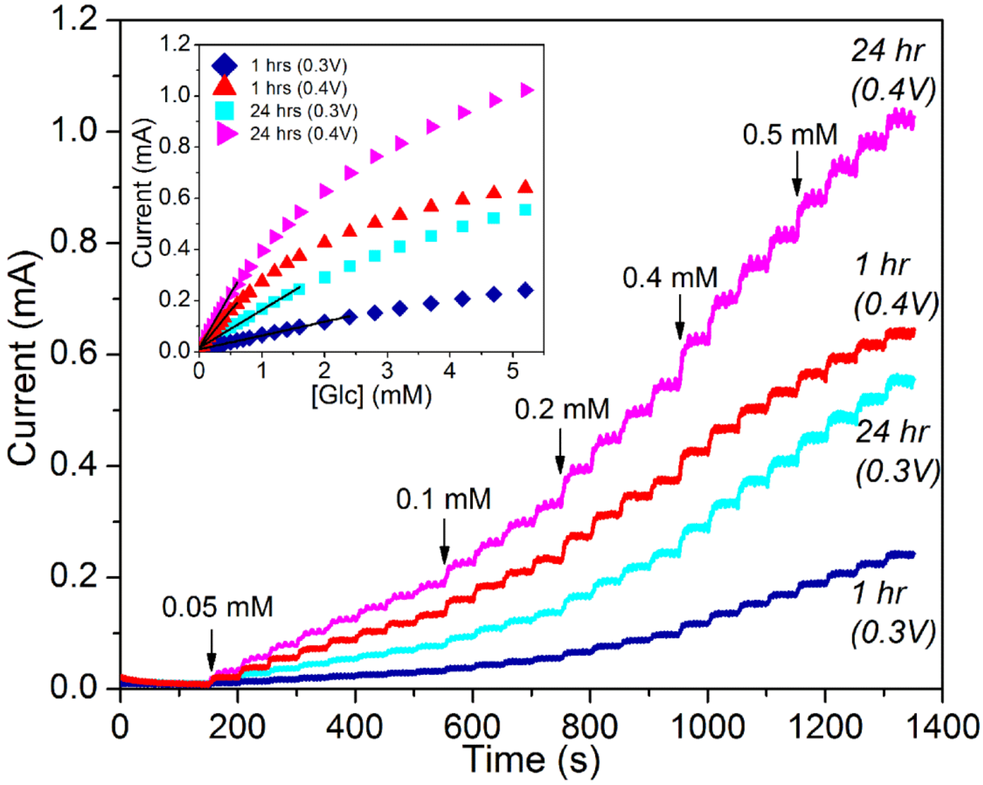

Figure 5.10: Amperometric response upon the successive addition of Glc in 0.1 M NaOH at the respective applied potential for Co/Al-NWNF-1 and Co/Al-NWNF-24. Inset: The corresponding calibration curves. [Note: The dilution effect has been taken into consideration for all concentration values indicated]

From the chronoamperograms, current vs. Glc concentration calibration plots are generated as shown in the inset of Figure 5.10. The corresponding linear range of these calibration plots are expanded more clearly in Figure 5.11. Equations for the linear regression of each calibration curve are given as indicated in the Figure. From the slopes of these curves, it is found that measurement at 0.4 V gives higher sensitivity than 0.3 V. Though more sensitive, measurement at 0.4 V resulted in smaller limit of linearity (LOL) (up to only 0.6 mM Glc) for both electrodes. At this larger applied potential, more Glc molecules would be oxidized and produce more intermediates, leading to the higher current response at each Glc addition (i.e. higher sensitivity). But, this would also cause the adsorption of analyte or intermediate molecules onto the active sites as mentioned in the preceding paragraph to occur at much lower concentration than when lower potential (0.3 V) was applied, resulting in the observed smaller LOL. Larger LOL is observed at 0.3 V up to 2.40 mM for Co/Al-NWNF-1 and 1.60 mM for Co/Al-NWNF-24 but at the expense of sensitivity dropping to 68.7 and 188.8 μAmM^{-1}cm^{-2}, respectively.

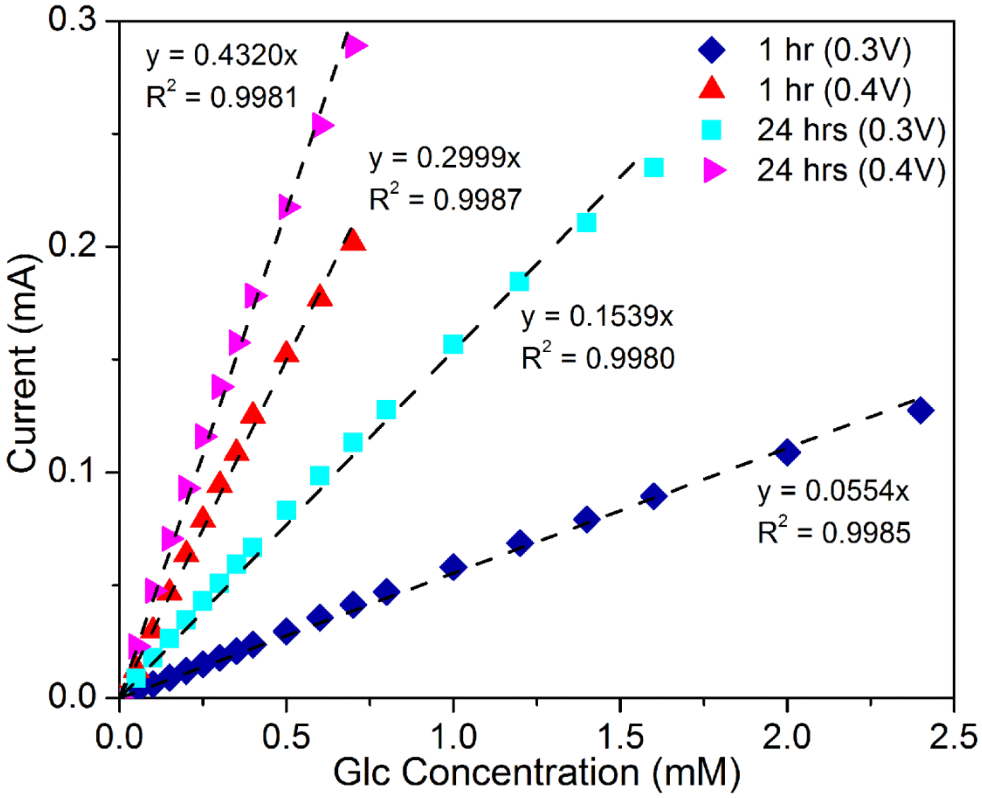

Figure 5.11: Expanded region of linear range from the calibration curve in the inset of Figure 5.10.

At each applied potential, Co/Al-NWNF-24 is always more sensitive to the detection of Glc than Co/Al-NWNF-1. This may be because the surface of Co/Al-NWNF-24 electrode consists of predominantly Co/Al-LDH species and NFs. Due to the layered structure of Co/Al-LDH, there is a large interlayer spacing in between the hydroxide layers.[1] At the chosen applied potential, Co(III) centres would be oxidized to Co(IV) as described by Equation 5.6 and OH^- ions would diffuse from the electrolyte to the surface of active material to ensure electroneutrality. With larger interlayer spacing, OH^- ions easily diffuse into the electrode surface of our Co/Al-NWNF electrodes. Thus. Equation 5.6 will shift to the right and more catalytic-active Co(IV) sites would be generated for the electrooxidation of Glc (Equation 5.7).

A comparison of the Glc sensing performance of our electrodes and some recently reported Co-based electrodes are tabulated in Table 5.3. Comparatively, our electrodes exhibit several merits such as high sensitivity even at low applied potential and relatively high LOL than most of the electrodes. The only one report that is also based on Co/Al-HT film[9] is comparatively less sensitive than our Co/Al-NWNF-24 electrode, even when their measurement was performed at higher applied potential. We would attribute the higher performance of our electrodes to the higher surface area arising from the hierarchical nanostructures designed.

Table 5.3: A comparison of non-enzymatic Glc sensing performance of Co-based electrodes in the literature.

Electrode materials	**E (V vs Ag/AgCl)**	**Sensitivity (μA mM^{-1}cm^{-2})**	**LOD^a (μM)**	**LOL^b (mM)**	**Resp. time (s)**	**Ref.**
Co/Al-NWNF-1 (0.1 M NaOH)	0.30	68.7	34.7	2.40	≤ 6^c	This study
	0.40	385.0	16.8	0.60		
Co/Al-NWNF-24 (0.1 M NaOH)	0.30	188.8	30.5	1.60		
	0.40	543.0	17.3	0.60		
Co/Al HT film (0.1 M NaOH)	0.50 (vs SCE)	424.0	2.0	1.50	-	[9]
Co_3O_4 NFs (0.1 M NaOH)	0.59	36.25	0.97	2.04	< 7	[42]
Co_3O_4 NRs (1.0 M NaOH)	0.50	571.8	0.058	3.50	-	[43]
CoOOH nanosheets (0.1 M NaOH)	0.40	341.0	30.9	0.70	< 4	[44]
	0.50	967.0	10.6	0.50		

[a] LOD = Limit of detection (S/N = 3); [b] LOL = Limit of linearity; [c] Response to 0.5 mM Glc

With OH$^-$ ions directly involved in Equation 5.6, concentration of NaOH (also pH of the electrolyte) would have an effect on the electrooxidation of Glc in Equation 5.7. As shown in Figure 5.12, it is obvious that the current response to a constant Glc concentration of 4 mM generally increases with the NaOH concentration and pH values. This dependency of electrocatalytic activity on the OH$^-$ ion concentration is similar to other reports on Co and Ni-based Glc sensors.[41, 43-45] As mentioned in the previous paragraph, OH$^-$ ions would have to diffuse from the electrolyte into the surface active material to ensure electroneutrality after the Co(III) centres in the hydroxide layers are oxidized to Co(IV). At higher OH^- concentration, more OH^- is available as counter ion. Equation 5.6 will shift to the right, generating more catalytic-active Co(IV) sites for electrooxidation of Glc and thus better sensitivity.

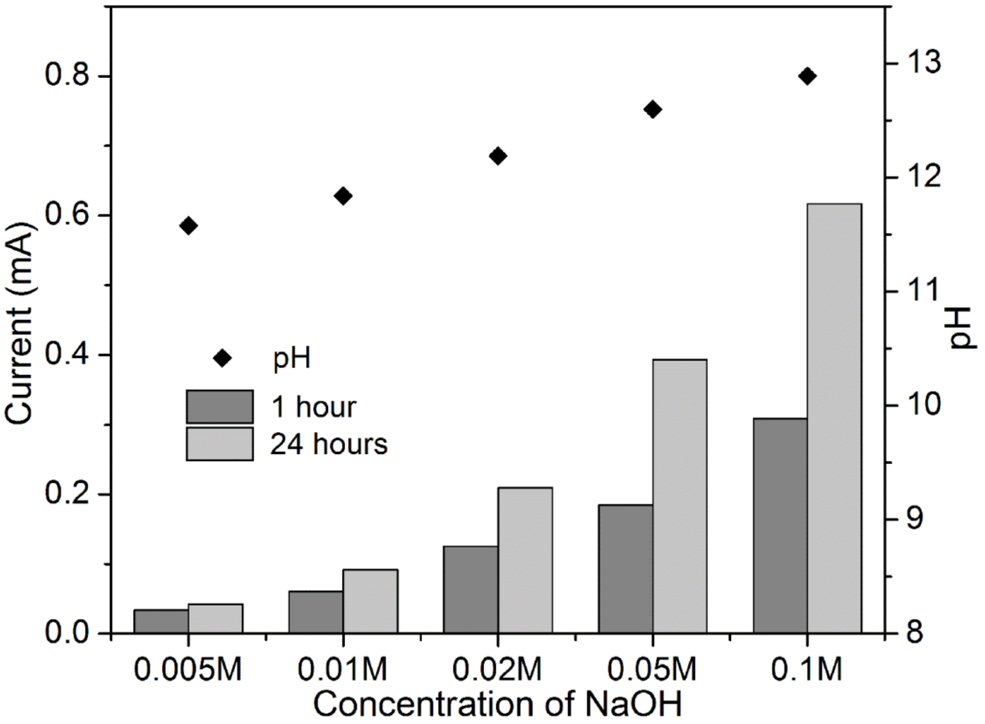

Figure 5.12: Amperometric response of Co/Al-NWNF electrodes to 4 mM Glc at 0.3 V in electrolytes of varying NaOH concentration and pH values.

Comparing the two electrodes, the increased sensitivity with NaOH concentration and pH of electrolyte was found to be more significant for Co/Al-NWNF-24. As mentioned in Section 5.1, the main difference between Co/Al-NWNF-1 and Co/Al-NWNF-24 is the nature of the dominant surface active material, presumably Co NWs and Co/Al-LDH

NFs for respective electrodes. At the same NaOH concentration, OH^- ions would diffuse more easily into the interlayer of Co/Al-LDH than for Co due to the larger spacing of the interlayer.[1, 46] Hence, the electrode surface of Co/Al-NWNF-24 is activated to larger extent, leading to much higher sensitivity towards Glc.

Since the current response arises due to Equation 5.7, any compounds other than Glc that can be oxidized would interfere with the measurement. In view of their potential applications as Glc sensor for blood/serum samples, the selectivity of our electrodes were tested against naturally occurring interfering compounds such as uric acid (UA) and ascorbic acid (AA). The tests were carried out at 0.3 V to measure 4 mM Glc against 0.33 mM of UA and 0.125 mM of AA. These concentrations are similar to that of normal physiological levels.[47, 48] As shown in Figure 5.13, Co/Al-NWNF-24 demonstrates better selectivity against UA and AA than Co/Al-NWNF-1. The presence of UA and AA in the electrolyte with 4 mM Glc resulted in only 3% and 4% increase of current response for Co/Al-NWNF-24 but for Co/Al-NWNF-1, the increase was 30% and 13%, respectively.

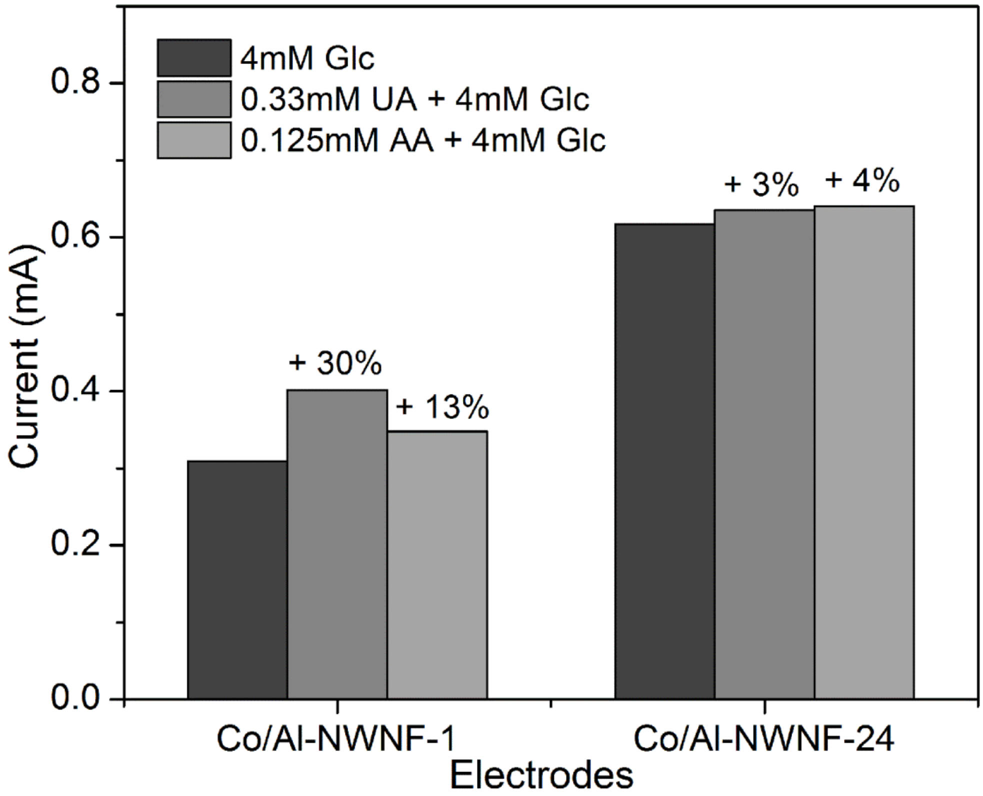

Figure 5.13: Amperometric response of Co/Al-NWNF electrodes to 4 mM Glc at 0.3 V in the presence of interfering compounds (UA: uric acid, AA: ascorbic acid) in 0.1 M NaOH electrolyte.

The selectivity towards Glc against UA and AA at our Co/Al-NWNF electrodes may arise from the repelling effect as described by Ding et al.[42] Since both Co/Al-NWNF electrodes in nature are hydroxides in the alkaline electrolyte and their isoelectric points (IEP) occur at about pH 9.8 - 10.8,[49-51] their surfaces should be negatively charged in the 0.1 M NaOH electrolyte (pH 12.9) used here. This negatively charged surface would then repel UA and AA which are also negatively charged in the alkaline environment due to the loss of proton. Based on such hypothesis, both Co/Al-NWNF-1 and Co/Al-NWNF-24 should have similar selectivity towards Glc. Instead, the Co/Al-NWNF-24 was observed to have better selectivity. This may be due to higher Al content integrated in Co/Al-NWNF-24 electrode which may further enhance the negative charge of the electrode surface as the IEP for Al occurs at pH 5.4,[52] leading to larger repelling effect against UA and AA. This demonstrates the potential of Co/Al-NWNF-24 as a sensitive and selective non-enzymatic sensor for Glc detection in blood/serum samples.

The reproducibility and stability of both electrodes were also investigated. All measurements were carried out at 0.3 V in 0.1 M NaOH. Both Co/Al-NWNF-1 and Co/Al-NWNF-24 electrodes showed good intra-electrode reproducibility from five repeated measurements of 0.4 mM Glc (n = 5) with relative standard deviation (RSD) of 2.0% and 2.9%, respectively. However, the inter-electrode reproducibility in response to 0.4 mM Glc for three electrodes prepared at same synthesis conditions (n = 3) is only satisfactory. Considerably low RSD of 14.7% and 18.2% were observed for Co/Al-NWNF-1 and Co/Al-NWNF-24, respectively. Both electrodes were found to have good stability. After 13 days of storage in ambient condition, current responses for 0.4 mM Glc at Co/Al-NWNF-1 and Co/Al-NWNF-24 electrodes were found to preserve 96% and 94% of their initial responses, respectively.

5.4 Summary

Hierarchical nanostructure of Co/Al-LDH NFs supported on Co NWs was successfully fabricated through an alkaline treatment of Co NWs embedded in AAO at ambient condition. These nanostructures were grown on current collector, thus can be used directly as electrode without the need of binder and tedious electrode preparation procedures such as dispersion, sonication, drop-casting and drying. The content of Al in NFs was found to increase with the duration of alkaline treatment and the crystal structure matched well with HT-like $Co_6Al_2CO_3(OH)_{16}.4H_2O$.

The electrochemical capacitor properties of these Co/Al-LDH nanostructured electrodes were found to improve with higher Al content and when Co/Al-LDH is the dominant species on the electrode surface. In addition to high capacitance value, these electrodes also show good rate capability and coulombic efficiency, and excellent electrochemical stability.

For the application in non-enzymatic Glc sensor, our nanostructured electrodes exhibited high sensitivity and low detection limit, with the highest value of 543.0 $\mu AmM^{-1}cm^{-2}$ achieved at applied potential of 0.40 V. These electrodes also exhibited good selectivity towards Glc in the presence of uric acid and ascorbic acid, making this electrode a potential sensitive and selective non-enzymatic sensor for Glc detection in blood/serum samples.

5.5 References

1. F. Cavani, F. Trifiro, A. Vaccari. *Catal. Today* **11** (1991) 173-301.
2. X. X. Guo, F. Z. Zhang, D. G. Evans, X. Duan. *Chem. Commun.* **46** (2010) 5197-5210.
3. H. Abdolmohammad-Zadeh, Z. Rezvani, G. H. Sadeghi, E. Zorufi. *Anal. Chim. Acta* **685** (2011) 212-219.

4. D. Tonelli, E. Scavetta, M. Giorgetti. *Anal. Bioanal. Chem.* **405** (2013) 603-614.

5. C. Mousty, F. Leroux. *Recent Patents on Nanotechnology* **6** (2012) 174-192.

6. V. Rives, M. A. Ulibarri. *Coord. Chem. Rev.* **181** (1999) 61-120.

7. V. Gupta, S. Gupta, N. Miura. *J. Power Sources* **177** (2008) 685-689.

8. Y. Wang, W. Yang, C. Chen, D. G. Evans. *J. Power Sources* **184** (2008) 682-690.

9. E. Scavetta, B. Ballarin, D. Tonelli. *Electroanalysis* **22** (2010) 427-432.

10. I. Gualandi, A. G. Solito, E. Scavetta, D. Tonelli. *Electroanalysis* **24** (2012) 857-864.

11. D. H. Buss, J. Bauer, W. Diembeck, O. Glemser. *J. Chem. Soc., Chem. Commun.* (1985) 81-82.

12. J. Bauer, D. H. Buss, H. J. Harms, O. Glemser. *J. Electrochem. Soc.* **137** (1990) 173-178.

13. H. Taube. *Adv. Inorg. Chem.* **1** (1959) 1-53.

14. L. E. Orgel. *An Introduction to Transition-Metal Chemistry: Ligand-Field Theory*. 2nd ed., Methuen & Co. Ltd., London (1966) pp. 107-116.

15. E. Scavetta, B. Ballarin, M. Gazzano, D. Tonelli. *Electrochim. Acta* **54** (2009) 1027-1033.

16. E. Scavetta, B. Ballarin, C. Corticelli, I. Gualandi, D. Tonelli, V. Prevot, C. Forano, C. Mousty. *J. Power Sources* **201** (2012) 360-367.

17. C. Y. Yan, H. Jiang, T. Zhao, C. Z. Li, J. Ma, P. S. Lee. *J. Mater. Chem.* **21** (2011) 10482-10488.

18. L. R. Hou, C. Z. Yuan, L. Yang, L. F. Shen, F. Zhang, X. G. Zhang. *Crystengcomm* **13** (2011) 6130-6135.

19. J. R. Miller, P. Simon. *Science* **321** (2008) 651-652.

20. B. E. Conway. *Electrochemical Supercapacitors: Scientific Fundamentals and Technological Application*. Plenum Press, New York (1999).

21. Y. Zhang, H. Feng, X. B. Wu, L. Z. Wang, A. Q. Zhang, T. C. Xia, H. C. Dong, X. F. Li, L. S. Zhang. *Int. J. Hydrogen Energy* **34** (2009) 4889-4899.

22. B. E. Conway, V. Birss, J. Wojtowicz. *J. Power Sources* **66** (1997) 1-14.

23. G. P. Wang, L. Zhang, J. J. Zhang. *Chem. Soc. Rev.* **41** (2012) 797-828.

24. H. Lee, M. S. Cho, I. H. Kim, J. D. Nam, Y. Lee. *Synth. Met.* **160** (2010) 1055-1059.

25. P. C. K. Vesborg, T. F. Jaramillo. *RSC Adv.* **2** (2012) 7933-7947.

26. B. J. Plowman, S. K. Bhargava, A. P. O'Mullane. *Analyst* **136** (2011) 5107-5119.

27. D. W. Kimmel, G. LeBlanc, M. E. Meschievitz, D. E. Cliffel. *Anal. Chem.* **84** (2012) 685-707.

28. P. Si, Y. J. Huang, T. H. Wang, J. M. Ma. *RSC Adv.* **3** (2013) 3487-3502.

29. G. F. Wang, X. P. He, L. L. Wang, A. X. Gu, Y. Huang, B. Fang, B. Y. Geng, X. J. Zhang. *Microchimica Acta* **180** (2013) 161-186.

30. E. Scavetta, D. Tonelli. *Electroanalysis* **17** (2005) 363-370.

31. E. Scavetta, B. Ballarin, M. Berrettoni, I. Carpani, M. Giorgetti, D. Tonelli. *Electrochim. Acta* **51** (2006) 2129-2134.

32. A. S. Arico, P. Bruce, B. Scrosati, J. M. Tarascon, W. Van Schalkwijk. *Nat. Mater.* **4** (2005) 366-377.

33. J. Huang, T. Lei, X. Wei, X. Liu, T. Liu, D. Cao, J. Yin, G. Wang. *J. Power Sources* **232** (2013) 370-375.

34. Q. F. Wang, X. F. Wang, B. Liu, G. Yu, X. J. Hou, D. Chen, G. Z. Shen. *J. Mater. Chem. A* **1** (2013) 2468-2473.

35. J. W. Zhao, Z. Z. Lu, M. F. Shao, D. P. Yan, M. Wei, D. G. Evans, X. Duan. *RSC Adv.* **3** (2013) 1045-1049.

36. A. Groysman. *Corrosion for Everybody*. Springer, (2010).

37. L.-H. Su, X.-G. Zhang. *J. Power Sources* **172** (2007) 999-1006.

38. Y. Wang, W. Yang, S. Zhang, D. G. Evans, X. Duan. *J. Electrochem. Soc.* **152** (2005) A2130-A2137.

39. L. H. Su, X. G. Zhang, C. H. Mi, Y. Liu. *J. Power Sources* **179** (2008) 388-394.

40. L. H. Su, X. G. Zhang, C. H. Mi, B. Gao, Y. Liu. *Physical Chemistry Chemical Physics : PCCP* **11** (2009) 2195-2202.

41. L. Q. Luo, F. Li, L. M. Zhu, Y. P. Ding, Z. Zhang, D. M. Deng, B. Lu. *Colloids and Surfaces B: Biointerfaces* **102** (2013) 307-311.

42. Y. Ding, Y. Wang, L. A. Su, M. Bellagamba, H. Zhang, Y. Lei. *Biosens. Bioelectron.* **26** (2010) 542-548.

43. C. W. Kung, C. Y. Lin, Y. H. Lai, R. Vittal, K. C. Ho. *Biosens. Bioelectron.* **27** (2011) 125-131.

44. K. K. Lee, P. Y. Loh, C. H. Sow, W. S. Chin. *Electrochem. Commun.* **20** (2012) 128-132.

45. J. Yang, W. D. Zhang, S. Gunasekaran. *Electrochim. Acta* **56** (2011) 5538-5544.

46. A. W. Hull. *Phys. Rev.* **17** (1921) 571-588.

47. S. Park, H. Boo, T. D. Chung. *Anal. Chim. Acta* **556** (2006) 46-57.

48. S. Hrapovic, J. H. T. Luong. *Anal. Chem.* **75** (2003) 3308-3315.

49. Z. Z. Xu, Z. L. Chen, C. Joll, Y. Ben, J. M. Shen, H. Tao. *Catal. Commun.* **10** (2009) 1221-1225.

50. K. Jurkiewicz. *Int. J. Miner. Process.* **17** (1986) 67-81.

51. G. A. Parks. *Chem. Rev.* **65** (1965) 177-198.

52. G. Lefevre, L. Cerovic, S. Milonjic, M. Fedoroff, J. Finne, A. Jaubertie. *J. Colloid Interface Sci.* **337** (2009) 449-455.

Chapter 6

Synthesis and Photocurrent Study of Aligned MWCNT/PPV Core-shell Nanowires

The discovery of carbon nanotubes (CNT)[1] have sparked new research interests towards 1D nanostructures. CNT has high surface area and high electrical conductivity, as well as unique thermal and mechanical properties.[2-6] Since then, composites of CNT with various polymers began to sprout in order to attain synergistic effects of the combined materials, mostly aimed at exploiting the unique mechanical properties of CNT.[7] Subsequently, interests in their electronic properties began to grow with the development of conjugated polymers (CPs) that exhibit unique electronic and optical properties.[8-10] Combination of these two materials are promising for electronic and optoelectronic devices where improvement such as higher electrical conductivity, electroluminescence efficiency and photoconduction have been observed.[11-16] These were attributed to the ability of CNT in providing direct pathways for charge transport, which enhanced conductivity and electroluminescence, and for separation of excitons, which improved photoconductivity.

The CNT/CP composites can be in the form of (1) films where loose strands of CNT are mixed within CP matrices,[11-14] (2) compact membranes consisted of individual CNT/CP core-shell NWs[15,17] and (3) free-standing arrays of perpendicularly aligned CNT/CP core-shell NWs on substrates.[16, [18, 19] Each of these has their disadvantages but all showed improvement of properties compared to individual components. Nevertheless, those in the form of core-shells were found to give additional advantage of higher surface area. With the CP wrapping around each strands of CNT, the CNT not only act as support that increases surface area of CP but also provide direct pathways for charge transport.[15-19] Besides, these CNT/CP core-shell NWs can be grown on or transferred onto a conductive substrate, thus the resulting product can be directly used as electrode without the need for binder and this thus simplifies the electrode preparation process.

Much effort had been dedicated to explore simple synthesis method to fabricate CNT/CP core-shell NWs such as surfactant-directed[20, 21] and ultrasonic-assisted[15, 22] in-situ polymerization, water/oil microemulsion[23] and electrochemical polymerization.[16-19] Among these methods, electrochemical polymerization may be the easiest with more control over the polymer shell thickness via the adjustment of electrodeposition parameters. Besides, this is one of the most commonly used methods for deposition of CP shells onto arrays of “aligned” CNT.[16, 18, 19]

Poly(*p*-phenylene vinylene) (PPV), which was studied in Chapter 3, is one of the CP that is popular for its optical and optoelectronic properties. Composites of CNT with PPV were explored, mostly based on films where loose strands of CNT are mixed within the PPV matrix.[11, 12] The closest form of CNT/PPV core-shell nanostructures are that reported by Kim *et al*.[24] and Massuyeau *et al*.[25] The former was in the form of bilayer NTs consisting of PPV inner layer and carbonized-PPV outer layer. No CNT was involved but they reported that the carbonized-PPV exhibits similar electrical conductivity properties. For the latter, many strands of single-walled CNT were embedded in each strand of PPV NWs within the nanochannels of AAO.

In this Chapter, we aimed to study composite of PPV with free-standing arrays of aligned multi-walled CNT (MWCNT) in the form of coaxial MWCNT/PPV core-shell NWs. Hence, array of perpendicularly aligned MWCNT produced by plasma-enhanced chemical vapour deposition (PECVD) is used as template for PPV to deposit onto as the shell. Preparation conditions for the electrodeposition of PPV shell are adapted from those established in Chapter 3. Current-voltage (*I*-*V*) behaviour and photocurrent (PC) response of these arrays of MWCNT/PPV core-shell NWs will be studied and compared to that for MWCNT arrays.

6.1 Synthesis and characterizations of aligned MWCNT/PPV core-shell nanowires

The free-standing arrays of aligned MWCNT and MWCNT/PPV core-shell NWs were synthesized following details given in Section 2.3. Shown in Figure 6.1 are the representative SEM images of the as-grown aligned MWCNT arrays on *n*-type Si substrate. Although the strands of MWCNT are not standing straight in rigid form, it was generally grown upward perpendicularly from the substrate. The average diameter of the MWCNT obtained is 21 ± 6 nm.

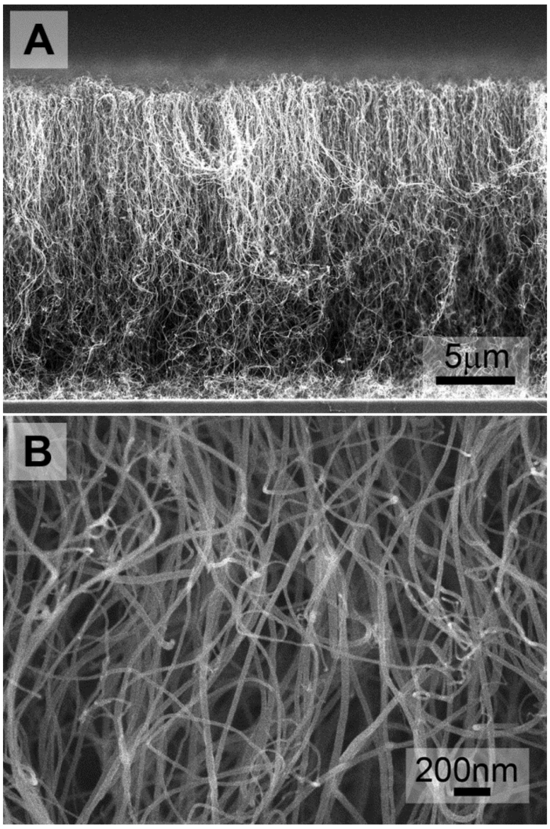

Figure 6.1: (A) Low and (B) high magnification of side view SEM images of aligned MWCNT arrays as-grown via PECVD.

As a start, electrodeposition of PPV onto the MWCNT was carried out at constant potential of -2.34 V, which was the optimized parameter used in Chapter 3. As shown in Figure 6.2, a thick layer of PPV was formed on top of the MWCNT array. On the other hand, the diameters of the MWCNT remained small indicating that PPV was not successfully deposited as the shell. The problem may arise from the rapid and continuous reduction of TBX precursor to form PPV at the electrode-electrolyte interface when constant potential was applied. Besides, "point effect" may have occurred where deposition occurs faster at the tips of MWCNT and block the diffusion of precursor into the array, preventing deposition of PPV along the sides of MWCNT.

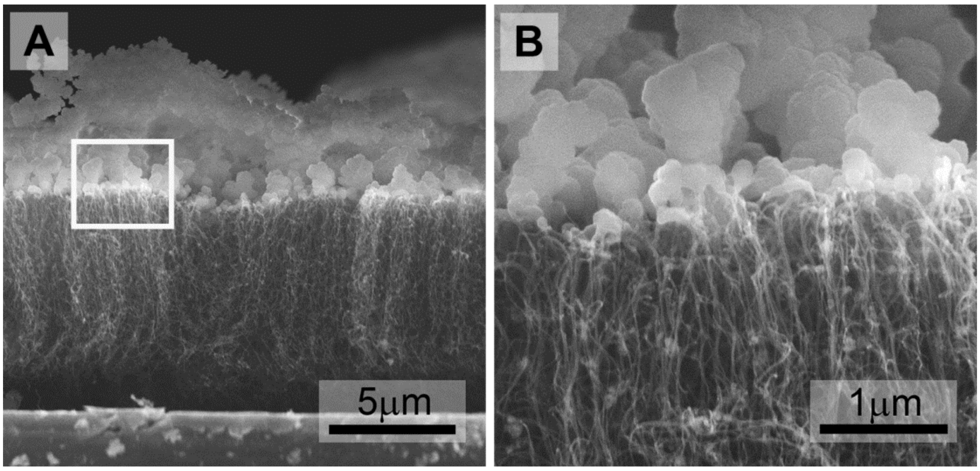

Figure 6.2: SEM images of MWCNT/PPV obtained via electrodeposition at constant potential of -2.34 V for total charge of 0.5 C at (A) low and (B) high magnification. The white box in (A) indicates area where image (B) was obtained.

For better control of the deposition of PPV around the MWCNT and its thickness, pulse potentiometry was explored. In principle, this technique enables slow "layer-by-layer" deposition, and can result in more controlled growth than constant potential.[26, 27] There was no specific rule for the best pulse parameters[28] and Figure 6.3 illustrates one cycle of the square-wave pulsed-potential sequence optimized for the deposition of PPV shell. This pulse sequence is repeated many cycles for a specific duration in order to obtain certain amount of PPV deposited. As shown in the pulse profile, deposition would occur at the strong negative pulse of deposition potential (E_{dep}) during t_{on} and punctuated by a positive pulse for duration $t_{off,}$ followed by a long rest (E = 0 V) for t_r. The positive pulse is to ensure no further reduction process and the resting time (t_r) allows restoration of the depleted starting material on the electrode surface before the next pulse is applied. The E_{dep} applied here is more cathodic than that used in Chapter 3 in order to push the electropolymerization to occur during the short pulses. This is similar to many other reports on using pulsed technique for electrodeposition.[26, 27]

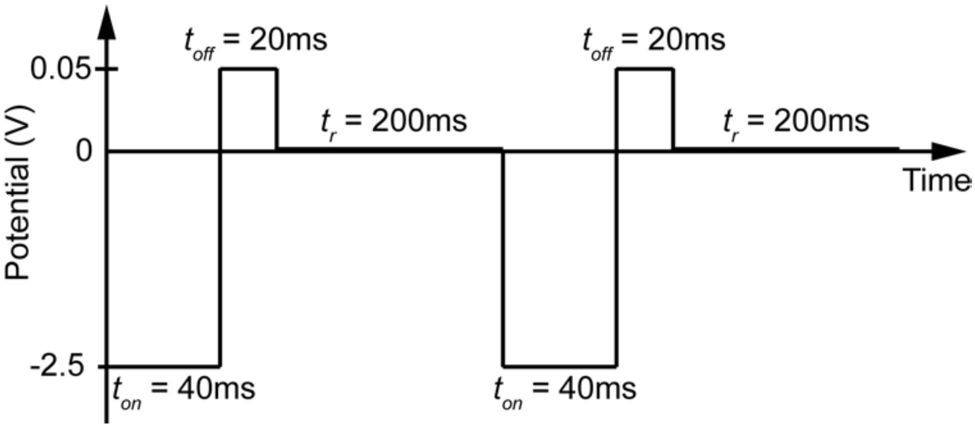

Figure 6.3: Profile of pulse potential used to electrodeposit PPV onto MWCNT. Shown here are two of the pulse cycles that are repeated to achieve specific duration of deposition.

As shown in the SEM images in Figure 6.4, uniform layer of PPV was successfully coated coaxially along the lengths of all MWCNT strands. These PPV shells grew thicker with increasing total duration of pulses from 10 to 30 minutes (samples are labelled as MWCNT/PPV-*n* from here onwards, where *n* is the total duration of the overall pulse cycles in minutes). This is expected since longer deposition duration leads to larger amount of charge deposited, which infers more TBX precursor had been reduced to form PPV.

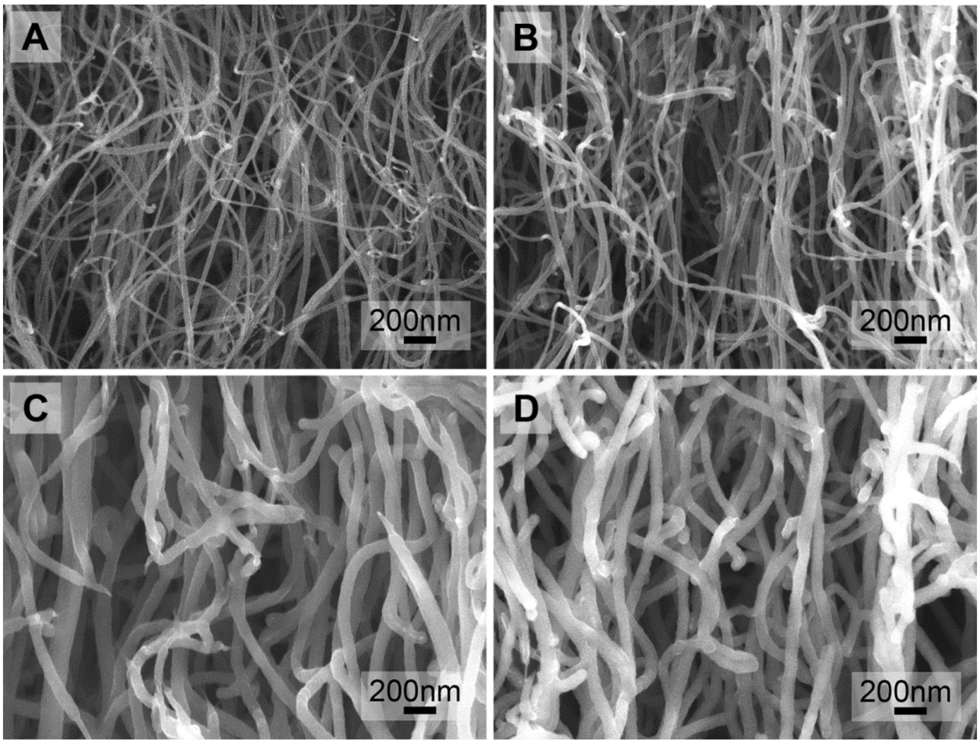

Figure 6.4: Representative SEM images of (A) MWCNT, (B) MWCNT/PPV-10, (C) MWCNT/PPV-20 and (D) MWCNT/PPV-30. The last two numbers in sample labels denote the total duration of the pulse cycles shown in Figure 6.3.

The corresponding increase of PPV shell thickness is further confirmed by HRTEM analysis (Section 2.9.2). HRTEM image in Figure 6.5A clearly shows the multi-walls of the as-grown MWCNT. After 10 minutes of pulses, the PPV shell is clearly observed but one side appears to be thicker than the other as shown in Figure 6.5B. As the pulse duration increases from 20 to 30 minutes, thicker layers of PPV shells are visible in Figure 6.5C and D, respectively. The increasing trend of PPV shell thickness as a function of pulse time is presented by the plot in Figure 6.5E. The dashed line gives the linear fit of the plot with a deposition rate of about 0.568 nm/min.

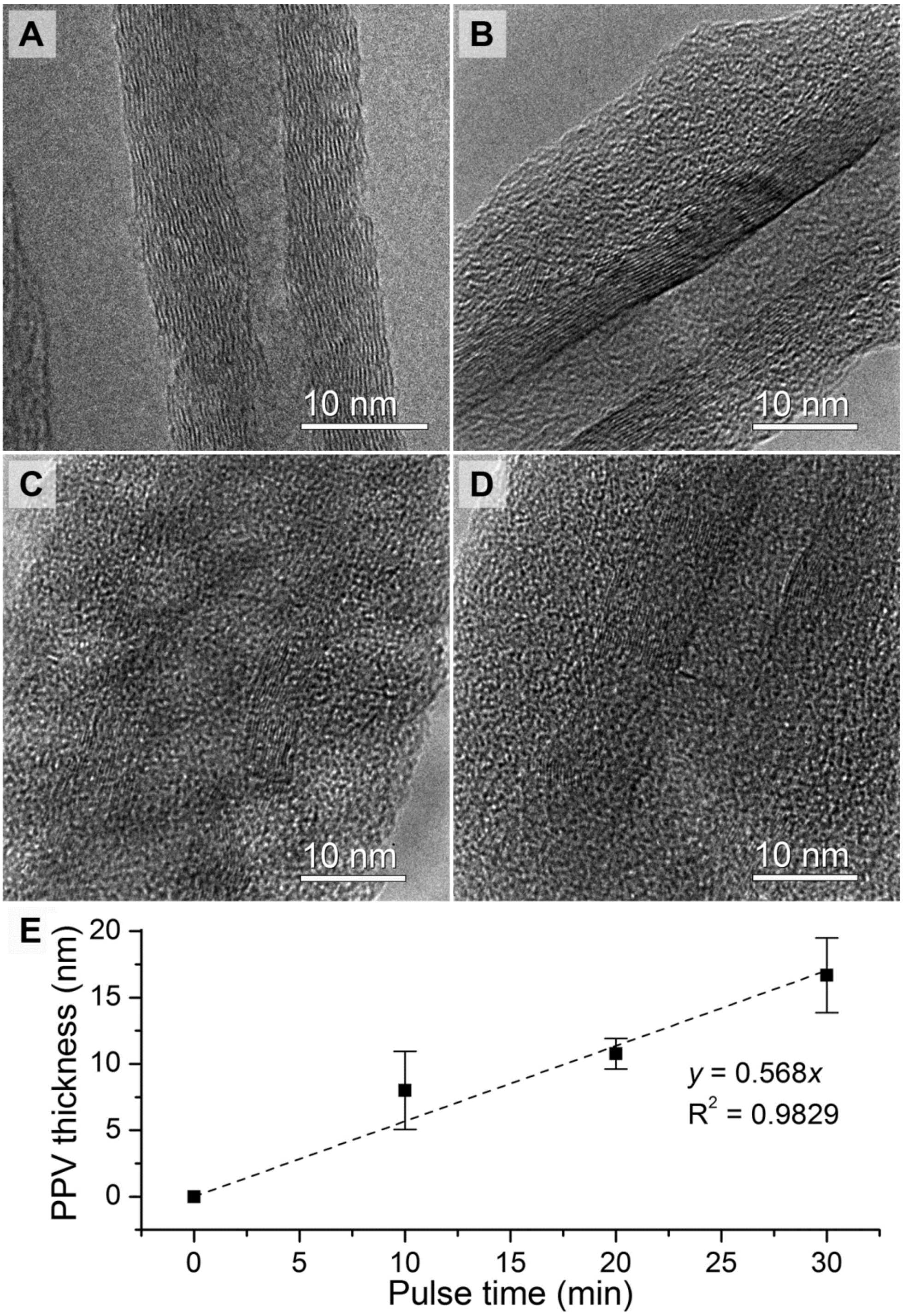

Figure 6.5: HRTEM images of (A) MWCNT, (B) MWCNT/PPV-10, (C) MWCNT/PPV-20 and (D) MWCNT/PPV-30. (E) Graph of PPV shell thickness obtained as a function of total pulse time.

Although pulsed technique was usually reported for the electrodeposition of metal,[26, 27] it was observed here to work just as fine for the electrodeposition of PPV shell. The success of this preparation is because the pulses allow slow punctuated growth of polymer on conductive surfaces including the sides of MWCNT strands and not only at the MWCNT tips. As mentioned in previous paragraph, the time off (t_{off}) and resting time (t_r) enable the recovery of TBX precursor after depletion in the reduction pulse and this compensates for the slow diffusion of TBX into the array of MWCNT.

The nanostructures were further characterized using micro-Raman spectroscopy (Section 2.9.5) to confirm the deposition of PPV. Typical Raman spectra for MWCNT and MWCNT/PPV nanostructures obtained at three different excitation wavelengths (λ_{exc}) of 785 nm, 633 nm and 532 nm are as shown respectively in Figure 6.6A, B and C. The reason for showing the spectra from three λ_{exc} will be discussed later.

Firstly, we will examine the Raman spectra of MWCNT. The as-grown MWCNT exhibits two main peaks at 1354 cm^{-1} and 1593 cm^{-1} at all λ_{exc}. These bands can be identified as the D and G bands, respectively. Ratio of the peak intensities (I_D/I_G) appears to be affected by λ_{exc}, similar to that reported.[29] Its value is larger than 1 at 785 nm (Figure 6.6A), decreasing down to near 1 from λ_{exc} = 633 nm (Figure 6.6B) to 532 nm (Figure 6.6C). The higher intensity of D band at longer λ_{exc} has been attributed to resonance with the vibrational bands of impurities and carbon nanoparticles absorbed onto MWCNT that lies in the near-infrared region.[29] In general, the ratio of I_D/I_G more or equals to 1 indicates higher level of disorder or defects in the as-grown MWCNT.

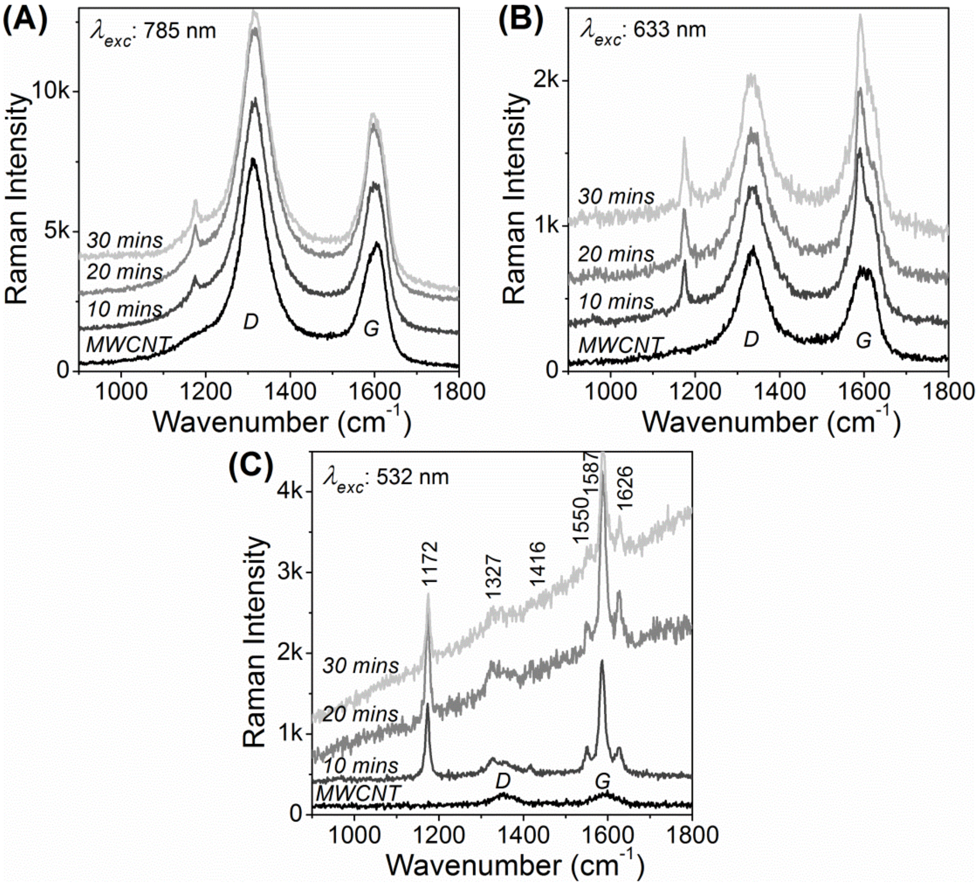

Figure 6.6: Raman spectra of MWCNT and MWCNT/PPV core-shell NWs electrodeposited at varying pulse durations as indicated. Excitation wavelengths are (A) 785 nm, (B) 633 nm and (C) 532 nm, respectively. D and G bands of MWCNT are indicated in all spectra while characteristic peaks of PPV are indicated in (C).

Characteristic Raman peaks of PPV[30] were not observed except for one small peak at 1172 cm^{-1} in the spectra excited at 785 nm (Figure 6.6A). All other peaks were completely overwhelmed by the higher intensities D and G bands of MWCNT. This λ_{exc} was applied for the characterization of PPV nanostructures in Chapter 3 but is not very useful here due to the interference from MWCNT.

Hence, Raman spectra excited at 633 nm and 532 nm were recorded. Peaks at 1550 cm^{-1}, 1587 cm^{-1} and 1626 cm^{-1} begin to be visible at 633 nm excitation (Figure 6.6B) while all peaks arising from PPV are observable at 532 nm (Figure 6.6C). These showed that MWCNT has larger contribution to the Raman spectra at longer λ_{exc} than PPV while the reverse is true for shorter λ_{exc}. This is expected since the electronic transitions of MWCNT are in resonance with near infrared λ_{exc} whereas that of PPV is with shorter λ_{exc}.[31]

Based on Figure 6.6C, while the fluorescence background interference is increasing, the main peaks of MWCNT are completely covered by the characteristic peaks of PPV as its thickness increases with longer pulse duration. In contrast to that obtained in Chapter 3, there was no 963 cm^{-1} band in the Raman spectra. This may indicate that the vinylene group of PPV prepared by this pulsed technique is not distorted from planar trans form, which is Raman-inactive.[32] In addition, the ratio of peak 1552 cm^{-1} and 1628 cm^{-1} is estimated to be near 1, indicating longer conjugation length than the PPV NTs prepared in Chapter 3.[33]

6.2 Optical properties of aligned MWCNT/PPV core-shell nanowires

Typical UV-visible absorption spectra for the core-shell NWs are compared with MWCNT as shown in Figure 6.7. Samples preparations for this characterization were shown in Section 2.9.6. Since the amount of materials used for measurement was not the same, the reflectance was normalized for better comparison. Similar to the literature, MWCNT was found to absorb significantly in the visible region with a peak at 265 nm.[34] On the other hand, MWCNT/PPV-30 core-shell nanostructures showed an absorption peak at 416 nm, which is at longer wavelength than that for PPV nanostructures in Chapter 3. Thus, consistent with the results from Raman spectra, PPV prepared here consisted of structure with longer conjugation length than the PPV nanostructures studied in Chapter 3. The large sloping background observed here should be due to the core MWCNT.

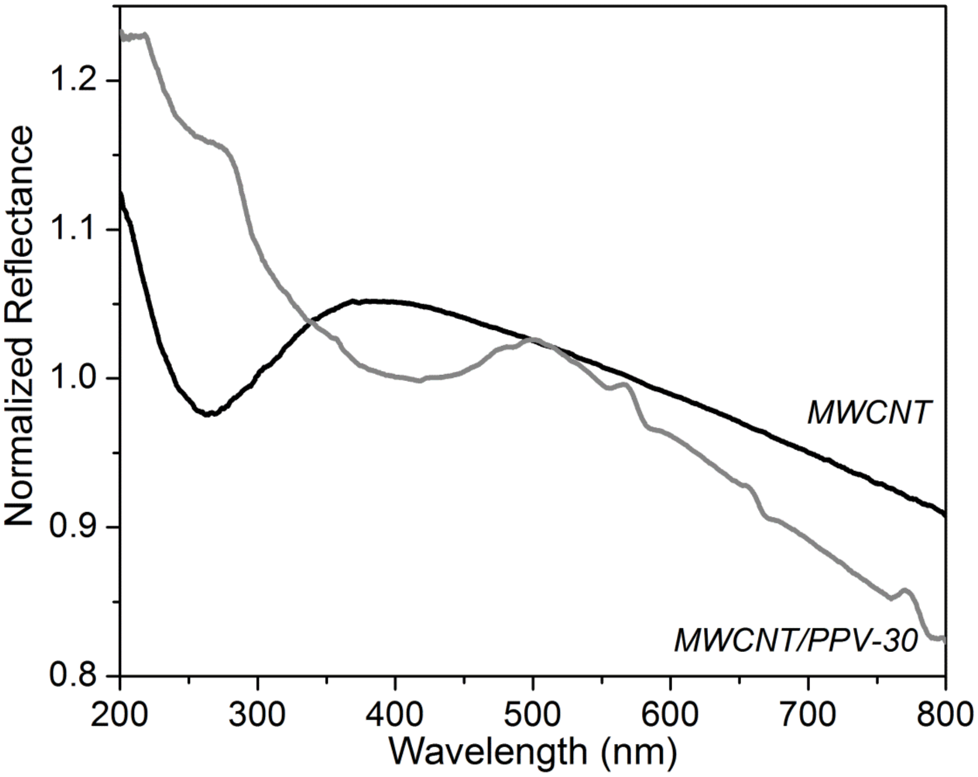

Figure 6.7: Typical UV-visible absorption spectra of MWCNT and MWCNT/PPV-30. The reflectance was normalized such that the mean intensity over all the data points is unity.

Since PPV is an optically active polymer, the MWCNT/PPV core-shell NWs were also characterized with PL spectroscopy (Section 2.9.7) and the PL spectra are shown in Figure 6.8. Since the density of MWCNT and thus the MWCNT/PPV array may vary for each sample, the PL intensities were normalized such that the mean over all the data points is unity for better comparison. As expected, MWCNT did not exhibit any PL, while all MWCNT/PPV samples exhibit PL as shown in Figure 6.8. The PL profiles are similar among all 3 samples and also to that for PPV NTs in Chapter 3, which is reproduced in Figure 6.8 for comparison.

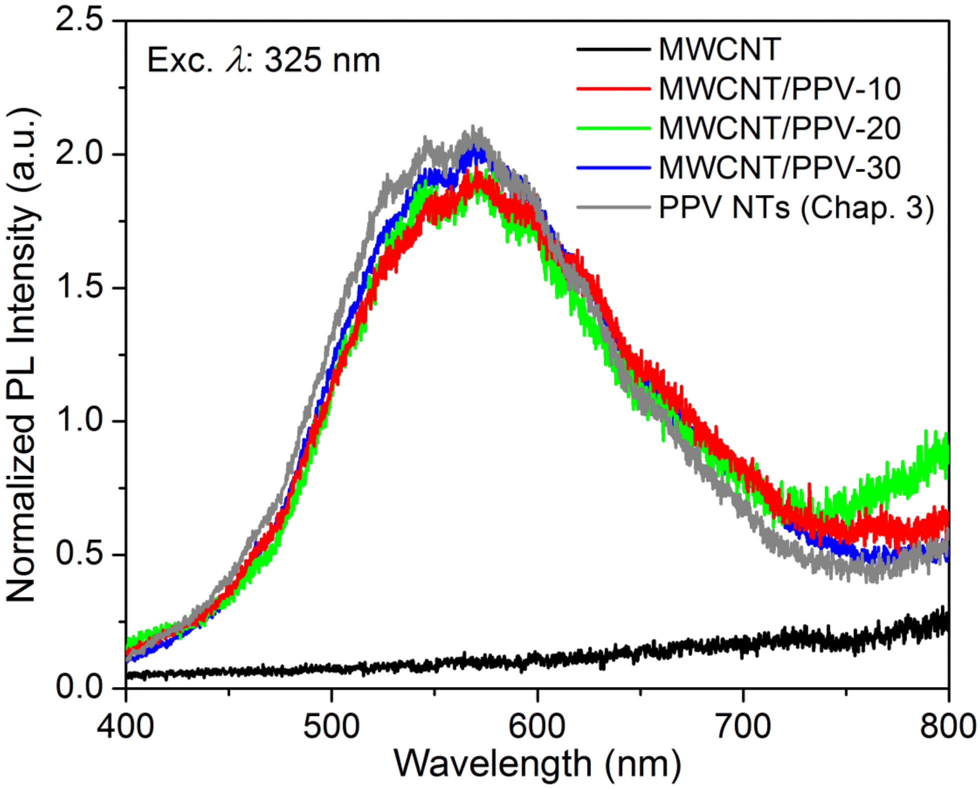

Figure 6.8: PL spectra of MWCNT and MWCNT/PPV electrodeposited at varying pulse durations as indicated. The PL intensities were normalized such that the mean intensity over all the data points is unity.

6.3 Photocurrent response of aligned MWCNT/PPV core-shell nanowires

Photocurrent (PC) responses of the MWCNT and MWCNT/PPV core-shell NWs towards 405 nm laser were measured as set up and detailed in Section 2.8. The areas of arrays to be analyzed in the set-up were 0.16 cm^2 for samples MWCNT, MWCNT/PPV-10 and MWCNT/PPV-20. Smaller area of arrays (0.06 cm^2) was measured for MWCNT/PPV-30 due to difficulty in the transfer of this array to the non-conductive substrate. To eliminate the effect of this area difference, current density (J) was calculated for all samples and used for comparison.

Electrical connections of all setup were first tested by sweeping the potential from -0.1 V to 0.1 V. The resulting current density-voltage (J-V) curves are shown in Figure 6.9. Within this potential range, the MWCNT and MWCNT/PPV show characteristics of ohmic contacts between the electrodes and the arrays. In general, the slopes of J-V curves for MWCNT/PPV samples are lower than that for MWCNT. This is expected since the conductivity of PPV is lower than MWCNT, the overall conductivities of the core-shell arrays are thus relatively lowered. J-V curve for the double-sided tape, which was used to transfer the arrays onto glass slide during device set-up, was also compared in Figure 6.9.

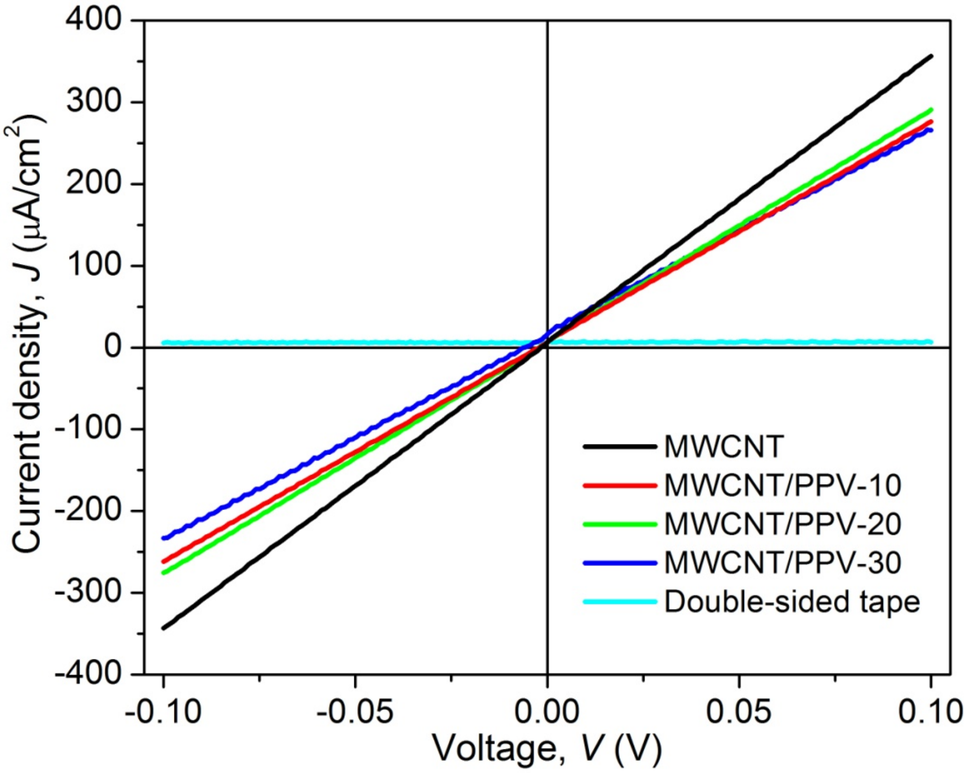

Figure 6.9: Current density versus potential (*J*-*V*) curves of MWCNT and MWCNT/PPV core-shell NWs prepared at the specified pulse times. *J*-*V* for double-sided tape is included for comparison.

To obtain the PC time response of the arrays, current at a constant bias voltage was recorded over time in the absence ("off") and presence ("on") of irradiation at 405 nm. PC response curves obtained at constant bias voltage of 0.1 V for all samples are shown in Figure 6.10. The dark current densities (J_0) for all samples were at different values due to slightly varying conductivity as revealed by the *J*-*V* curves in Figure 6.9. Thus, for ease of comparison, the current densities at the *y*-axis for Figure 6.10 were normalized by subtracting the corresponding J_0 from all measurements. The double-sided tape base shows no PC response, thus indicating no interference from the base of the setup. From Figure 6.10, it is clearly observed that the PC response increases with increasing PPV shell thickness.

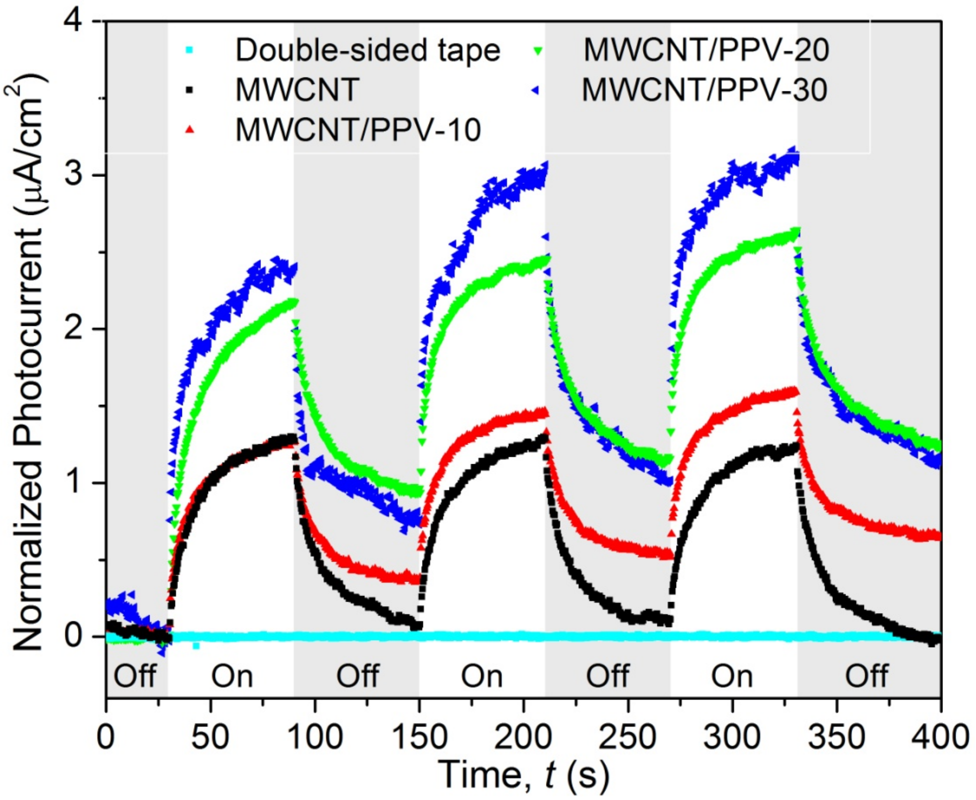

Figure 6.10: Photocurrent (PC) time response of MWCNT and MWCNT/PPV core-shell NWs prepared at indicated pulse durations at bias voltage of 0.1 V. PC for double-sided tape is included for comparison.

In the attempt to understand the kinetics of PC for the arrays of MWCNT and MWCNT/PPV core-shell NWs, we attempted to fit the PC response curves according to various functions. We have found that these PC responses did not fit well to simple exponential function[13, 35] often used to describe PC of MWCNT and MWCNT/polymer composite films, nor the stretched exponential relaxation law,[36, 37] which was used to describe the PC decay of PPV films. Instead, it was found that the rising and decay curves of our PC responses are well described by the two-process exponential functions[38] as below:

$$\text{Rising: } J = J_0 + A_1[1-\exp(-\frac{t-t_0}{\tau_1})] + A_2[1-\exp(-\frac{t-t_0}{\tau_2})] \qquad (6.1)$$

$$\text{Decay: } J = J_0 + A_1 \exp(-\frac{t-t_0}{\tau_1}) + A_2 \exp(-\frac{t-t_0}{\tau_2}) \qquad (6.2)$$

Here, J_0 is the dark current density and t_0 is the initial response time. There are two characteristic current amplitudes (A_1 and A_2) and time constants (τ_1 and τ_2) in the PC response. Examples of curve fittings for PC build-up and decay are shown in Figure 6.11A and Figure 6.11B, respectively. These are for the first PC cycle of MWCNT/PPV-20 sample at bias voltage of 0.10 V. The fittings gave R^2 of 0.9980 and 0.9963, respectively, indicating very good fit of the experimental data.

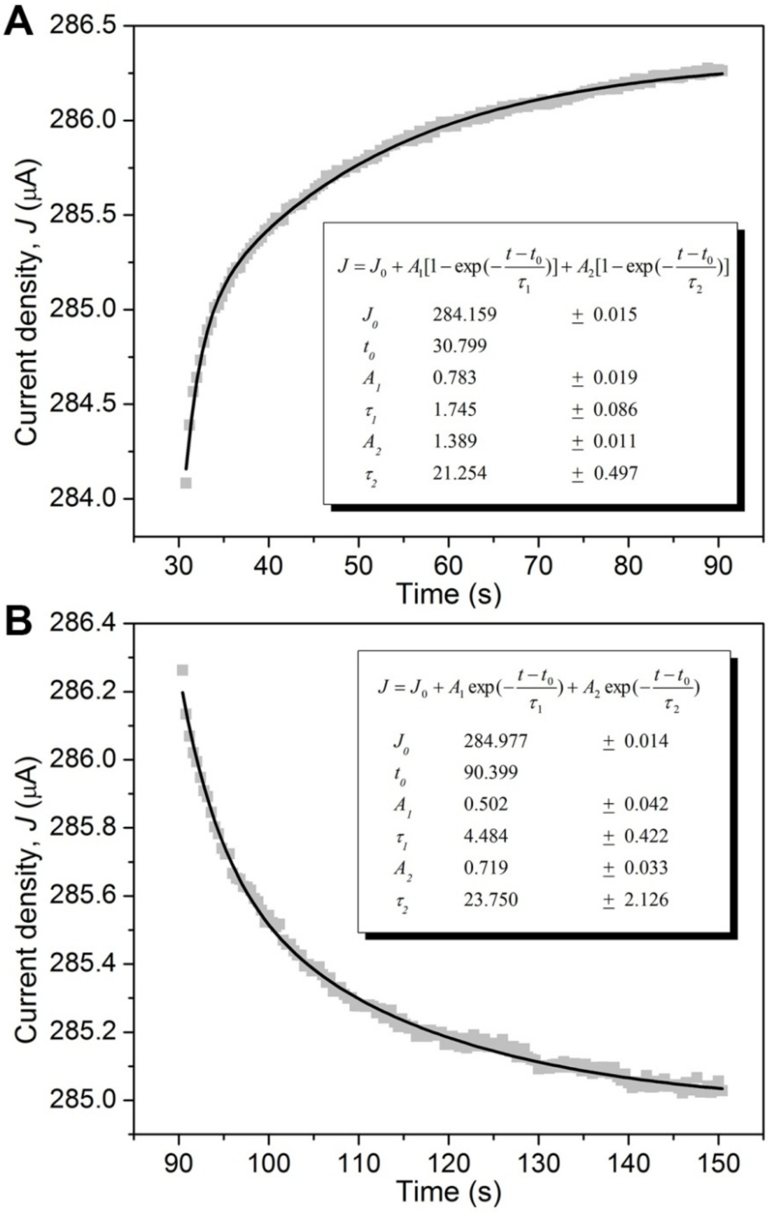

Figure 6.11: (A) Rising and (B) decay photocurrent time response of MWCNT/PPV-20 at bias voltage of 0.10V upon light “on” and light “off” state, respectively. The black solid lines are the exponential fittings of the corresponding data in gray. Inset boxes show the calculated parameters for each fit.

Included in Figure 6.11A and Figure 6.11B are the fitted parameters for the corresponding response curves. There are two sets of parameters, each for a type of process occurring during the PC build-up and decay.

Characteristic time constant τ_1 is generally shorter than τ_2. Thus, the former most probably originates from the faster process of photo-generation of carriers while the latter denotes slower process of thermal effect, carrier trapping/de-trapping and/or interaction of surface states with the irradiation.[38] In addition, the amplitude of PC upon irradiation, $J_p - J_0$, where J_p is the peak current density, can also be obtained by combining the fitted current amplitudes, $A_1 + A_2$.

From the fittings of the PC response curves, amplitude of the PC build-up ($J_p - J_0$) at the first light "on" stage and the average time constants (τ_1 and τ_2) were compiled in Table 6.1. This table clearly illustrates the increase of PC with PPV deposition time and thus the PPV shell thickness. This demonstrates that the PPV shell could improve the photo-response of the hybrid core-shell NWs towards 405 nm laser.

Table 6.1: PPV shell thickness estimated from TEM analysis, PC amplitude (J_p-J_0), and two characteristic time constants (τ_1 and τ_2) of PC build-up and decay, at bias 0.10 V for samples prepared at the corresponding PPV deposition pulse time.

Pulse time (mins)	PPV thickness (nm)	PC (μA/cm^2)	Rising		Decay	
			τ_1 (s)	τ_2 (s)	τ_1 (s)	τ_2 (s)
0	0	1.28	3.3	21.7	3.2	24.0
10	8.00	1.28	2.2	21.8	2.1	15.8
20	10.76	2.17	1.7	16.1	3.7	24.8
30	16.67	2.41	0.7	22.7	1.5	31.0

The shorter time constant, τ_1, for PC build-up was found to be generally decreasing with increasing PPV shell thickness. This indicates faster generation of carriers upon irradiation. As shown in Figure 6.7, MWCNT/PPV exhibits an absorption peak at around 416 nm. Upon irradiation of 405 nm laser, PPV is expected to absorb most of the photons, generating more charge carriers that diffuse across the array and increase the PC. For the PC decay, τ_1 is similar to that for PC build-up except for MWCNT/PPV-20. More studies should be carried out to further confirm this exception.

The limiting process is obviously the slower process of thermal effect and charge trapping which is represented by time constant τ_2. Based on Table 6.1, the values for τ_2 at PC build-up appear to be quite constant. Since our MWCNT sample originally contains high amount of disorder or defects as observed from the Raman peak ratio I_D/I_G (Figure 6.6), much of the charge trapping effects occur at the MWCNT. Thus, the value of τ_2 is quite constant even with increasing thickness of PPV shell because it is limited by the highly disordered or defective MWCNT. For the PC decay, the τ_2 values appear to increase with PPV shell thickness and are generally larger than those of the PC build-up. In the absence of irradiation, τ_2 represents time required for the dissipation of heat accumulated during light irradiation and trapping of charge. The rate of heat dissipation may be slower than accumulation process, thus the larger decay τ_2 value. In addition, the increase of decay τ_2 has led to larger upward slope for PC response curves of samples with thicker PPV shell, as shown in Figure 6.10. The carriers took longer time to decay to the original state when light was “off” than it was when building-up upon irradiation.

One important note is that the PPV layer could be oxidized upon irradiation by the 405 nm laser in air, as was observed in Chapter 3 for PPV NTs. This photo-oxidation of PPV may affect the PC response of this MWCNT/PPV system. It may not be detrimental, however, as Antoniadis *et al.*[39] have reported that oxidized PPV film with C=O group was found to improve the photoconductivity of device.

6.4 Summary

In summary, MWCNT/PPV core-shell NWs were successfully fabricated via simple pulsed potentiometry. The PPV shell was uniformly coated along the length of each strands of MWCNT and its thickness increases linearly with pulse time, showing good control of this method on the shell growth. Conductivity of the MWCNT/PPV core-shell NWs was found to be ohmic but less conductive compared to MWCNT. These MWCNT/PPV NWs exhibit PC response under the irradiation of 405 nm laser. The rising and decay curves were found to fit well to exponential functions describing two time-dependent processes. The faster process with time constant τ_1 represents the photo-generation of charge carriers while the slower process (τ_2) describes the thermal effect and charge trapping at defective sites. With increasing PPV shell thickness, it was observed that PC also increases. The corresponding τ_1 for PC build-up decreases with

PPV shell thickness, indicating improvement of photo-generation of carriers. The values of τ_2 appear to be similar across all samples during PC build-up. Much of the charge trapping probably occurs at the highly disordered/defective MWCNT. Comparing to that for PC build-up, τ_2 for PC decay were generally larger and appear to increase with PPV shell thickness. Rate of heat dissipation may be slower than accumulation process, leading to larger decay τ_2 value.

It is noted that the results presented here are preliminary and more work would be required to understand effects such as laser power, laser wavelength, and temperature on the photo-response of the hybrid nanostructures.

6.5 References

1. S. Iijima. *Nature* **354** (1991) 56-58.
2. T. W. Ebbesen, H. J. Lezec, H. Hiura, J. W. Bennett, H. F. Ghaemi, T. Thio. *Nature* **382** (1996) 54-56.
3. K. Anazawa, K. Shimotani, C. Manabe, H. Watanabe, M. Shimizu. *Appl. Phys. Lett.* **81** (2002) 739-741.
4. P. Kim, L. Shi, A. Majumdar, P. L. McEuen. *Phys. Rev. Lett.* **87** (2001) 215502.
5. M. M. J. Treacy, T. W. Ebbesen, J. M. Gibson. *Nature* **381** (1996) 678-680.
6. E. W. Wong, P. E. Sheehan, C. M. Lieber. *Science* **277** (1997) 1971-1975.

7. P. J. F. Harris. *Int. Mater. Rev.* **49** (2004) 31-43.

8. J. H. Burroughes, D. D. C. Bradley, A. R. Brown, R. N. Marks, K. Mackay, R. H. Friend, P. L. Burns, A. B. Holmes. *Nature* **347** (1990) 539-541.

9. C. J. Zhao, H. H. Wang, Z. Y. Jiang. *Appl. Surf. Sci.* **207** (2003) 6-12.

10. G. Malliaras, R. Friend. *Phys. Today* **58** (2005) 53-58.

11. H. Ago, K. Petritsch, M. S. P. Shaffer, A. H. Windle, R. H. Friend. *Adv. Mater.* **11** (1999) 1281-1285.

12. Z. H. Xu, Y. Wu, B. Hu, I. N. Ivanov, D. B. Geohegan. *Appl. Phys. Lett.* **87** (2005) 263118.

13. P. Stokes, L. W. Liu, J. H. Zou, L. Zhai, Q. Huo, S. I. Khondaker. *Appl. Phys. Lett.* **94** (2009) 042110.

14. C. Bounioux, E. A. Katz, R. Yerushalmi-Rozen. *Polym. Adv. Technol.* **23** (2012) 1129-1140.

15. L. Li, Z. Y. Qin, X. Liang, Q. Q. Fan, Y. Q. Lu, W. H. Wu, M. F. Zhu. *J. Phys. Chem. C* **113** (2009) 5502-5507.

16. Q. Peng, Z. H. Wen, G. S. Zeng, J. P. Zou, S. Q. Lu. *Chem. Lett.* **38** (2009) 380-381.

17. Y. P. Fang, J. W. Liu, D. J. Yu, J. P. Wicksted, K. Kalkan, C. O. Topal, B. N. Flanders, J. D. Wu, J. Li. *J. Power Sources* **195** (2010) 674-679.

18. M. Gao, S. M. Huang, L. M. Dai, G. Wallace, R. P. Gao, Z. L. Wang. *Angew. Chem. Int. Edit.* **39** (2000) 3664-3667.

19. M. Hughes, M. S. P. Shaffer, A. C. Renouf, C. Singh, G. Z. Chen, J. Fray, A. H. Windle. *Adv. Mater.* **14** (2002) 382-385.

20. X. T. Zhang, J. Zhang, R. M. Wang, T. Zhu, Z. F. Liu. *Chemphyschem* **5** (2004) 998-1002.

21. X. X. Bai, X. J. Hu, S. Y. Zhou, J. Yan, C. H. Sun, P. Chen, L. F. Li. *Electrochim. Acta* **87** (2013) 394-400.

22. Y. Zhou, Z. Y. Qin, L. Li, Y. Zhang, Y. L. Wei, L. F. Wang, M. F. Zhu. *Electrochim. Acta* **55** (2010) 3904-3908.

23. H. F. Guo, H. Zhu, H. Y. Lin, J. Q. Zhang. *Mater. Lett.* **62** (2008) 3919-3921.

24. K. Kim, B. H. Kim, S. H. Joo, J. S. Park, J. Joo, J. I. Jin. *Adv. Mater.* **17** (2005) 464-468.

25. F. Massuyeau, Y. C. Zhao, A. A. El Mel, A. Yaya, F. Geschier, E. Gautron, S. Lefrant, J. Y. Mevellec, C. Ewels, C. S. Hsu, E. Faulques, J. Wery, J. L. Duvail. *Nano Res.* **6** (2013) 149-158.

26. R. Elnathan, R. Kantaev, F. Patolsky. *Nano Lett.* **8** (2008) 3964-3972.

27. R. Inguanta, S. Piazza, C. Sunseri. *Appl. Surf. Sci.* **255** (2009) 8816-8823.

28. N. V. Mandich. *Metal Finishing* **98** (2000) 375-380.

29. Y. Ouyang, L. M. Cong, L. Chen, Q. X. Liu, Y. Fang. *Physica E* **40** (2008) 2386-2389.

30. K. Honda, Y. Furukawa, H. Nishide. *Vib. Spectrosc* **40** (2006) 149-154.

31. E. Mulazzi, R. Perego, H. Aarab, L. Mihut, S. Lefrant, E. Faulques, J. Wery. *Phys. Rev. B* **70** (2004) 155206.

32. A. Sakamoto, Y. Furukawa, M. Tasumi. *J. Phys. Chem.* **96** (1992) 1490-1494.

33. T. P. Nguyen, V. H. Tran, P. Destruel, D. Oelkrug. *Synth. Met.* **101** (1999) 633-634.

34. H. Ago, M. S. P. Shaffer, D. S. Ginger, A. H. Windle, R. H. Friend. *Phys. Rev. B* **61** (2000) 2286-2290.

35. H. B. Huang, Z. Liu, Y. C. Zhao, K. H. Zheng, S. S. Xie, L. F. Sun. *J. Nanosci. Nanotechnol.* **9** (2009) 1326-1329.

36. C. H. Lee, G. Yu, A. J. Heeger. *Phys. Rev. B* **47** (1993) 15543-15553.

37. B. Dulieu, J. Wery, S. Lefrant, J. Bullot. *Phys. Rev. B* **57** (1998) 9118-9127.

38. J. L. Sun, J. Xu, J. L. Zhu, B. L. Li. *Appl. Phys. A: Mater. Sci. Process.* **91** (2008) 229-233.

39. H. Antoniadis, L. J. Rothberg, F. Papadimitrakopoulos, M. Yan, M. E. Galvin, M. A. Abkowitz. *Phys. Rev. B* **50** (1994) 14911-14915.

Chapter 7

Conclusions and Outlook

In this thesis, we had presented synthesis of various types of 1D nanostructures using AAO and MWCNT as the template. AAO were utilized as the sacrificial template and/or source of Al^{3+} ions, and MWCNT as the support for deposition. Electrochemical deposition technique was used as the main fabrication method for its ease of control over the type and length of NWs or NTs.

Chapter 3 and Chapter 4 presented the use of AAO as sacrificial shape-directing template for synthesis of various 1D nanostructures. In Chapter 3, the template was used to obtain PPV NWs and NTs which were prepared through the electro-reduction of TBX precursor within the nanochannels of AAO at constant potential. We have shown that either NWs or NTs can be obtained by manipulating the conditions of the plating solution and changing the deposition potential. The former influenced the diffusion of precursor into the AAO nanochannels while the latter affected the deposition rate. With an increase in diffusion rate (in the presence of oxygen and moisture) and slow deposition rate (at low cathodic potential), mainly NWs were formed. The reverse conditions, on the other hand, produced mostly NTs.

We have also demonstrated the ability to micro-pattern these arrays of PPV nanostructures using focused laser beam technique. An interesting “red-shift” of the PL maximum was observed upon laser modification in air. Observations from both DR-FTIR and XPS spectra indicated the oxidation of PPV for regions laser-modified in air. However, based on literatures findings, oxidation of PPV did not cause any shift in PL peak. Hence, in addition to oxidation, some other phenomenon, e.g. formation of intermediate trap states, maybe responsible for the red-shift upon laser modification. While further investigation is needed to probe this phenomenon, this technique has the potential to fabricate coloured patterns on the array of PPV nanostructures by adjusting the laser power and environment of patterning.

In Chapter 4, we further demonstrated the versatility of AAO as shape-directing template for synthesis of various coaxial multi-layered 1D nanostructures. A “Pore Widening” method was developed to manipulate the width of AAO nanochannels. Here, a mild etching reagent was chosen to controllably etch away the channel walls of AAO, creating annular gaps around the deposited core NWs for subsequent deposition of shells. With judicious selection of materials and sequences of steps, we have illustrated strategies to fabricate polymer/metal, metal/metal and polymer/metal/metal core-shell NWs. In addition, metal oxide/metal double-walled NTs were also prepared using this method. With such flexibility, this “Pore Widening” method can be extended to fabricate coaxial multi-layered 1D nanostructures made up of other combination of materials such as metals, semiconductors and polymers. By coupling the core and shell materials, we envisage that many interesting nanostructures can be generated that will be useful in potential functional devices in various areas.

Subsequently in Chapter 5, AAO was shown to be more than just a sacrificial template. Hierarchical nanostructures of Co/Al-LDH NFs supported on Co NWs (Co/Al-NWNF) were fabricated using AAO. Here, AAO was the template to grow Co NWs and also the source providing the Al^{3+} ions in the alkaline solution for growth of Co/Al-LDH NFs. The content of Al in the NFs was found to increase with the duration of alkaline treatment and the crystal structure matched well with HT-like $Co_6Al_2CO_3(OH)_{16}.4H_2O$. The resulting arrays were used directly as electrodes for electrochemical capacitor and glucose sensing applications, without the need for binder. Overall, the electrochemical capacitance and glucose sensing capability of these Co/Al-NWNF electrodes were found to improve when Al content is high and Co/Al-LDH is the dominant species on the electrode surface. The largest capacitance of 0.510 F/cm^2 was obtained from Co/Al-NWNF-48 containing 12% Al at current density of 2.5 mA/cm^2. For application in glucose sensing, high sensitivity value of 543.0 μAmM^{-1}cm^{-2} was achieved using Co/Al-NWNF-24 as electrode at applied potential of 0.40 V.

Looking forward, Co/Al-NWNF arrays can also be further tested for application in detection of other types of analytes such as hydrazine and hydrogen peroxide. In addition, this synthesis method can also be utilized to prepare other type of LDH NFs such as Ni/Al-NWNF. Instead of Co NWs, Ni NWs can be firstly deposited followed by alkaline treatment to grow Ni/Al-LDH NFs onto the NWs. Furthermore, a combination of LDHs such as Co/Ni/Al-LDH can also be fabricated by subjecting Co-Ni multi-segmented NWs to alkaline treatment.

Finally in Chapter 6, we described the use of aligned MWCNT as supporting template for the growth of MWCNT/PPV core-shell NWs. The electropolymerization conditions established in Chapter 3 was adapted to coaxially grow PPV onto each strands of MWCNT, forming arrays of aligned MWCNT/PPV core-shell NWs. Both constant potentiometry and pulsed potentiometry were applied. The latter was found to show better control of the shell thickness. The conductivities of the MWCNT/PPV core-shell NWs were similar regardless of PPV shell thickness and this was expected since PPV is generally less conductive. All MWCNT and MWCNT/PPV exhibited PC response towards 405 nm laser. The rising and decay curves were found to fit well to exponential functions describing two time-dependent processes. The faster process represents the photo-generation of charge carriers while the slower process describes the thermal effect and charge trapping at defective sites. It was observed that PC increases with PPV shell thickness. Besides, the time constant representing the photo-generation of carriers also decreased with increasing shell thickness.

On the basis of our preliminary findings, more work would be required to investigate effects such as laser power, laser wavelength and temperature on the photo-response of the hybrid nanostructures. Nevertheless, by using similar pulsed deposition method, many other materials other than polymers (such as CdS, MnO, etc.) can be decorated onto MWCNT. These hybrid nanostructures have high potential for applications in optoelectronic and electrochemical capacitor.

In general, synthesis of 1D nanostructures using template-assisted synthesis has many advantages. It is simple and easy. The use of template can be combined with various other deposition methods such as sol-gel, precursor solution infiltration and chemical vapour deposition to fabricate many 1D nanomaterials. However, the type of materials to be deposited is limited to those inert to the chemical(s) used to remove the template at the end of the synthesis procedures. To remove AAO template, for example, the use of NaOH or diluted acids is necessary. Thus, only materials that are inert to these reagents can be prepared using this template. In addition, some impurities due to incomplete removal of template may also be a problem. Nevertheless, with judicious selection of materials and sequences of steps, template-assisted method will provide easy and relatively cheap ways to synthesize 1D nanostructures.